Spring 1-1-2012

# An operational radar-based precipitation climatology for the Swiss Alps

James V. Rudolph
*University of Colorado at Boulder*, james.rudolph@colorado.edu

# An operational radar-based precipitation climatology for the Swiss Alps

by

JAMES V. RUDOLPH

B.S., University of Illinois, 1992

M.S., University of Colorado, 2010

A thesis submitted to the

Faculty of the Graduate School of the

University of Colorado in partial fulfillment

of the requirement for the degree of

Doctor of Philosophy

Department of Atmospheric and Oceanic Sciences

2012

This thesis entitled:
An operational radar-based precipitation climatology for the Swiss Alps
written by James V. Rudolph
has been approved for the Department of Atmospheric and Oceanic Sciences.

_____
Katja Friedrich

_____
John J. Cassano

Date_____

The final copy of this thesis has been examined by the signatories, and we find that both the content and the form meet acceptable presentation standards of scholarly work in the above mentioned discipline.

# ABSTRACT

Rudolph, James V. (Ph.D., Department of Atmospheric and Oceanic Sciences)

**An operational radar-based precipitation climatology for the Swiss Alps**

Thesis directed by Assistant Professor Katja Friedrich

Eleven years (2000-2010) of ground-based operational weather radar data are used to analyze three-dimensional precipitation distribution in the Swiss Alps. Daily synoptic scale weather patterns associated with high resolution (2 x 2 $km^2$) radar-estimated precipitation show an advective synoptic scale pattern with southerly flow results in the highest median and 90th quantile values for total daily precipitation while a convective synoptic scale pattern results in elevated frequency of extreme rainfall rate events. Radar-estimated precipitation observations are coupled with geopotential height fields from Community Climate System Model Version 3.0 (CCSM3) and indicate that changes in synoptic pattern frequencies will result in an approximately 10-15% decrease in decadal precipitation over the course of the 21st century for seven Swiss river basins. Radar reflectivity is also used for analysis of precipitation systems' vertical structure on the southern side of the Alps. Storms occurring in summer are more convective than winter season storms as indicated by more frequent observation of reflectivity at higher altitudes during summer. Seasonal classification of individual storms by vertical structure of reflectivity reveals a transition between winter and summer-type storms during spring and fall that follows changes in average daily surface temperature. Although summer and winter-type storms result in a similar amount of total precipitation, summer-type storms have shorter duration, and therefore, greater intensity. The dependence of storm type on temperature has implications for intensification of the hydrologic cycle due to climate change. Warmer winter, spring, or fall surface temperatures may affect average precipitation intensity by increasing the

number of days per year that experience more intense convective precipitation while decreasing the probability of less intense stratiform precipitation.

# ACKNOWLEDGEMENTS

My research was supported by NSF grant AGS-0937035 and the University of Colorado at Boulder Department of Atmospheric and Oceanic Sciences.

I am extremely grateful to my research advisor, Katja Friedrich, for providing me with the opportunity to investigate precipitation in mountainous terrain, the exact topic that motivated me to enter graduate school in the first place, and also for encouraging me to pursue my own avenues of research.

I also thank my committee members John Cassano, Thomas Chase, Balaji Rajagopalan, and Andrew Slater for their ideas and guidance. Your interest, engagement, and availability to discuss my work have been very beneficial.

Of course, none of this work would have been possible without the assistance of Urs Germann and Marco Boscacci in providing MeteoSwiss operational radar data products.

I also express my appreciation to the following organizations: MeteoSwiss for rain gauge and surface temperature data which were downloaded through the web-based interface IDAWEB portal (https://gate.meteoswiss.ch/idaweb); the European Centre for Medium-Range Weather Forecasts (ECMWF) for providing free internet access to ERA Interim reanalysis data; and the Hydrology Group, Institute of Geography, University of Bern for providing Swiss river basin coordinates, and the Community Climate System Model project (www.ccsm.ucar.edu), supported by the Directorate for Geosciences of the National Science Foundation and the Office of Biological and Environmental Research of the U.S. Department of Energy.

Most importantly I thank my wife, Leslie, for encouraging me to pursue graduate school and for her support along the way, and also, Max, for his example of pure curiosity.

TABLE OF CONTENTS

# LIST OF TABLES

# LIST OF FIGURES

# CHAPTER 1: INTRODUCTION

Precipitation is a primary component of the hydrologic cycle and has significant implications for fresh water supply and storage, as well as flooding. Precipitation characteristics such as total amount, frequency, intensity, type, and duration are likely to be affected by changes in global and regional climate. The Fourth Assessment Report of the Intergovernmental Panel on Climate Change (IPCC, Kundzewicz et al. 2007) emphasizes that changes in precipitation related to climate change will exacerbate the current stress on water resources from population growth and land-use change. Mountains play an especially important role in the hydrologic cycle with implications for runoff, flooding, water storage, and glacier-mass balance (Beniston, 2005). Changes in precipitation amount and intensity in mountainous regions are of major concern, affecting both the localized alpine area and the lowlands that utilize fresh water supplied from upper elevation catchments and are exposed to flooding risk that results from extreme precipitation. Understanding past and future precipitation characteristics in mountainous regions is essential to develop water policy and management strategies for responding to the impact of climate change. The 2008 IPCC technical paper on climate change and water notes that there is insufficient information on the effect of climate change where topography generates fine spatial scales in climate, and also that further development is needed of catchment scale climate models that are more relevant to water management (Bates et al. 2008).

My overall research intent is to utilize operational radar data to analyze precipitation distribution in the European Alps with three main objectives: 1) develop a high resolution radar-based precipitation climatology and relate it to synoptic weather patterns, 2) leverage the relationship between precipitation distribution and synoptic patterns to downscale precipitation from global climate models (GCMs), and 3) utilize the 3-diminensional spatial nature of radar data to investigate the vertical structure of precipitation.

In Chapter 2, operational radar is utilized to create a high resolution decade-length precipitation record, and the relationship between precipitation distribution and synoptic weather patterns is analyzed (Rudolph et al., 2011). The contents of Chapter 2 were published in the *Journal of Applied Meteorology and Climatology* in an article titled "Relationship between radar-estimated precipitation and synoptic weather patterns in the European Alps" (Rudolph et al., 2011). The distribution of total daily precipitation and occurrence of high precipitation rate events over the years 2000-2008 are summarized for regions located to the north, northwest, west, and south of the main crest of the Alps. The goals for development of this analysis are to a) demonstrate the use of radar-based precipitation estimates in creating a high resolution decade-length precipitation record, b) identify seasonal and annual trends over the period of the study, c) compare regional precipitation distributions within the Alps, and d) beyond direct analysis of precipitation characteristics, understand the relationship between precipitation distribution and synoptic scale weather patterns. Systematic classification of synoptic scale weather patterns into discrete categories over the time span of the analysis enables the investigation of potential correlations between synoptic patterns and resulting precipitation characteristics.

In Chapter 3, radar-estimated precipitation observations are combined with GCM data to forecast the effects of climate change on future precipitation at spatial resolution relevant to river basin hydrologic models (Rudolph et al. 2012). The contents of Chapter 3 were published in the *Journal of Climate* in an article titled "Model-based estimation of dynamic effect on 21$^{st}$ century precipitation for Swiss river basins" (Rudolph et al. 2012). Synoptic weather patterns are used as a link between the high resolution (~2 km) radar-based precipitation climatology developed in Chapter 2 and low resolution (~100 km) GCM output in order to determine expected trends in

precipitation for Swiss river basins. The dynamic effect of climate change on future precipitation is evaluated by using future changes in the occurrence of synoptic patterns to quantify future changes in precipitation. This approach to understanding the impact of climate change on precipitation is unique because it provides an additional perspective to downscaled climate models for locations where sufficient radar data are available. The use of radar-estimated precipitation observations with high spatial resolution enables the development of a river-basin specific analysis that accounts for terrain and localized climate variation, yet is not reliant on interpolation of sparse data.

In Chapter 4, the three-dimensional nature of radar reflectivity data is used to investigate the seasonal variability and annual cycle of vertical reflectivity structure over southern Switzerland (Rudolph and Friedrich 2012). The material in Chapter 4 has been accepted by the *Journal of Hydrometeorology* as an article titled "Seasonality of vertical structure in radar-observed precipitation over southern Switzerland" and is in review at the time of publication of this dissertation (Rudolph and Friedrich 2012). A relationship is found between the vertical structure of reflectivity and surface precipitation characteristics such as total amount, duration, and intensity of precipitation. It is important to establish a link (or lack thereof) between vertical reflectivity structure and surface precipitation measurements in order to understand the implications that various storm types, as identified by the vertical structure of reflectivity, have for the hydrologic cycle. Furthermore, the effects of surface temperature on the vertical structure of reflectivity and potential impacts of climate change on the hydrologic cycle are examined. Previous work indicates that changes in synoptic patterns over the 21st century in Europe will increase the proportion of convective precipitation for Swiss river basins (Rudolph et al. 2012). Chapter 4 further examines the possibility that precipitation events in southern Switzerland may

become more convective as temperature increases and how an increase in convective precipitation may contribute to an increase in precipitation intensity.

The characterization of past and future precipitation lies at the interface between atmospheric climate science and hydrology. This dissertation is relevant to alpine areas worldwide that rely on orographic forcing of precipitation as an input to the hydrological cycle. In addition, the work presented here demonstrates the value of intermountain radar networks for hydrological monitoring and the potential utility of combining radar data with climate models to quantify effects of climate change on localized precipitation.

# CHAPTER 2
# RELATIONSHIP BETWEEN RADAR-ESTIMATED PRECIPITATION AND SYNOPTIC WEATHER PATTERNS IN THE EUROPEAN ALPS

## 2.1. Introduction

Precipitation is a primary element of the water cycle, and precipitation characteristics such as frequency, intensity, type, and duration are likely to be affected by changes in global and regional climate. The Fourth Assessment Report of the Intergovernmental Panel on Climate Change (IPCC, Kundzewicz et al. 2007) emphasizes that changes in precipitation related to climate change will exacerbate the current stress on water resources from population growth and land-use change. Mountains play an especially important role in the hydrologic cycle with implications for runoff, flooding, water storage, and glacier-mass balance (Beniston, 2005). Changes in precipitation amount and intensity in mountainous regions are of major concern, affecting both the localized alpine area and the lowlands that utilize fresh water supplied from upper elevation catchments and are exposed to flooding risk that results from extreme precipitation. Understanding past and future precipitation characteristics in mountainous regions is essential to develop water policy and management strategies for responding to the impact of climate change. The 2008 IPCC technical paper on climate change and water notes that there is insufficient information on the effect of climate change where topography generates fine spatial scales in climate, and also that further development is needed of catchment scale climate models that are more relevant to water management (Bates et al. 2008).

The intent of this study is to utilize operational radar data to analyze precipitation distribution in the European Alps. Here, the distribution of total daily precipitation and occurrence of high precipitation rate events over the years 2000-2008 are summarized for regions located to the north, northwest, west, and south of the main crest of the Swiss Alps. The goals for development of this analysis are to 1) demonstrate the use of radar-based precipitation estimates in creating a

decade length precipitation record, 2) compare regional precipitation distributions within the Alps, and 3) beyond direct analysis of precipitation characteristics, understand the relationship between precipitation distribution and synoptic scale weather patterns. Systematic classification of synoptic scale weather patterns into discrete categories over the time span of the analysis enables correlations between synoptic patterns and resulting precipitation characteristics.

The analysis presented herein is unique because of its operational radar basis. Previous European Alps precipitation climatologies have reported precipitation quantity and intensity as inferred from daily rain gauge values (e.g., Schönwiese et al., 1994; Widmann and Schär, 1997; Frei and Schär, 1998; Schmidli et al., 2002; Klein Tank and Können, 2003; Begert et al., 2005; Schmidli and Frei, 2005; Moberg et al. 2006; Zolina et al., 2008; Zolina et al., 2010). Although rain gauge based precipitation climatologies provide valuable information about seasonal and regional precipitation attributes, they are limited by the spatial resolution of the rain gauge network. Smith et al. (2003) showed that precipitation distribution in complex Alpine terrain varies at scales less than 10 km, yet rain gauge based precipitation climatologies for the Alps only attain spatial resolution of approximately 25 km (Frei and Schär, 1998). The radar based precipitation data presented here has underlying spatial resolution of 2 x 2 $km^2$.

Furthermore, the radar basis of this study provides higher temporal resolution than most non-automated rain gauges. Rain gauge based climatologies typically characterize data on a daily basis (Frei and Schär, 1998; Klein Tank and Können, 2003; Schmidli and Frei, 2005; Moberg et al. 2006; Zolina et al., 2008; Zolina et al., 2010), whereas radar provides precipitation estimates at 5-15 minute intervals thereby enabling detailed precipitation rate analysis. Wüest et al. (2009) recognized the timescale advantage of radar precipitation estimates and applied hourly radar analyses to rain gauge data to improve the temporal resolution of a rain gauge based

climatology for the Alps, but did not incorporate spatial advantages inherent to radar. Sub-hour radar-based precipitation rate was leveraged by Carbone et al. (2002) and Ahijevych et al. (2004) to investigate diurnal precipitation patterns in the continental United States. Germann et al. (2009) even demonstrates the usefulness of radar-derived precipitation rate estimation as an input to a real time hydrologic model for a mountainous region. The distribution of high precipitation rate is important to consider and included in this study because of the implications for flooding (Alamano et al., 2009).

This study is also distinguished by the complex terrain of the European Alps. Previously, a 10-year radar-based precipitation climatology of total precipitation and extreme precipitation events was developed for the relatively flat terrain of the Netherlands (Overeem et al., 2009a and 2009b). In earlier work, Schiesser et al. (1995) demonstrated the utility of radar for characterizing the structure of severe mesoscale precipitation systems over Switzerland for a 5-year period (1985-1989), but radar instrument capability has significantly improved since this work was published. Panziera and Germann (2010) demonstated the use of Swiss radar data from a single site to characterize airflow and precipitation rate for 58 orographic precipitation events occurring in the years 2004-2008. Here, the timespan is extended to the entirety of 2000-2008 and the data set is a composite of three Swiss radar sites (Fig. 2.1). Usage of ground-based radar in complex terrain presents many challenges. Obstacles faced by modern radar installations and associated verification of radar precipitation estimates in mountainous areas, specifically the central European Alps, are described in Germann et al. (2006, 2009).

## 2.2. Data and Method

### *2.2.a. Data*

Data from the operational Swiss Weather Service, MeteoSwiss, radar network forms the basis of this analysis. The radar network includes three C-band Doppler weather radars at Lema, Albis, and La Dole (located near Locarno, Zurich, and Geneva, respectively, see Fig. 2.1). Each of the radars scans 20 elevations every 5 minutes monitoring radar reflectivity up to a range of 230 km. MeteoSwiss composites the three Swiss radars to estimate surface precipitation in a data product called RAIN. RAIN provides a 30 minute running average of surface precipitation

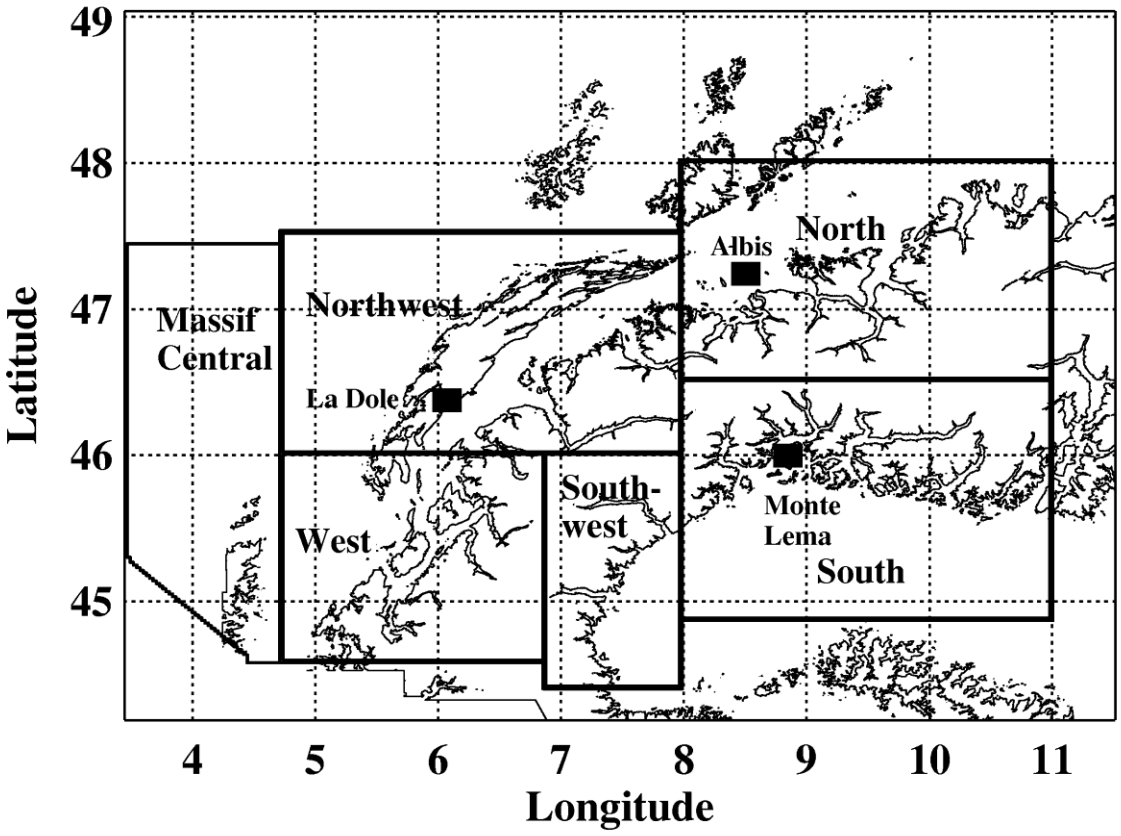


FIG. 2.1: Area of investigation covered by the three MeteoSwiss radars (locations indicated with squares): Albis, La Dole, and Monte Lema. The boundaries of the six investigation regions are shown with thick black lines. Thin lines indicate 800 m above sea level topographic contours.

rate on a 2 x 2 $km^2$ Cartesian grid and is updated every 5 minutes. Thorough descriptions of the Swiss radar network and data products are found in Joss et al. (1998), Germann and Joss (2004), Germann et al. (2006, 2009), and Panziera and Germann (2010). MeteoSwiss radar-based precipitation estimates incorporate multiple quality control measures including automatic hardware calibration; removal of ground clutter and false echoes; corrections for visibility to account for and properly weight pulse volumes that are not fully visible by the radar antenna; corrections for vertical profile of reflectivity to account for precipitation phase change and growth between the height of the visible measurement and the ground; and bias correction for non-uniform beam filling, low level growth unaccounted for by the vertical profile correction, and attenuation (Joss et al.,1998; Germann and Joss, 2004; Germann et al., 2006).

Precipitation fields derived from the Swiss radars are adjusted to rain gauge measurements on an annual basis. Analyses of measurement uncertainty revealed that the adjustment was most valuable when applied over a large space-time window, i.e., a single value for each year (Germann et al., 2006). Germann et al. (2006) have previously evaluated precipitation estimates from the Swiss radar network by comparison of total daily rain gauge and radar precipitation measurements and showed improvement over 1997-2004 that resulted in a global bias across the whole of Switzerland of -1.3% for the daily radar-gauge ratio for summer 2004. Germann et al. (2006) also quantifies localized bias between radar-estimated and rain gauge measured precipitation. Geographically, bias varies from 0.2% on the South side of the Alps near the Monte Lema radar to 13% in the interior of the Alps where the terrain is more complex.

### *2.2.b. Seasons and regions*

The time intervals defined for analysis of seasonal precipitation distribution and patterns are spring (March – May), summer (June – August), fall (September – November), and winter

(December – February, the year associated with the winter season is the year of January/February).

The Swiss Alps are divided into six regions to facilitate spatial analysis of the interaction between synoptic weather conditions and topography. The first requirement for defining the regions is that each is contained within the geographic boundaries of radar coverage. Secondly, the regions are defined such that they are roughly aligned with the main Alpine crest. With these requirements in mind, precipitation distributions are calculated for each season of 2000-2008 for the six regions shown in Fig. 2.1: Northern Alps (N), Southern Alps (S), Northwestern Alps (NW), Southwestern Alps (SW), Western Alps (W), and Massif Central (MC). The regions range in size from 15,000 to 40,000 $km^2$ (3700 to 10,000 pixels). It is noted that the NW, N, and S regions each contain one of the three radar sites, so data for these regions result from shorter distances and lower heights of the radar beam and have different data quality than the more distant MC region. Also noted is absence of a region covering the Eastern Alps due to lack of radar visibility.

### *2.2.c. Total precipitation*

Total daily precipitation is estimated at each pixel within each region by summing the estimated precipitation rate (mm/h) at the surface for each 30 minute period ($\text{Precip Rate}_{30\text{ min}}$) over the course of each day (Equation 2.1). The daily totals are then averaged over each season for all pixels in a given region to give average daily precipitation.

$$\text{Average daily precip.}\left[\frac{\text{mm}}{\text{d}}\right] = \frac{\sum_{\text{region}} \sum_{1}^{48\text{ observations /day}} \frac{\text{Precip Rate}_{30\text{ min}}}{2\text{ observations/hour}}}{\text{area of region}} \quad (2.1)$$

Equation 2.1 reveals a difference between the time series of average daily precipitation calculated here and time series of daily precipitation reported by rain gauge based climatologies.

The radar-based daily precipitation in this analysis is a temporal and spatial average of precipitation received at each pixel (representing 2 x 2 $km^2$) within a region; whereas, rain gauge based precipitation is generally reported as time-series for specific points which can be interpolated to provide regional precipitation averages.

*2.2.d. High precipitation rate*

The 30-minute time resolution of the radar-based precipitation rate data is leveraged to develop an analysis that includes precipitation rate as well as quantity. Therefore, in addition to total daily precipitation, the regional and seasonal distributions of high precipitation rate events are also investigated. Precipitation rate is analyzed in terms of geographic extent and duration of heavy precipitation, i.e., number of pixels having a precipitation rate greater than or equal to 20 mm/h over the course of a season, and is subsequently referred to as *frequency* of high precipitation rate, F (Equation 2.2).

$$F = \frac{\sum_{time} \sum_{region} \text{number of pixels with precip rate} \geq 20 \text{ mm/h}}{\text{area of region}} \qquad (2.2)$$

The 20 mm/h threshold is confirmed as a high, rarely-occurring value (extreme value) for precipitation rate by observing that over the period of 2000-2008 a precipitation rate of 20 mm/h or greater occurred in 0.39% of the sampled pixels that indicated occurrence of precipitation.

Although quality control (QC) measures are built into the dataset as described in Section 2.2.a., an additional measure was applied to the frequency of high precipitation rate data to further remove non-precipitating echoes. The QC procedure involved gathering frequency data during a time frame where no precipitation was received and radar reflectivity is related to clear air echoes. Pixels which showed a rain rate of greater than 8 mm/h during this time frame were omitted from the frequency of high precipitation rate analysis.

### *2.2.e. Synoptic weather patterns*

Distribution of total precipitation and high precipitation rate is generally coupled with the associated synoptic weather situation (e.g. Lin et al., 2001; Rudari et al., 2004). The identification of weather patterns most likely to result in the greatest daily precipitation and the most widespread occurrence of high precipitation rate allows prediction of future precipitation amounts related to changes in natural modes of the atmospheric circulations such as the North Atlantic Oscillation (NAO). Schüepp's weather classification is a system that provides daily categorization of the synoptic pattern in the central Alps from 1945-current. A detailed description of Schüepp's weather classification is provided by Schüepp (1979), Wanner et al. (1998), and Stefanicki et al. (1998). Schüepp's classification system is a subjective method because the weather pattern definitions are known in advance. It is used for this analysis because of its established usage in the Swiss Alpine area. Daily Schüepp's synoptic weather pattern classifications for the years 2000-2008 were obtained from MeteoSwiss.

The main three classes of the Schüepp system (convective, advective, mixed) are determined by the strength of the surface pressure gradient across a 444 km diameter centered in Switzerland at 46.5° N, 9° E. The convective type is characterized by lack of surface pressure gradient, and the advective classification is associated with the existence of a gradient in surface pressure larger than 5 hPa across the diameter. The mixed classification results when surface and 500 hPa pressure gradients are at odds (strong gradient at one level while weak at the other). The main classes are further divided into the following sub-classes: a) convective: high (CH), flat (CF), and low (CL) (based 500 hPa geopotential height relative to the annual mean); b) advective: north (AN), south (AS), east (AE), and west (AW), based on the direction of the 500hPA

geostrophic wind; and c) mixed (MIX): no further sub-classification. A final distinction into 40 weather situations is made by evaluating the angle between surface isobars and 500 hPa contours, and 500 hPa wind speed and geopotential height from soundings in Payerne, Switzerland; Milan, Italy; and Munich, Germany.

The 1000 hPa and 500 hPa geopotential height maps are generated for Schüepp's classifications that are herein identified as associated with days having high total precipitation or frequency of high precipitation rate. The geopotential data were retrieved from the European Centre for Medium-Range Weather Forecasts (ECMWF) Re-Analysis (ERA) Interim dataset with a horizontal resolution of 1.5° x 1.5°.

## 2.3. Results and Analysis

### *2.3.a. Total precipitation*

Total precipitation for each region is compared within each season to indicate which region has the highest precipitation amount over the years 2000-2008 (Fig. 2.2). The SW has the highest median value in winter, spring, and fall and is among the group of regions having the greatest average daily precipitation for all seasons (based on pairwise comparison using t-test with 95% confidence). However, the N region has highest median in summer. The W and MC regions are consistently in the group with the lowest median values of total precipitation in all seasons. Also, the maximum values of total precipitation in each region qualitatively follow the same pattern as the distribution of median values for each region.

To indicate which season provides the highest values of total precipitation each season is compared within each region (Fig. 2.3). Summer has the highest median and maximum value of total precipitation for all regions and is the wettest season in all regions with median values of total precipitation for summer more than twice winter median values. The SW is the exception

where a significant difference does not exist between any pair of seasons (at 95% confidence level, Fig. 2.3). The result agrees with Frei and Schär (1998) who also reported summer to be the wettest season across the Alps, with the exception of the southwestern Alps where minimal seasonal differences were found.

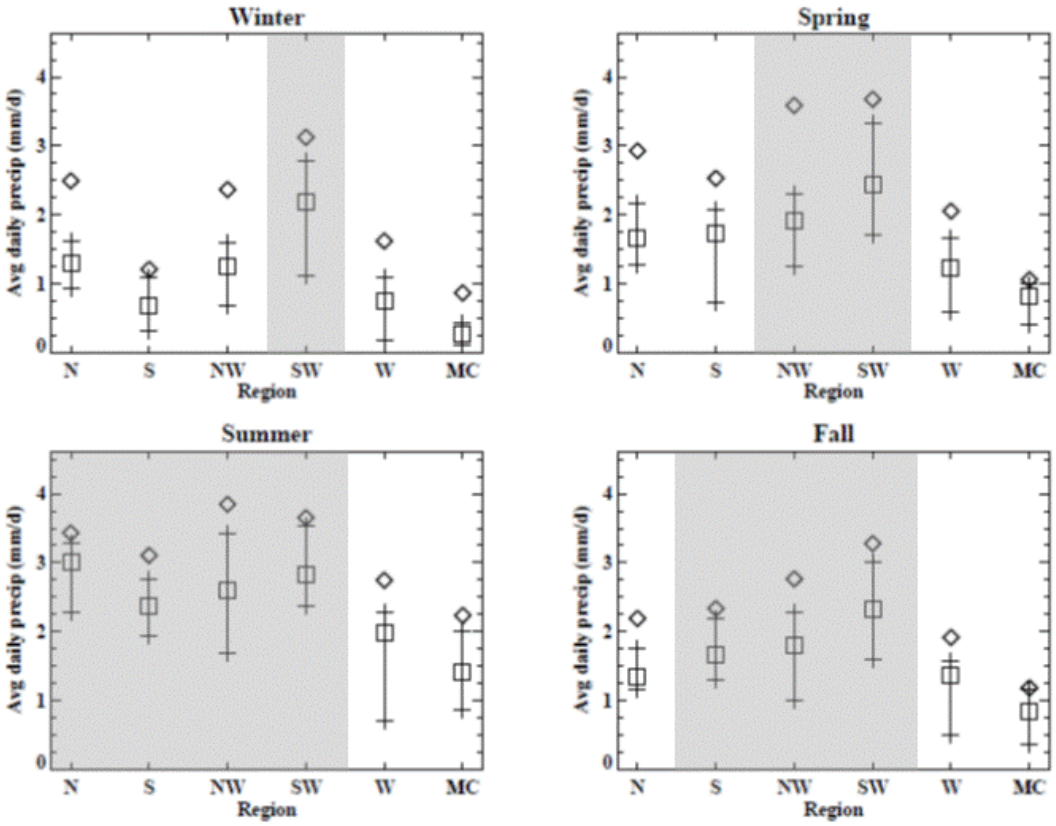


FIG. 2.2: Average daily precipitation for each season between the years 2000-2008 is plotted as a function of region. Diamonds indicate maximum values, boxes indicate median values, and the lines indicate interquartile range at the hash marks (within each region). The regions receiving the most total precipitation during each season are shaded gray (based on pairwise comparison with 95% confidence as discussed in Section 2.3.a.).

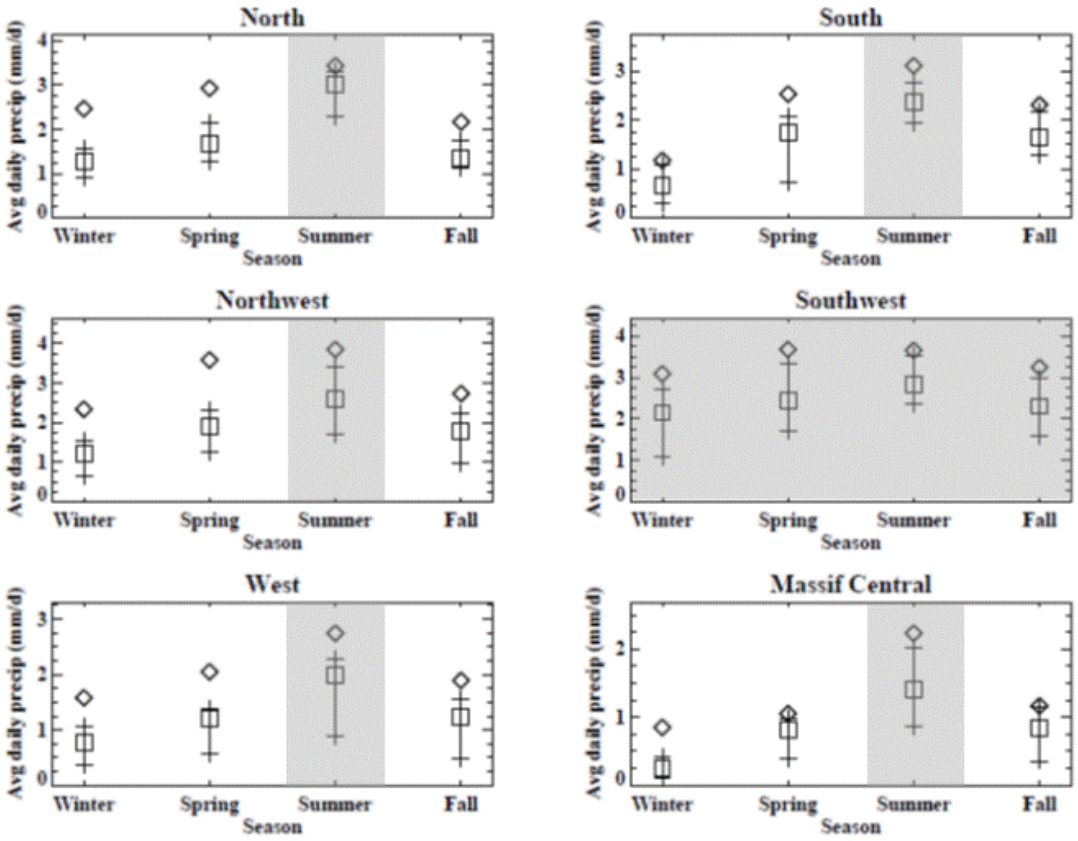


FIG. 2.3: Average daily precipitation between the years 2000-2008 is plotted for each region as a function of season. Diamonds indicate maximum values, boxes indicate median values, and the lines indicate interquartile range at the hash marks (within each season). The seasons receiving the most total precipitation within each region are shaded gray (based on pairwise comparison with 95% confidence). Note the scale differences on the y-axis for the various regions.

The 10-day running mean (-5 day/+4 day) of total daily precipitation averaged over 2000-2008 as shown in Fig. 2.4 provides some insight into the relative seasonal values of total precipitation. Each region follows a similar annual cycle. Daily precipitation reaches its minimum during winter, steadily increases during spring, reaches maximum values during the summer, begins to decrease in late summer, and remains at lower values with more variability during fall as compared to summer. Late spring and early-mid fall both contain individual days which have similar total precipitation in several regions as the summer season; however, when averaged together with drier days earlier in spring and later in fall, both seasonal means of total

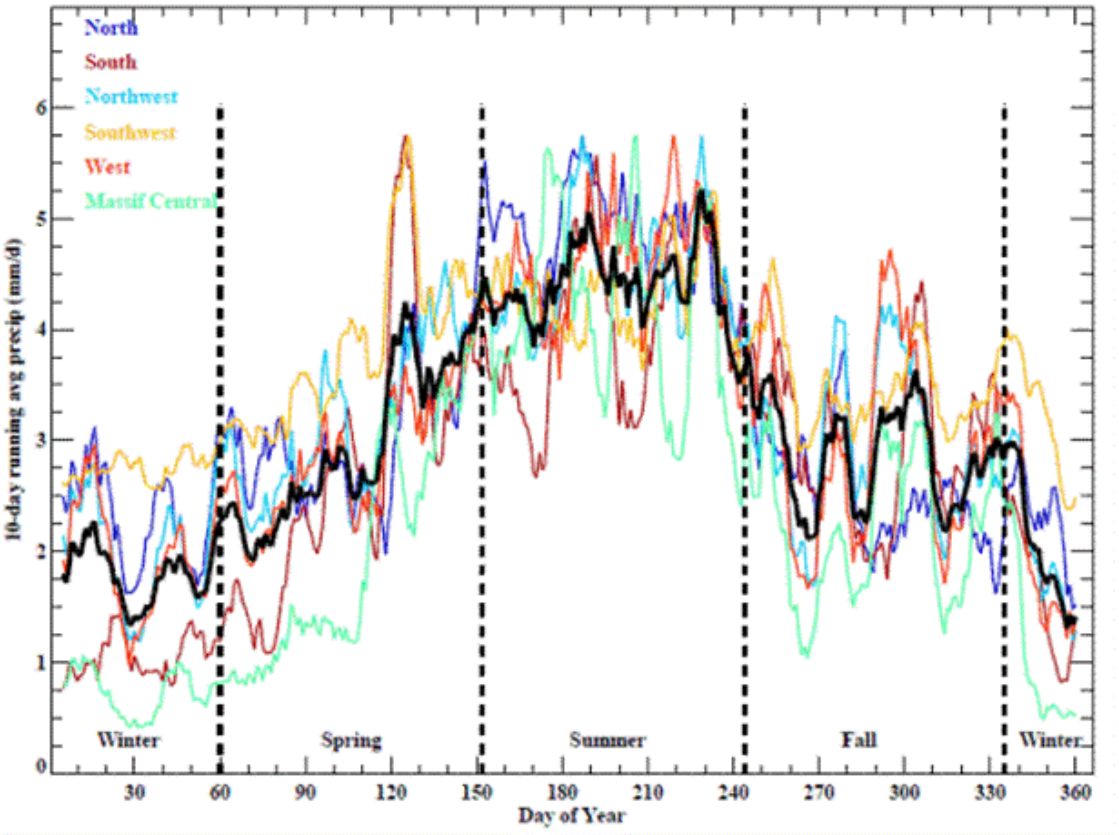


FIG. 2.4. 10-day running average daily precipitation received over the years 2000-2008 is plotted for each day of the year and for each region. The 10-day running average over all regions is indicated by the black line.

precipitation are less than summer which culminates in the relative mean values of the seasonal distributions (Fig. 2.3). The high variability of total precipitation in spring and fall may be reflective of the increased occurrence of strong southerly flow that results in heavy precipitation and flooding during April/May and October/November as reported by Grazzini (2007). Most of the heavy precipitation events, especially in spring and fall, are linked to upper-level troughs (Lin et al. 2001; Rudari at al. 2004). The lee cyclone, also called the Genoa cyclone, forms in the lee of the southern Alps close to the city of Genoa, Italy. This weather situation first causes heavy precipitation on the southern side of the Alps followed by heavy precipitation on the northern side (e.g., areas of Switzerland received 200 - 300 mm of precipitation over a five day period during the August 2005 flood; Hohenegger et al., 2008).

### *2.3.b. Frequency of high precipitation rate*

In order to provide insight into local areas of maximum precipitation rate and the spatial distribution within each region the number of occurrences of precipitation rate exceeding 20 mm/h is summed at each pixel over each season (resulting in resolution of 2x2 $km^2$). Figure 2.5 is shown as an example of the output generated for each season of 2007. In 2007 summer was the season with the largest area having experienced a precipitation rate greater than 20 mm/h. The area south of the Alps contained more numerous and widespread high precipitation events compared to the other regions and seasons. Spring was the season with the second largest area of high precipitation rate over the Alps. The Lago Maggiore area in the southern region of the Alps had the greatest frequency of high precipitation events in spring, summer, and fall of 2007. Frequency of high precipitation rate, i.e., total seasonal count of pixels that exceed a precipitation rate of 20 mm/h divided by the surface area of each region, is summarized for each region and season over 2000-2008 in Fig. 2.6. Larger values indicate greater geographic extent, or combined effect of widespread and frequent, high precipitation events. The overall maximum frequency of high precipitation rate observed (summer in the NW region, Figs. 2.6 and 2.7) results both from increased horizontal distribution of high precipitation rate events, meaning that more surface area received at least one instance of high precipitation rate, and increased occurrence of high precipitation rates in localized areas, specifically north and northwest of the Alps. Summer months have the highest frequency in all regions over the period of 2000-2008 while winter has the lowest frequency (Figs. 2.6 and 2.7). The S region has the highest overall mean frequency value (all seasons, not shown) while the W region has the lowest overall mean frequency.

In contrast to total precipitation shown in Fig. 2.2, seasonal comparison of frequency of high precipitation rate between each region with 95% confidence shows the most high precipitation rate events in winter occur in the N region (Fig. 2.6). In spring and summer, the W region has the least frequency of high precipitation rate events, and in fall the S and SW regions have the greatest frequency of high precipitation rate events.

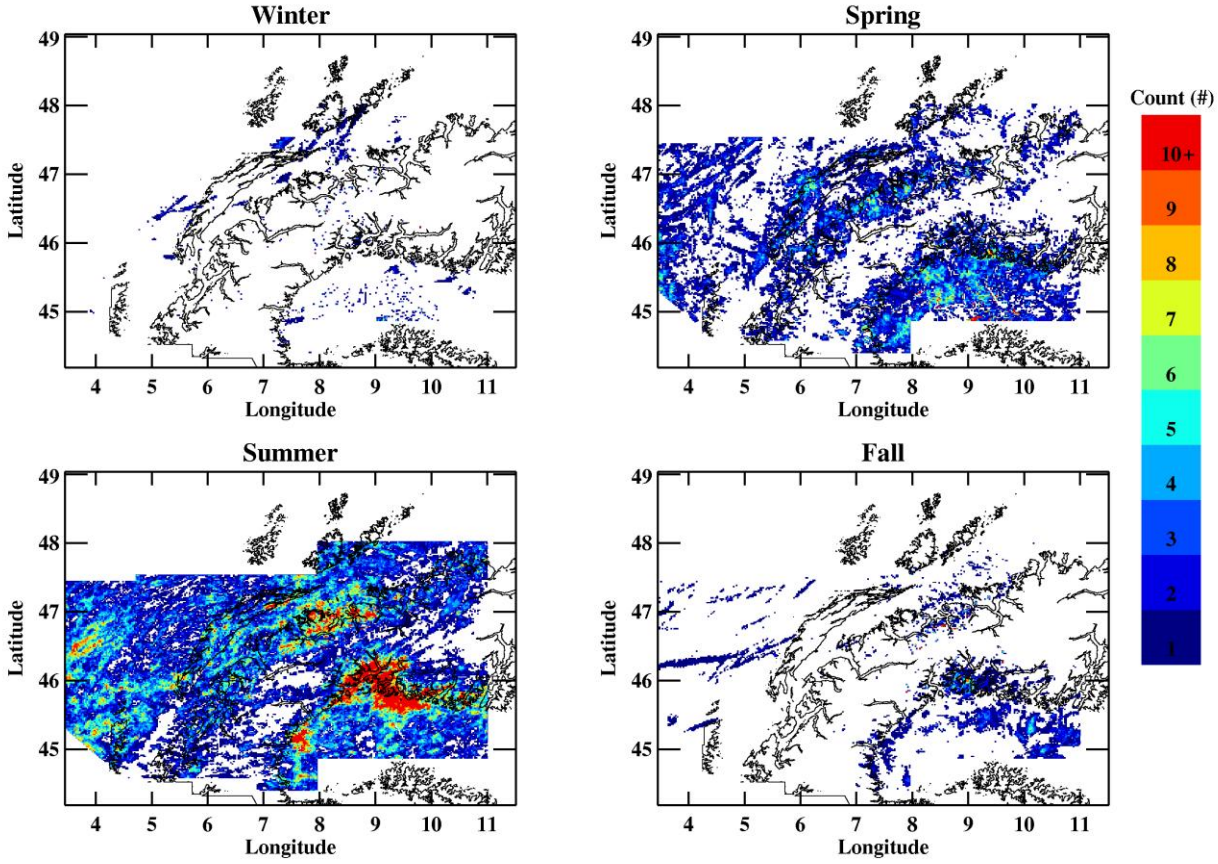


FIG. 2.5. Horizontal distribution of high precipitation rate frequency (number of occurrences of precipitation rate greater than 20 mm/h) is plotted for all seasons of 2007. Black lines indicate 800 m above sea level topography.

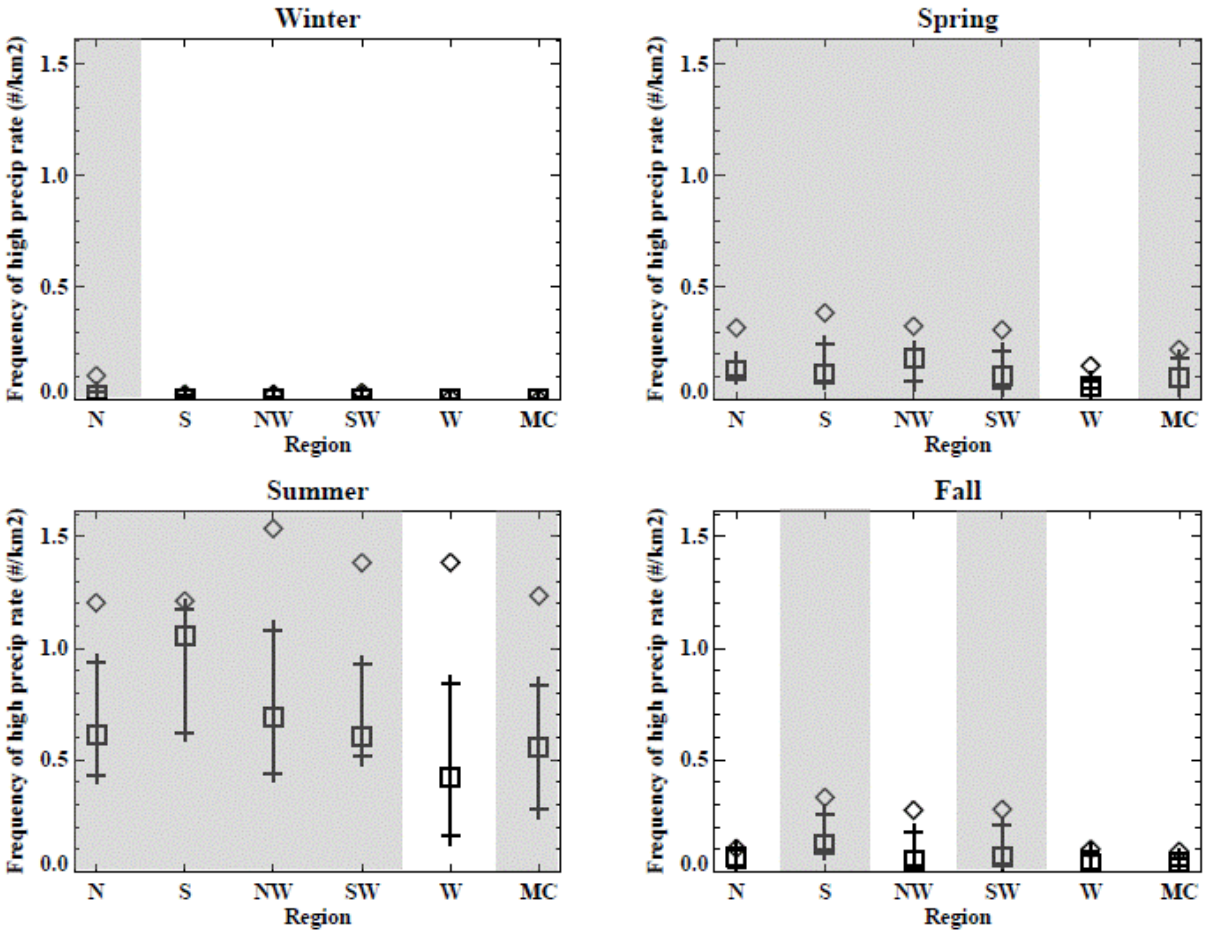


FIG. 2.6. Frequency of high precipitation rate for each season between the years 2000-2008 is plotted as a function of region. Diamonds indicate maximum values, boxes indicate median values, and the lines indicate interquartile range at the hash marks (within each region). The regions with the greatest frequency of high precipitation rate events during each season are shaded gray (based on pairwise comparison with 95% confidence).

Comparison of the frequency of high precipitation rate between seasons (with threshold set at 20 mm/h for all seasons) within each region shows that frequency in summer is significantly different than each of the other seasons in all regions (Fig. 2.7). Spring, fall, and winter are not found to be significantly different. Therefore, in general, summer has the most widespread occurrence of high precipitation rate events, and the result is consistent with previous studies that show the majority of severe mesoscale convective systems and heavy precipitation events in Switzerland occur during summer (Schiesser et al., 1995; Laing and Fritsch, 1997).

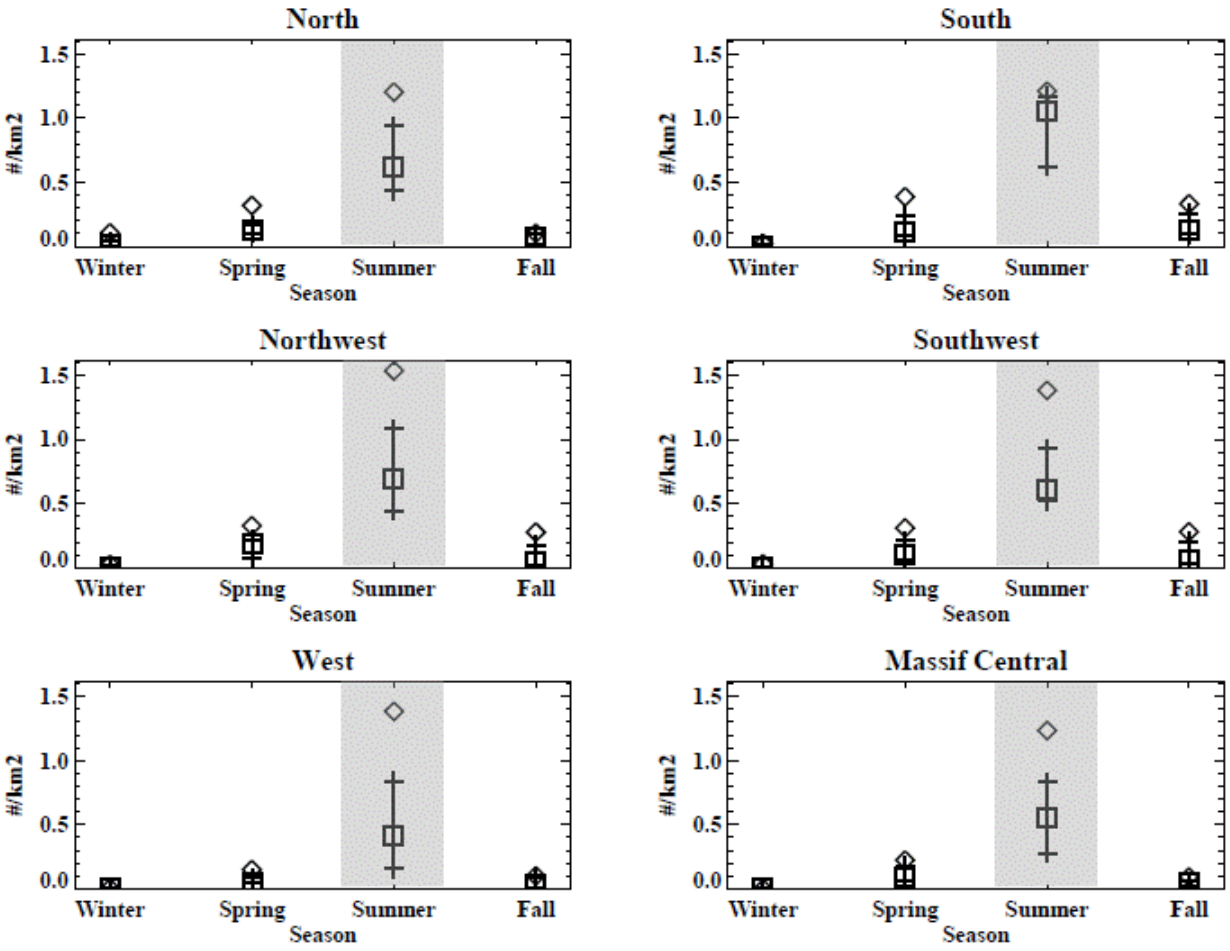


FIG. 2.7. Frequency of high precipitation rate between the years 2000-2008 is plotted for each region as a function of season. Diamonds indicate maximum values, boxes indicate median values, and the lines indicate interquartile range at the hash marks (within each region). The seasons with the greatest frequency of high precipitation rate events in each region are shaded gray (based on pairwise comparison with 95% confidence).

### *2.3.c. Correlation of synoptic weather pattern to total precipitation and high precipitation rate*

As already discussed in Sections 2.2.e and 2.3.a. most of the precipitation in the Alps is related to the synoptic scale weather pattern. If the 9-year (2000-2008) precipitation distribution presented here is related to synoptic weather patterns, it may enable prediction of future precipitation amounts and occurrence of high precipitation rate based on changes in occurrence of synoptic weather patterns as predicted by climate models. First, the synoptic weather patterns are identified corresponding to the highest median and $90^{th}$ quantile (Q90) of total daily precipitation and frequency of high precipitation rate for each region over the years 2000-2008 (Table 2.1). Days characterized by an advective pattern have both the highest median and Q90 of total daily precipitation. This implies that advective patterns are associated with the highest values of total daily precipitation. Furthermore, the AS pattern accounts for the highest median and Q90 values of total daily precipitation in all regions, except the N. Advective patterns in the Schüepp classification exhibit a surface level pressure gradient and are further classified by the direction of the 500 hPa geostrophic wind. The AS pattern is generally associated with a mid-tropospheric southerly flow that carries moist air from the Mediterranean toward the Alps and provides the necessary moisture to result in large daily totals of precipitation as shown in Fig. 2.8. The sub-categories of the advective Schüepp's classification are limited to four cardinal directions (north, south, east, west), and the AS pattern includes advection from the southwest, as well as the south, while advection from the southeast is classified as AE (Schüepp, 1979; Wanner et al., 1998; Stefanicki et al., 1998).

| | Total Daily Precipitation | | Frequency of High Precipitation Rate | |
|---|---|---|---|---|
| Region | Largest Median | Largest Q90 | Largest Median | Largest Q90 |
| North | AN | AW | CF,CH | CH |
| South | AS | AS | CF | MIX |
| Northwest | AS | AS | CH | CH |
| Southwest | AS | AS | CH | CH |
| West | AS | AS | CH | CH |
| Massif Central | AS | AS | CH | CH |

TABLE 2.1. Schüepp's weather classifications corresponding to largest median and largest 90% quantile values for total daily precipitation and frequency of high precipitation rate are shown for each region for the years 2000-2008. Synoptic weather pattern abbreviations are as follows: AN: advective north; AS: advective south; AW: advective west; CF: convective flat; CH: convective high; MIX: mixed.

Figure 2.8 shows the 1000 and 500 hPa geopotential height contours averaged for the five days classified as AS that produced the greatest amount of total daily precipitation as indicated by operational radar across all regions during the years 2000-2008. The surface pressure gradient across Switzerland leads to the advective classification while the SSW 500 hPa geostrophic wind direction further classifies the situation as AS. The predominant feature is the passage of an upper-level trough west of the Alps that usually extends from England to the Mediterranean and causes moist flow from over the Mediterranean to interact with the Alpine topography to result in heavy precipitation. In addition, the westward movement of the trough is slowed by a ridge to the east of the Alps. The synoptic situation displayed in Fig. 2.8 is similar to the elongated trough, or potential vorticity streamer, described as an ingredient for heavy Alpine precipitation in Doswell et al. (1998), Massacand et al. (1998), Lin et al. (2001), Martius et al. (2006), Grazzini (2007), and references within. Although the North Atlantic has been identified as the greatest contributor of moisture to annual precipitation for the overall Alpine

area (Sodemann and Zubler, 2010), the association of the AS pattern with the highest daily values of precipitation suggests that the Mediterranean is the moisture source that produces the largest daily totals of precipitation across the Alpine area, with the exception of the North region.

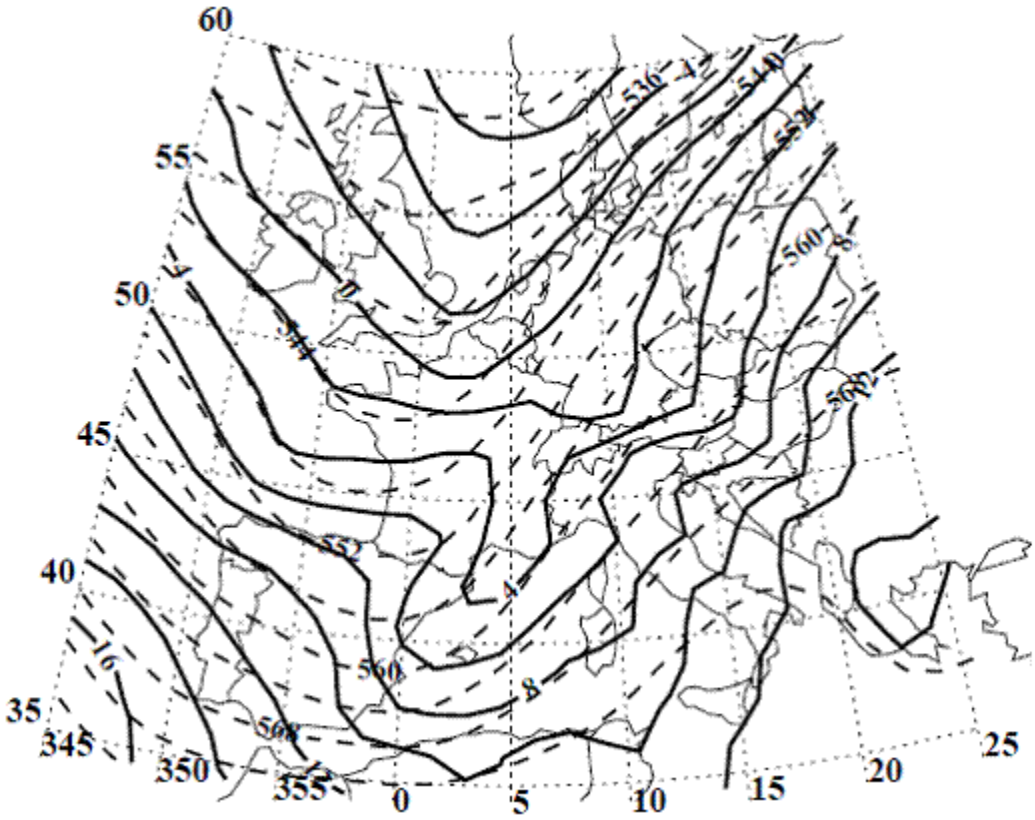


FIG. 2.8. The 1000 hPa geopotential height (solid contours, units are dm) and 500 hPa geopotential height (dashed contours, units are dm) averaged for the top five total precipitation days during the years 2000-2008 (26 October 2004, 31 October 2003, 13 July 2008, 8 December 2006, 6 December 2006) classified as advective south Schüepp's weather pattern.

Days characterized by a convective pattern account for the both the greatest median and Q90 of high precipitation rate frequency in all regions (Table 2.1). Therefore, across all regions, convective patterns are associated with the greatest geographic extent of high precipitation rate. In fact, the CH pattern accounts for the greatest median and Q90 values of high precipitation rate frequency in all regions, except for the S region. Convective patterns are characterized by a dome or ridge of high pressure at the surface that creates a weak pressure gradient and subsequently results in light low-level geostrophic winds. Weak surface-level winds may allow localized convective systems producing high precipitation rates to develop, thereby, enabling the relationship between a convective synoptic pattern and high precipitation rate.

Figure 2.9 shows the 1000 and 500 hPa geopotential height contours averaged for the five days classified as CH that produced the greatest frequency of high precipitation rate as indicated by operational radar across all regions for the years 2000-2008. The convective classification is associated with minimal surface pressure gradient across Switzerland (Fig. 2.9). The CH sub-classification is determined when the 500 hPa geopotential height is in the upper quartile of the mean annual distribution of 500 hPa heights for soundings from Payerne, Milan, and Munich. Since the majority of high precipitation rate events are found in the warm summer season, as evidenced here and also in Schiesser et al. (1995), it is not surprising that the associated 500 hPa geopotential heights are in the upper quartile. Also notable in Fig. 2.9 is the southwesterly geostrophic wind at 500 hPa. Again, similar to the advective situation, the southerly component of the mid-tropospheric flow carries moisture from the Mediterranean toward the Alps. Vertical wind shear, as indicated by the difference in geostrophic wind between the surface and mid-troposphere, also creates an environment favorable for development of intense storms capable of producing high precipitation rates (Weisman and Klemp, 1984).

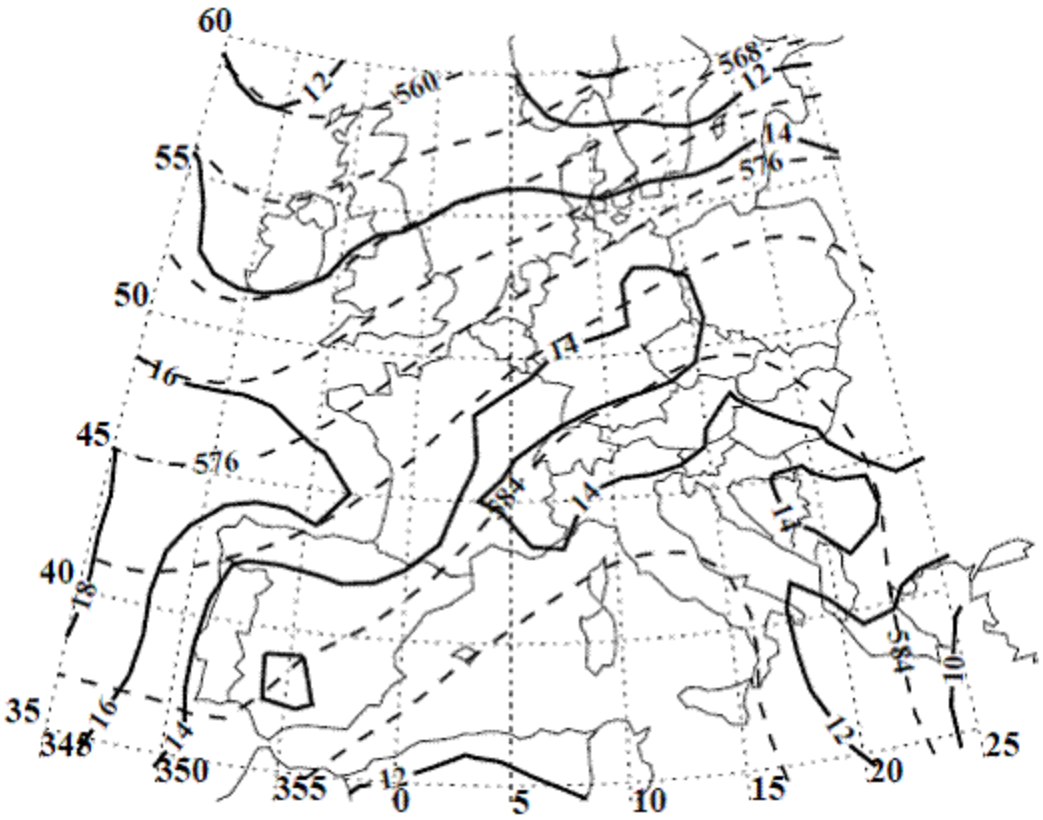


FIG. 2.9. The 1000 hPa geopotential height (solid contours, units are dm) and 500 hPa geopotential height (dashed contours, units are dm) averaged for the top five frequency of high precipitation rate days during the years 2000-2008 (24 June 2005, 12 July 2006, 20 June 2007, 12 June 2003, 27 June 2006) classified as convective high Schüepp's weather pattern.

The relationship between total precipitation and frequency of high precipitation rate is analyzed with conditional probability. Specifically, the conditional probability that a given day is above the 90$^{th}$ quantile for total precipitation given that the frequency of high precipitation rate is above the 90$^{th}$ quantile, noted as P(total90|rate90) is defined as:

$$P(\text{total90} \mid \text{rate90}) = \frac{P(\text{total90} \cap \text{rate90})}{P(\text{rate90})} \qquad (2.3)$$

The conditional probability, P(total90|rate90) , is a measure of the causal effect of high precipitation rate on large amounts of total daily precipitation. Larger values indicate that high precipitation rate (in this case ≥ 20 mm/h) contributes more to total precipitation. Likewise, smaller conditional probabilities result when large quantities of total precipitation result from longer duration, lower precipitation rate events.

Figure 2.10 shows conditional probability, P(total90|rate90), for each Schüepp synoptic pattern and region. The convective high pattern (CH) has the highest conditional probabilities for all regions. Therefore, under a CH synoptic pattern, high precipitation rates are more likely to result in large quantities of total precipitation. In contrast, the advective south (AS) synoptic pattern has lower conditional probability for each region, an indication that large quantity precipitation events occurring in an AS pattern are associated with persistent precipitation at lower rates.

Figure 2.11 further illustrates the use of conditional probability in evaluating the relationship between precipitation rate and quantity. Frequency of high precipitation rate is plotted against total daily precipitation for the South region for days classified as AS and CH with the 90$^{th}$ quantile (Q90) values for frequency of high precipitation rate and total daily precipitation indicated with dashed lines. Data points in the upper right sector demarked by the 90$^{th}$ quantile

lines are values that are above the 90th quantile for both precipitation rate and quantity. For the AS pattern, the values greater than Q90 for total precipitation are dispersed across both sides of the Q90 line for precipitation rate. However, the CH pattern exhibits a stronger relationship between total precipitation and precipitation rate, thereby explaining the larger conditional probability for the CH pattern as shown in Fig. 2.10.

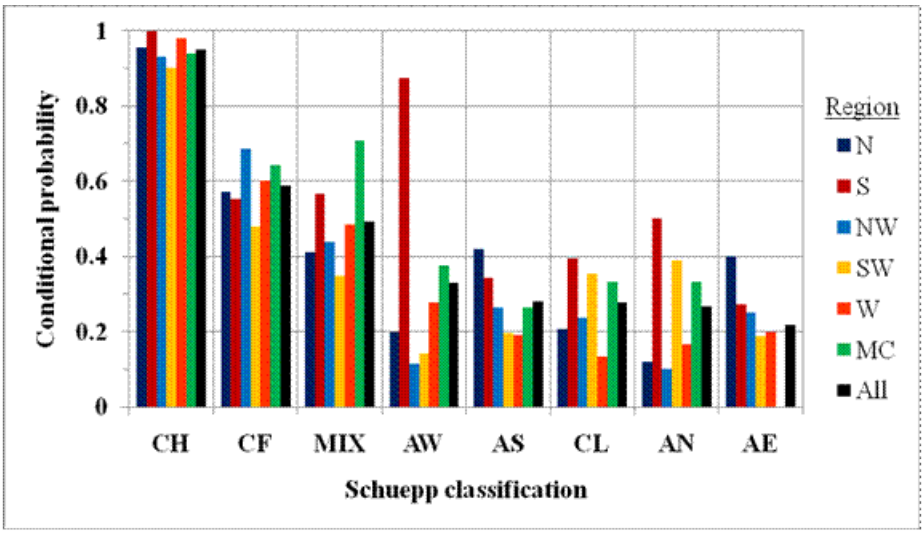


FIG. 2.10. Conditional probability that daily total rainfall (mm/d) is above the 90th quantile given that the frequency of high precipitation rate (#/km$^2$) for the day is above the 90th quantile for each Schüepp synoptic classification and region.

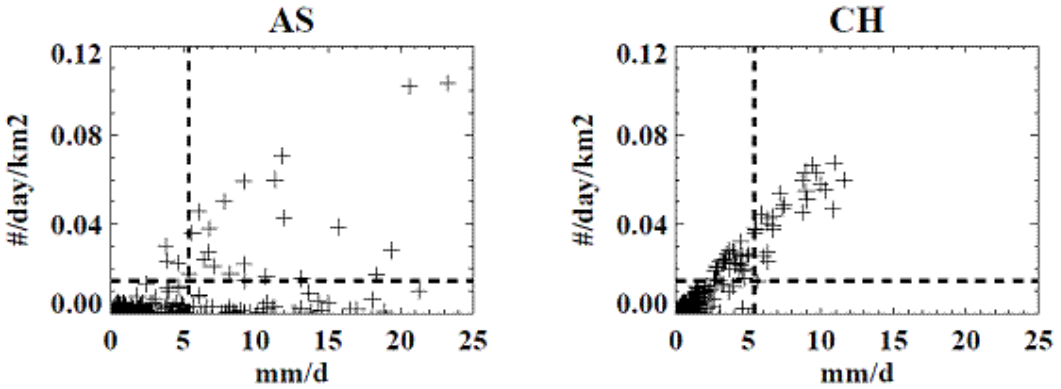


FIG. 2.11. Frequency of high precipitation rate for each day (#/day/km$^2$) is plotted vs. total daily precipitation (mm/d) for the South region. Days classified as advective south (AS) are shown on the left and days classified as convective high (CH) are show on the right. The data include all days over the years 2000-2008. The vertical dashed line is the 90th quantile of total daily precipitation for the South region and the horizontal dashed line is the 90th quantile for frequency of high precipitation rate.

Table 2.2 shows the relative frequencies of the main Schüepp weather classifications for the period of 1945-1994 (as reported in Wanner et al., 1998) and also for the period of 2000-2008. The data indicate an increased frequency of convective days at the expense of a decrease in advective days. The increase in convective days and decrease in advective days for 2000-2008 as compared to 1945-1994 is consistent with trends reported in Stefanicki et al. (1998). Based on the association of convective patterns with high precipitation rate and relationship between precipitation rate and total precipitation for convective patterns, it may be expected that an increasing frequency of convective patterns will lead to intense precipitation events accounting for a greater portion of total precipitation. In fact, several studies provide evidence that extreme events are increasing in probability and increasing their contribution to total seasonal precipitation amounts (Klein Tank and Können, 2003; Groisman et al., 2005; Zolina et al., 2010).

| Schüepp Classification | 1945-1994 | 2000-2008 |
|---|---|---|
| Convective | 0.51 | 0.57 |
| Advective | 0.43 | 0.36 |
| Mix | 0.06 | 0.07 |

TABLE 2.2. Frequencies of main Schüepp's weather classifications are shown for the period 1945-1994 (Wanner et al., 1998) and 2000-2008.

### 2.4. Summary and Conclusions

A 9-year (2000-2008) analysis of precipitation for the central and western European Alps has been assembled from Swiss operational radar data. Six regions aligned with the general topography of the Alps and the radar coverage were established to enable sub-analysis at the 100s of km scale. The seasonal distribution of total daily precipitation and the frequency of high precipitation events were characterized on the basis of radar-estimated precipitation rate at the surface.

Total daily precipitation was found to follow a similar annual time series across all regions with minimum values in the winter, steadily increasing during the spring, consistently at the highest values in the summer, and then decreasing in late summer and more variable throughout the fall. The SW region exhibits less of a seasonal trend in daily precipitation and also is among the regions that received the most total precipitation per $km^2$ in all seasons. For all regions, high precipitation events (precipitation rate $\geq$ 20 mm/h) were most frequent in summer and least frequent in winter over the years 2000-2008.

The highest median and Q90 values of total daily precipitation occurred on days with advective synoptic weather patterns, a synoptic situation that carries moist air from the Mediterranean toward the Alps. A convective synoptic weather classification having minimal surface pressure gradient was associated with the highest median and Q90 values of high precipitation rate frequency. Under a convective high synoptic pattern all regions are more likely to receive large total amounts of precipitation resulting from high precipitation rate. Conversely, under an advective south pattern large amounts of total daily precipitation are more likely to result from longer duration, lower intensity precipitation rates.

A potentially more valuable and available extension of this analysis is application of the radar-based precipitation distribution at the resolution of the base data (2x2 $km^2$), and therefore, potential use as a catchment- or glacier-specific precipitation characterization (Machguth et al., 2009). Furthermore, a probability distribution of precipitation at each grid point is envisioned which, when related to synoptic weather patterns, provides precipitation distribution and frequency for potential use in coupling catchment-scale hydrologic models to coarser-resolution climate models. Relating the operational radar-based precipitation analysis to climate models also provides opportunity for assessment and validation of downscaled climate model

precipitation output, such as in Smiatek et al. (2009) where multiple regional climate models for the European Alps are reported, but not thoroughly compared, due to lack of high resolution precipitation data. Finally, additional future work is planned to leverage the three-dimensional spatial nature of radar data to study features of vertical structure such as melting layer and distribution of precipitation type (snow/rain).

# CHAPTER 3
# MODEL-BASED ESTIMATION OF DYNAMIC EFFECT ON 21ST CENTURY PRECIPITATION FOR SWISS RIVER BASINS

## 3.1. Introduction and Background

Precipitation is a primary component of the hydrologic cycle and has significant implications for fresh water supply and storage, as well as flooding. Quantitative Precipitation Forecasts (QPFs) and Quantitative Precipitation Estimates (QPE) are critical inputs to hydrologic forecasts because of the direct connection between the spatial and temporal distribution of precipitation and resulting runoff. The Mesoscale Alpine Programme Demonstration of Probabilistic Hydrological and Atmospheric Simulation of flood Events (MAP D-PHASE) is an example of a collaborative atmospheric and hydrologic sciences effort to incorporate QPE and QPF into hydrologic forecasts for the European Alps (Ranzi et al. 2007; Zappa et al. 2008). A primary goal of MAP D-PHASE is operational forecasting of Alpine flood events through improvement of single to multi-day hydrologic forecasts. Forecasts with short time horizons (hours to days) are typically used for tactical actions such as warning and minimization or prevention of floods, similar to the objectives of MAP D-PHASE. However, hydrologic forecasts with longer time horizons are also important for water resources management (Table 3.1; adapted from Webster et al. 2010). Long-term forecasts (seasonal, annual, and even decadal) provide a basis for strategic water resource planning, such as development of management policy or investment in infrastructure.

As the time horizon for QPF is extended it becomes important to consider precipitation climatology. Long-term hydrologic forecasting has traditionally been based upon a climatology that includes observed historical precipitation distribution with an assumption of climate stationarity over time. However, it is now realized that as climate changes it is not valid to base water resource planning on static, historical precipitation distributions (Milly et al. 2008;

Gilleland and Katz 2011; Hirsch 2011). It has become critical to develop an understanding of how precipitation may be affected in a changing climate, so that water management strategy may adapt, if necessary.

| Forecast period | Time horizon | Usage |
|---|---|---|
| immediate, "nowcast" | present - hourly | tactical |
| short-term | daily | tactical |
| intraseasonal | weekly | tactical/strategic |
| seasonal | monthly | strategic |
| long-term | yearly - decadal | management strategy & policy development, infrastructure requirements |

TABLE 3.1: Hydrologic forecast periods are listed with applicable time horizons and typical usage in water resource management (adapted from Webster et al. 2010).

So how can we generate long-term precipitation forecasts at spatial resolution relevant to river basin hydrologic forecasts in a changing climate? Various methods of downscaling have been applied to this problem. Current methods for downscaling regional precipitation distribution are categorized as dynamical or statistical (Schmidli et al. 2007, and references within). Dynamical downscaling uses regional climate models (RCMs) to directly obtain high resolution atmospheric data at the desired grid spacing. For example, Smiatek et al. (2009) ran multiple RCMs for the European Alps with spatial resolution ranging from approximately 5-20 km. The study concluded that lack of high resolution precipitation observations prevented model validation and limited the use of models for evaluating trends in future precipitation due to climate change (Smiatek et al. 2009). In statistical downscaling, lower resolution data, either from observations or numerical models, are extrapolated or interpolated, as required, to deduce precipitation distributions at the desired spatial scale. Statistical downscaling of precipitation

data over complex alpine terrain is often accomplished by applying functions to account for spatial variations in temperature, elevation, or aspect to convert low resolution data into a high resolution grid. For example, Machguth et al. (2009) calculated inputs to glacier mass balance for the Swiss Alps by downscaling RCM precipitation from ~18 km grid spacing to 100 m resolution via application of topography-based temperature and precipitation lapse rates. A spatial resolution of 100 m was chosen because variation in orographic precipitation significant to glacier mass balance occurs at a scale from less than one to a few kilometers (Machguth et al. 2009). Model results were compared to observations at 14 weather stations, and it was found that errors in model output, including errors due to localized precipitation variability, were significant enough that the model did not provide reliable glacier mass balances (Machguth et al. 2009). Therefore, validation of both statistical and dynamical downscaled models has proven challenging, either because of model inaccuracy in reproducing climate effects that occur at small spatial scales or due to unavailability of high resolution observations for comparison. As a result, long-term QPFs relevant to river basin hydrological forecasts remain highly uncertain.

What if we develop a long-term QPF by direct association of high-resolution observations with a climate model? This approach provides an alternative to downscaled models for obtaining a long-term QPF, and is investigated in this study by coupling high resolution precipitation observations (~2 km) with a coarser resolution (~100 km) global climate model (GCM). The result is a 90-year precipitation outlook at a spatial scale relevant to river basins and catchments that takes into account the effects of changes in global circulation due to climate change. High-quality multi-year radar data are used to estimate future precipitation throughout the 21$^{st}$ century for seven major river basins in Switzerland. Previously, the high spatial and temporal resolution of operational radar has been leveraged in development of immediate term precipitation forecasts

used in hydrologic "nowcasting" (Germann et al. 2009; Panziera and Germann 2010). Now, we apply the spatial and temporal resolution advantages of radar estimated precipitation to a long-term QPF.

In this paper, synoptic weather patterns are used as the link between precipitation observations and GCM representation of future climate since the spatial distribution of total daily precipitation has been shown to be related to the associated synoptic weather situation (Lin et al. 2001; Plaut and Simonnet 2001; Rudari et al. 2004; Rudolph et al. 2011). By using future changes in the occurrence of synoptic patterns to quantify future changes in precipitation the dynamic effect of climate change on future precipitation is evaluated. Thermodynamic effects are not addressed in this study; however, it is recognized that a warmer atmosphere is likely to have greater water content (via the Clausius-Clapeyron equation) that can combine with dynamic effects to impact precipitation distribution (Trenberth et al. 2003; Seager et al. 2010).

### 3.2. Data and Methods

Figure 3.1 outlines the process used in this paper to calculate expected precipitation for Swiss river basins in the 21st century. Four data sets are used in this analysis:

1) daily synoptic weather pattern (DATA1 in Fig. 3.1) between 1948-2008 as determined by MeteoSwiss (Swiss Weather Service) per Schüepp's classification method (Schüepp 1979)
2) reanalysis data from the European Centre for Medium-Range Weather Forecasts (ECMWF) Re-Analysis Interim (ERAi) data set for 2000-2008 (DATA2 in Fig. 3.1)
3) surface precipitation estimated by MeteoSwiss operational radar network for 2000-2008 (DATA3 in Fig. 3.1)

4) output from the National Center for Atmospheric Research (NCAR) Community Climate System Model Version 3.0 (CCSM3) for Intergovernmental Panel on Climate Change (IPCC) scenario A1B for 1948-2099 (DATA4 in Fig. 3.1; CCSM3 experiment b030.040e, atmosphere post-processed data, daily averages, version 1; Collins et al. 2006; Solomon et al. 2007) . The IPCC Fourth Assessment Report (AR4) projects scenario A1B will result in a mid-to-upper range global surface temperature increase as compared to other IPCC scenarios for the years 2090-2099 as compared to 1980-1999 (Solomon et al. 2007).

Observational and model data from three time frames are referenced in this analysis: 1) historical, referring to the years 1948-1999; 2) current, referring to 2000-2008; and 3) future, referring to 2010-2099.

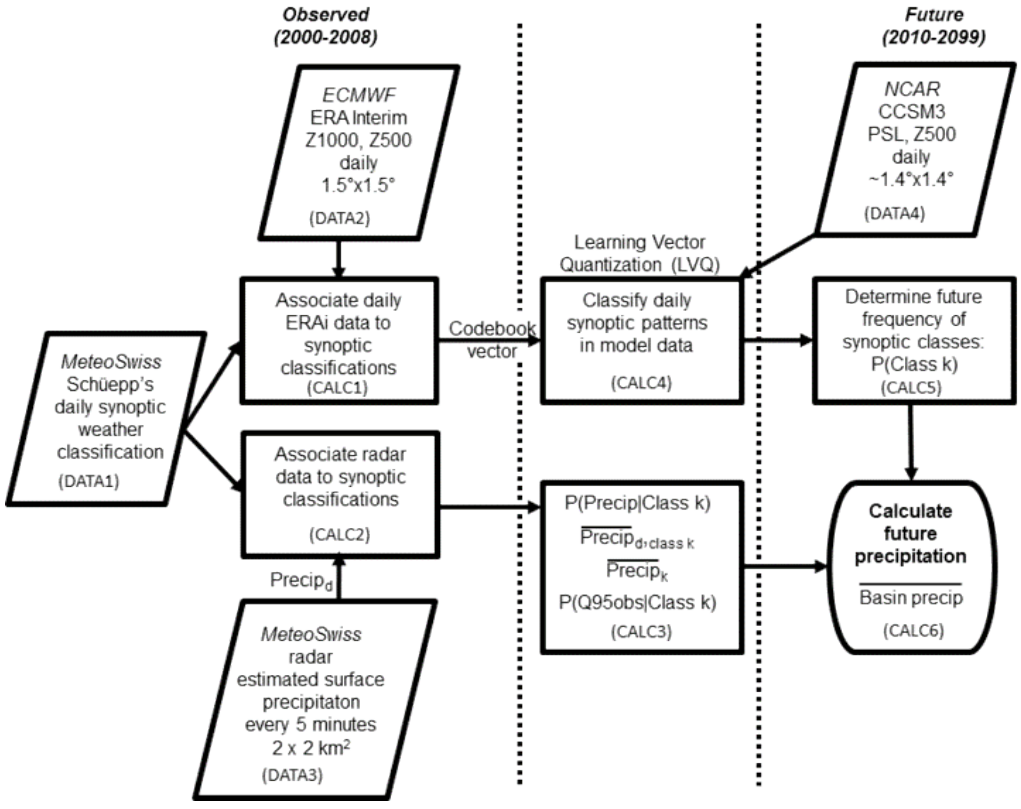


FIG. 3.1: Process for using synoptic weather patterns to couple radar-estimated precipitation with global climate model (GCM) to determine future precipitation.

### *3.2.a. Observed synoptic weather patterns*

Synoptic scale weather patterns are identified using Schüepp's synoptic weather classifications (DATA1 in Fig. 3.1) which are described in detail by Schüepp (1979), Wanner et al. (1998), and Stefanicki et al. (1998). Schüepp's weather classification system provides daily categorization of the synoptic pattern in the central Alps. Daily Schüepp classifications generated by MeteoSwiss for the Swiss Alpine area are used in this study for the historical and current timeframes (1948-1999 and 2000-2008). Schüepp's classification is a subjective method because it is based on predefined weather patterns. Many different circulation type classification (CTC) methods are available for classification of synoptic scale weather patterns. Schiemann and Frei (2010) evaluated the skill of 71 CTC systems in predicting precipitation over the Alpine area and found the Schüepp system in the top 15 out of 71 compared CTC systems for skill in prediction of precipitation occurrence. The CTCs that outperformed the Schüepp system were all automated classification schemes; whereas, Schüepp classifications are performed manually. The Schüepp classification system is used for this study because of its long data record dating back to 1948 and specific tailoring to the Alpine region. Although as noted in Schiemann and Frei (2010) MeteoSwiss is in the process of replacing manual Schüepp weather pattern classification with an automated CTC system. However, the general method described in this study for linking high resolution observations to large scale circulation from a GCM is readily adaptable to other synoptic classification systems.

The Schüepp system defines 40 synoptic weather patterns which are grouped into three main classes and eight subclasses (Wanner et al. 1998). The main three classes of the Schüepp system (convective, advective, mixed) are determined by the strength of the surface pressure gradient across a 444 km diameter centered in Switzerland at 46.5° N, 9° E. The convective type is

characterized by lack of surface pressure gradient. The advective classification is associated with the existence of a gradient in surface pressure larger than 5 hPa across the diameter. The mixed classification results when surface and 500 hPa pressure gradients are at odds (strong gradient at one level while weak at the other). The main classes are further divided into the following eight subclasses: a) convective: high (CH), flat (CF), and low (CL) (based 500 hPa geopotential height relative to the annual mean); b) advective: north (AN), south (AS), east (AE), and west (AW), based on the direction of the 500 hPa geostrophic wind; and c) mixed (MIX): no further subclassification. Schüepp's eight subclasses (CH, CF, CL, AN, AS, AE, AW, and MIX) are used in this analysis for classification of weather patterns.

### *3.2.b. Observed precipitation distribution*

Data from the MeteoSwiss operational radar network for the years 2000-2008 are the basis of the observed precipitation distribution used in this analysis (DATA3 in Fig. 3.1). The radar network includes three C-band Doppler weather radars located at Lema, Albis, and La Dole (Fig. 3.2). Each of the radars scans 20 elevations every 5 minutes monitoring radar reflectivity up to a range of 230 km. MeteoSwiss composites reflectivity from the three radars to estimate surface precipitation in a data product called RAIN. RAIN provides a 30 minute running average of surface precipitation rate (in units of mm/h) on a 2 x 2 $km^2$ Cartesian grid. Thorough descriptions of the Swiss radar network and data products are found in Joss et al. (1998), Germann and Joss (2004), Germann et al. (2006, 2009), and Panziera and Germann (2010).

For this study, a precipitation day is defined as a day having two successive occurrences at a 30 minute interval where radar-estimated precipitation rate at the surface is greater than 0.5 mm/h. The magnitude of the precipitation day threshold and the requirement for sequential 30

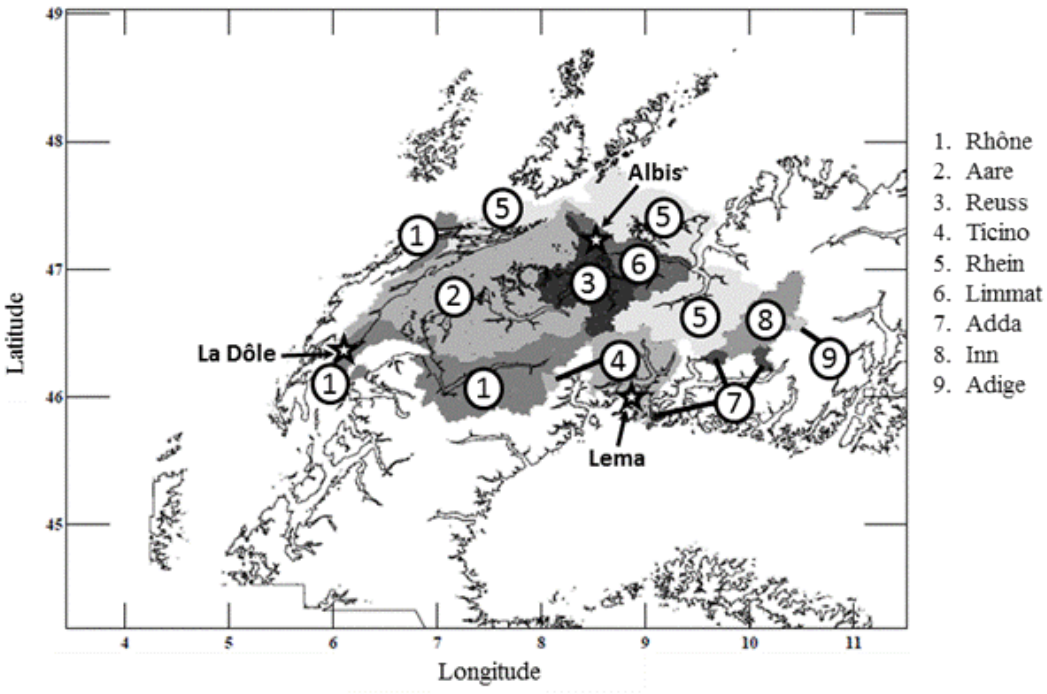


FIG. 3.2: Location of Swiss radars (stars) and river basins (numbered) relative to 800 meter above sea level topography lines. Basins are shaded gray to differentiate from topography lines.

minute measurements above the threshold differentiate it from the limit of 1 mm/day used by previous studies to segregate wet and dry days (Groisman and Knight 2008; Zolina et al. 2010). Then, the Schüepp's classification for each day of 2000-2008 is used to determine the probability of precipitation at each pixel given a certain synoptic classification, $P(\text{Precip}|\text{Class}_k)$, where *k* ranges from one to eight and represents the number of Schüepp classifications used.

$$P(\text{Precip}|\text{Class}_k) = \frac{\text{number of days of class } k \text{ with precip}}{\text{total number of days of class } k} \qquad (3.1)$$

The amount of precipitation received on a precipitation day, $\text{Precip}_d$, at a specific pixel (2 x 2 $km^2$) is calculated as:

$$\text{Precip}_d \left[\frac{\text{mm}}{\text{d}}\right] = \sum_1^{24\ \text{h/day}} \text{RR} \qquad (3.2)$$

where RR is the hourly radar estimated precipitation rate. $\text{Precip}_d$ is then associated with the daily synoptic weather classifications from 2000-2008 (CALC2 in Fig. 3.1) to obtain a

distribution of $Precip_d$ at each pixel for each synoptic classification. A mean value of $Precip_d$, is calculated for each synoptic classification at each pixel, $\overline{Precip}_{d,class\ k}$ (CALC3 in Fig. 3.1). The calculation of overall daily mean precipitation resulting from each synoptic classification, $\overline{Precip}_k$, accounts for the probability that precipitation occurs:

$$\overline{Precip}_k = P(Precip|Class_k) \bullet \overline{Precip}_{d,class\ k} \qquad (3.3)$$

The distribution of $Precip_d$ is also used to determine the observed 95$^{th}$ quantile ($Q95_{obs}$) of daily precipitation (all synoptic classes over the years 2000-2008) and the conditional probability of exceeding $Q95_{obs}$ given a specific synoptic classification, $P(Q95_{obs}|Class_k)$.

### *3.2.c. Future occurrence of synoptic weather patterns*

In this study, changes in large-scale circulation are evaluated by quantifying trends in probability of occurrence of daily synoptic patterns, $P(Class_k)$, over time. This requires identification of daily synoptic patterns for the future time period (years 2010-2099). Learning vector quantization (LVQ) is the neural network algorithm used in this analysis for identification of Schüepp's synoptic patterns in CCSM3 for a future climate scenario. The LVQ method uses supervised learning in which data with known classifications are used to classify unknown data (Kohonen 1997). In this case, daily synoptic classifications are known for the current time period (2000-2008), but unknown for the future (2010-2099).

The first step in LVQ pattern identification is to provide definition for each Schüepp's classification using known data. Within the LVQ method the definition of each pattern is known as a codebook vector. As stated in Section 3.2.a., Schüepp's synoptic classifications are based on surface pressure and 500 hPa geopotential height. For this study, daily 1000 hPa and 500 hPa geopotential height (Z1000 and Z500, respectively) data are paired with known daily Schüepp's classifications to create codebook vectors for each synoptic pattern. Specifically, Z1000 and

Z500 from daily 12Z ERAi (1.5° x 1.5° lat/lon; DATA2 in Fig. 3.1) for the years 2000-2008 are sorted based on daily Schüepp's classifications to define each Schüepp's synoptic classification in terms of Z1000 and Z500 (CALC1 in Fig. 3.1, note that this is the same time span as radar data set).

The next step in the LVQ pattern matching algorithm is classification of unknown data. In this step the objective is to obtain daily Schüepp's classification of CCSM3 data for future climate (CALC4 in Fig. 3.1). Daily Z1000 and Z500 values from CCSM3 are compared to the codebook vectors for each Schüepp's classification using a nearest-neighbor approach to determine the best classification for each day in the CCSM3 output. CCSM3 directly provides Z500; however, Z1000 is not a direct output from the model and must be calculated from equivalent sea level pressure (PSL). PSL from CCSM3 ($p_1$ in Eq. 3.4 below) is converted to Z1000 ($Z_2$) via the simplified hypsometric equation:

$$Z_2 - Z_1 = H \ln(p_1/p_2) \qquad (3.4)$$

where scale height, H = 7.5 km; $p_2$ = 1000 hPa; and surface height, $Z_1$ = 0 m.

The LVQ pattern matching algorithm requires spatial alignment between data points represented in the codebook vector and data points in the unknown data set to be classified. However, the ERAi and CCSM3 data are not initially spatially aligned. ERAi data are on a 1.5° x 1.5° latitude/longitude grid and the CCSM3 data are approximately 1.4° x 1.4°. Therefore, both sets of data are interpolated to an Equal Area Scalable Earth grid (EASE grid) with 100 km grid spacing (Brodzik and Knowles 2002). The EASE grid interpolation provides the additional benefit of distributing the data such that the density of points is equivalent at all latitudes rather than being over-weighted in northern latitudes as occurs in a standard latitude/longitude grid.

Following EASE grid interpolation, data points within ± 9° latitude/longitude of 46.5°N and 7.5°E were selected for inclusion in the pattern matching algorithm.

After determining daily synoptic classifications for 2000-2099 from the CCSM3 data, the occurrence of each classification is assessed over time (CALC5 in Fig. 3.1). The probability of occurrence of each classification, $P(Class_k)$, is calculated for each decade of 2000-2099:

$$P(Class_k) = \frac{\text{number of days of class } k}{\text{total number of days}} \qquad (3.5)$$

Time-based trends, or lack thereof, in decadal $P(Class_k)$ identified from the CCSM3 data provide indication of the effect of climate on large-scale circulation as modeled by CCSM3.

LVQ codebook generation and subsequent pattern identification in CCSM3 is a source of uncertainty in the values of $P(Class_k)$ reported for the 21st century. The uncertainty arises because the LVQ method utilizes random sampling from the data set of ERAi geopotential fields associated with each synoptic classification to optimize generation of the codebook used for classification of unknown data (Kohonen 1997). Therefore, different iterations of codebook generation result in variation in the frequency of patterns identified from CCSM3. Uncertainty associated with pattern identification has been incorporated into the results by performing 100 repetitions of the codebook generation and pattern identification process in order to report mean and standard deviation of synoptic pattern frequency as identified from CCSM3. The variation in synoptic pattern frequency reported here should not, however, be interpreted as evaluation of uncertainty inherent to CCSM3 geopotential height fields as this is not explicitly quantified in this study.

### *3.2.d. Future precipitation for Swiss river basins*

In order to obtain a precipitation distribution for specific river basins, it is necessary to spatially relate pixels in the radar estimated precipitation data to geographic boundaries of river

basins. Coordinates for vertices of polygons that form the outlines of Swiss river basins (generally > 1000 $km^2$), and the sub-catchments (approximately 30-50 $km^2$) within each basin, were provided by the Hydrology Group, Institute of Geography, University of Bern. The borders of Swiss river basins relative to 800 msl topography are shown in Fig. 3.2. To relate the basin borders to the radar-estimated precipitation rate data, the outline of each basin's sub-catchments are compared to the 2 x 2 $km^2$ grid of the radar data. Pixels in the precipitation rate data are identified as within a specific sub-catchment when greater than 50% of the area represented by a pixel is within the sub-catchment border.

Future mean precipitation ($\overline{\text{Precip}}$) at each pixel is calculated by:

$$\overline{\text{Precip}} = \sum_{\text{class}=1}^{k} \{P(\text{Class}_k) \bullet \overline{\text{Precip}}_k\} \quad (3.6)$$

Where, as previously, *k* represents the eight Schüepp's subclassifications. Future mean precipitation for an entire river basin ($\overline{\text{Basin precip}}$; CALC6 in Fig. 3.1) is calculated by summing mean precipitation over all pixels contained within the boundaries of a basin. The future probability of occurrence of each synoptic pattern, $P(\text{Class}_k)$, is the only term in Eq. 3.6 that varies; therefore, only changes in large-scale circulation (dynamic effects) affect the calculation of future precipitation. $\overline{\text{Precip}}_k$ is held constant at the value determined from the current time period (2000-2008). The assumption that $\overline{\text{Precip}}_k$ remains constant likely removes potential thermodynamic effects on precipitation such as increased atmospheric water content, changes in atmospheric moisture flux, and changes in soil moisture which all may affect the average amount of precipitation associated with a specific synoptic pattern. Appendix 1 provides a further analysis of precipitation projection based on changes in synoptic pattern frequencies on the basis of Swiss rain gauge data.

Similar to the expected precipitation calculation, the future occurrence of heavy precipitation is also based on changes in $P(Class_k)$. $P(Q95_f)$ is used to denote the future probability of exceeding $Q95_{obs}$ and is calculated as follows:

$$P(Q95_f) = \sum_{class=1}^{k} \{P(Q95_{obs}|Class_k) \bullet P(Class_k)\} \quad (3.7)$$

Again, only $P(Class_k)$ in Eq. 3.7 is changing for future decades, so changes in the occurrence of synoptic patterns over time, as identified from CCSM3, determine if any variation occurs in $P(Q95_f)$ as compared to $P(Q95_{obs})$.

## 3.3. Results and Discussion

### *3.3.a. Identification and verification of observed synoptic patterns*

ERAi Z1000 and Z500 for the eight Schüepp's synoptic patterns averaged over 2000-2008 are shown in Fig. 3.3. The geopotential height data represented in these maps were used to generate codebook vectors for identifying patterns in CCSM3 output (CALC1 in Fig. 3.1). Table 3.2 shows the frequency of occurrence and number of days that were averaged for each classification to obtain Fig. 3.3. During 2000-2008 convective synoptic patterns were most frequent, followed by advective patterns. All eight of the Schüepp's classifications were observed a significant number of times, ranging from 135 to 940 daily occurrences. The years 2000-2008 were chosen so that the synoptic pattern codebook definitions are temporally aligned with the radar data used as the basis for the precipitation distribution. As shown in Fig. 3.3 convective patterns (CH, CF, and CL) exhibit a minimal gradient in Z1000 across Switzerland; whereas, geopotential height gradients are more prominent in the advective patterns (AN, AE, AS, and AW). Additionally, the cardinal direction (north, south, east, or west) in the name of each advective pattern is generally consistent with the direction of the 500 hPa geostrophic wind,

i.e., the 500 hPa geostrophic wind for the AN classification has a northerly component. Overall, the geopotential height contours in Fig. 3.3 appear as expected based on the Schüepp subclassification definitions. Therefore, Fig. 3.3 provides qualitative verification that the ERAi geopotential height data and the daily Schüepp classifications were accurately paired to generate the LVQ codebook vectors.

| Synoptic Classification | Observed $P(Class_k)$ | # days |
|---|---|---|
| AN | 0.14 | 456 |
| AE | 0.04 | 135 |
| AS | 0.09 | 285 |
| AW | 0.08 | 265 |
| All Advective | 0.36 | 1141 |
| CL | 0.06 | 197 |
| CF | 0.30 | 940 |
| CH | 0.22 | 686 |
| All Convective | 0.57 | 1823 |
| Mix | 0.07 | 220 |
| Total | 1.00 | 3184 |

TABLE 3.2: Observed $P(Class_k)$ for each Schüepp's synoptic classification and number of days each classification occurred over 2000-2008 (from MeteoSwiss daily Schüepp's classifications). It is noted that the total number of days (3184 days) used in this analysis is less than the actual number of days between 2000-2008 (3288 days) due to omission of some days because of radar data quality or availability.

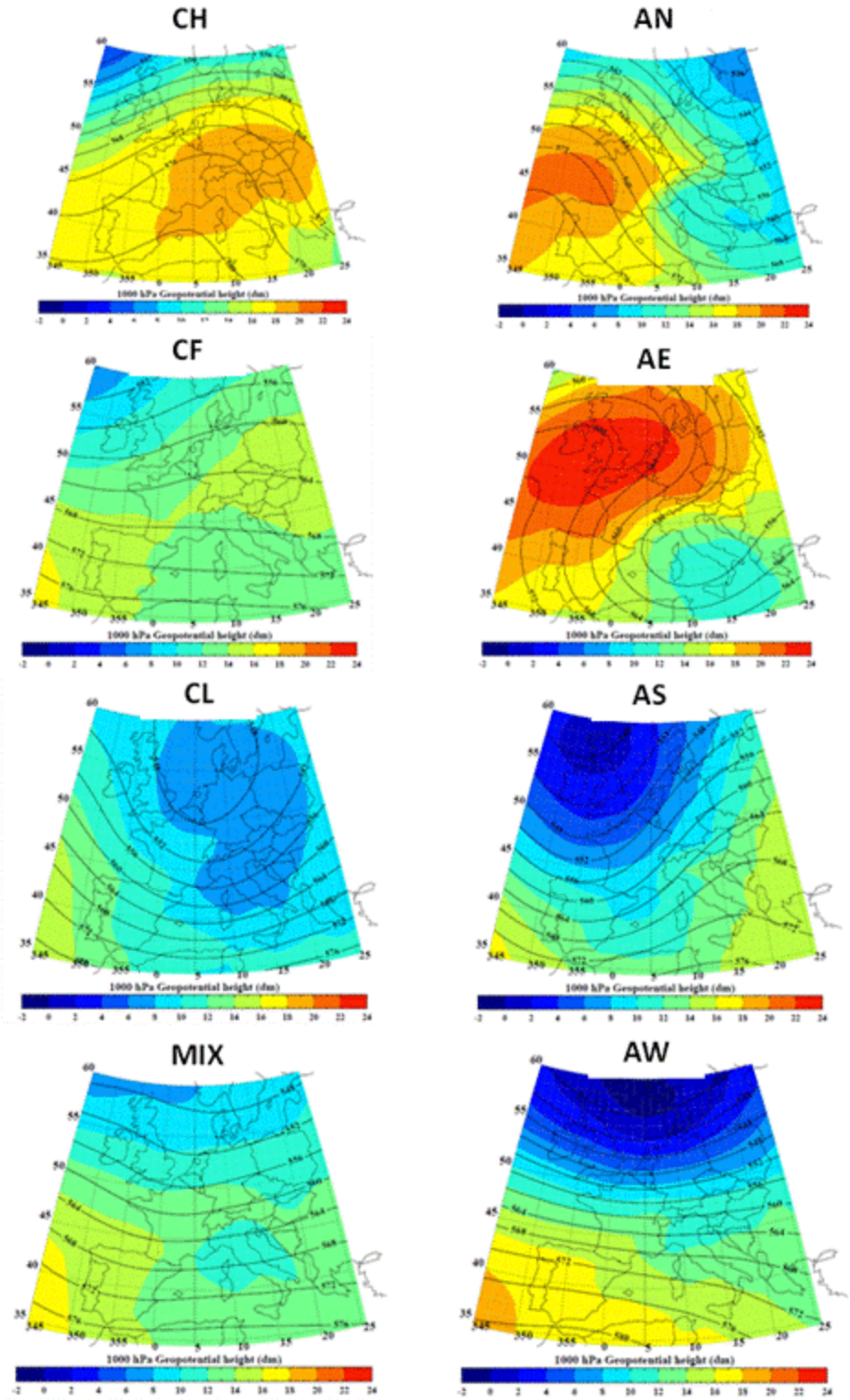


FIG. 3.3: Geopotential heights at 1000 hPa (color coded) and 500 hPa (solid black lines) averaged over 2000-2008 for the main Schüepp's weather classifications: convective high (CH), convective flat (CF), convective low (CL), mixed (MIX), advective north (AN), advective east (AE), advective south (AS), and advective west (AW). Plots are based on ERAi data set.

We base the calculation of future precipitation on the occurrence of synoptic patterns in CCSM3 data. Therefore, it is important to verify our identification of Schüepp's classifications from CCSM3. Verification is provided by comparing the occurrence of synoptic patterns as identified from CCSM3 to the observed occurrence of synoptic patterns over a known time period. The comparison establishes a bias between model and observations for the occurrence of each synoptic pattern:

$$\text{bias}_k = \frac{\text{model P}(\text{Class}_k)}{\text{observed P}(\text{Class}_k)} \qquad (3.8)$$

Model P($\text{Class}_k$) in Eq. 3.8 is the frequency that each Schüepp's classification occurs in daily CCSM3 data for the historical period 1948-1999 as identified using LVQ. Observed P($\text{Class}_k$) is the frequency that each Schüepp's synoptic pattern occurred during 1948-1999 per daily classifications provided by MeteoSwiss. The bias accounts for errors introduced during synoptic pattern identification from CCSM3 and also the ability of CCSM3 to represent the occurrence of observed historical synoptic patterns over Switzerland. The over 50 year time span used as the basis for bias calculation ensures longer-term climate cycles that impact large-scale atmospheric circulation, such as El Niño/La Niña-Southern Oscillation (ENSO) and the North Atlantic Oscillation (NAO), with periods of 6-12 years, are adequately captured in the comparison.

The biases for the eight Schüepp's classifications range from 0.20 for AE to 1.92 for AW (Table 3.3). Z1000 and Z500 from CCSM3 output for 1948-1999 show similar spatial patterns for the eight Schüepp's classifications as in Fig. 3.3 (not shown) indicating that model data are properly classified by the LVQ method. Since synoptic patterns appear to be correctly identified in the model data, the bias appears to be primarily attributed to the ability of the model to reproduce the occurrence of synoptic patterns at the frequency with which they were observed over 1948-1999. The source of the biases between modeled and observed synoptic pattern

frequencies was further investigated by using the LVQ method with the codebook developed from 2000-2008 ERAi data to identify Schüepp's classifications in 1980-1999 ERAi data. The biases for identification of synoptic patterns from the 1980-1999 ERAi ranged from 0.73 for AE to 1.11 for CH, a smaller range than for the CCSM3 data. This indicates that the LVQ-identified occurrence of synoptic patterns in ERAi is more representative of observations than the occurrence of synoptic patterns in CCSM3.

| Synoptic Classification | Observed $P(Class_k)$ | CCSM3 $P(Class_k)$ | Bias | CCSM3 $P(Class_k)$ w/bias |
|---|---|---|---|---|
| AN | 0.16 | 0.16 | 1.00 | 0.16 |
| AE | 0.05 | 0.01 | 0.20 | 0.05 |
| AS | 0.10 | 0.10 | 0.98 | 0.10 |
| AW | 0.10 | 0.20 | 1.92 | 0.10 |
| All Advective | 0.42 | 0.47 | 1.12 | 0.42 |
| CL | 0.07 | 0.06 | 0.81 | 0.07 |
| CF | 0.28 | 0.18 | 0.66 | 0.28 |
| CH | 0.17 | 0.25 | 1.49 | 0.17 |
| All Convective | 0.52 | 0.49 | 0.94 | 0.52 |
| MIX | 0.06 | 0.04 | 0.57 | 0.06 |
| Total | 1.00 | 1.00 | - | 1.00 |

TABLE 3.3: Bias between $P(Class_k)$ in observations (from MeteoSwiss daily Schüepp's classifications) and model (as identified in CCSM3 by LVQ) for Schüepp's synoptic weather classifications over the years 1948-1999.

Comparison of current (2000-2008, Table 3.2) and historical (1948-1999, Table 3.3) synoptic pattern frequencies shows the current time span has a decreased frequency of advective patterns and an increased frequency of convective patterns. The observed frequency of advective patterns (observed $P(Class_k)$ in Tables 3.2 and 3.3) decreased from 0.42 (1948-1999) to 0.36 (2000-2008) while the frequency of convective patterns increased from 0.52 (1948-1999) to 0.57 (2000-

2008). The observation that advective patterns are decreasing in frequency as convective patterns are increasing is a result similar to previously reported trends (Stefanicki et al. 1998; Rudolph et al. 2011). The decrease in advective pattern frequency is relatively uniform across the four advective subclassifications (AN, AE, AS, and AW) as the occurrence of each pattern decreased by 1-2%. However, the overall change in occurrence of convective patterns is not equally distributed among subclassifications CL, CF, and CH. Contrary to the overall increased frequency of convective patterns, the occurrence of CL declined by 1%. CF frequency increased by 2%, but the main contribution to the observed increase in frequency of convective patterns is the 5% increase in the occurrence of CH. The increased occurrence of CH indicates that anti-cyclonic patterns over Switzerland were more common during 2000-2008 than in the previous fifty years (1948-1999). The increased occurrence of CH also implies warming in the atmosphere between the surface and 500 hPa. By definition, days classified as CH have Z500 in the upper 25$^{th}$ quantile of historical Z500 values. Increased average temperature between the surface and 500 hPa would lead to a corresponding shift towards higher Z500, and therefore, more days classified as CH.

### *3.3.b. Current precipitation for each synoptic pattern*

Figure 3.4 shows mean radar-estimated daily precipitation for each synoptic classification, $\overline{\text{Precip}}_k$, received over the years 2000-2008 for seven of the nine Swiss river basins (CALC3 in Fig. 3.1). The Inn and Adige basins are not included in the analysis because topography significantly affects radar visibility and accuracy of radar-estimated precipitation for these basins. For each basin, the largest value of mean precipitation occurs during advective weather patterns having geostrophic winds, and therefore moisture flux, directed towards the Alps. For example, in the Reuss basin located on the north side and close to the main crest of the

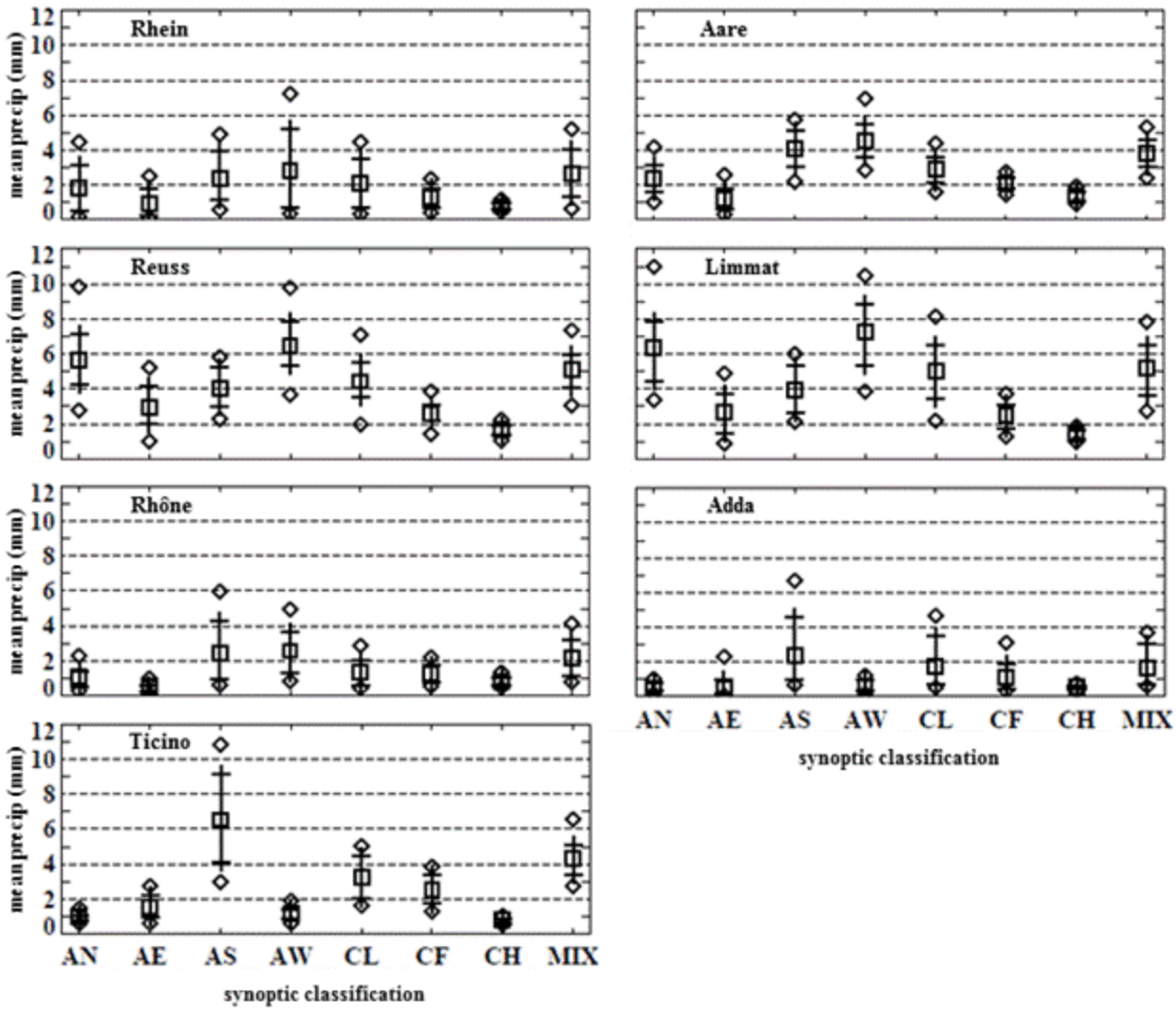


FIG. 3.4: Radar-estimated daily precipitation ($\overline{\text{Precip}_k}$) for seven Swiss river basins over 2000-2008 by Schüepp's synoptic weather classification. Boxes indicate mean values, connected bars indicate interquartile range (25$^{th}$ to 75$^{th}$ quantile), and diamonds indicate 10$^{th}$ and 90$^{th}$ quantiles.

Alps, moisture flux advected from the north and west (AW and AN classifications) results in the greatest daily mean values of precipitation (> 5 mm). The AN and AW classifications produce the largest mean values of daily precipitation for the Reuss basin because northerly and westerly winds generate orographic lift on the predominantly northwest aspects of this basin (the Schüepp system does not explicitly define an advective northwest classification). This is supported by previous work that found the AN classification results in the highest daily mean value of

precipitation, and the AW pattern results in the highest 95$^{th}$ quantile of daily precipitation for the northern Alps (Rudolph et al. 2011). Similarly, Fig. 3.4 indicates that southerly flow experienced during AS patterns produces the most precipitation in the south-facing Ticino and Adda basins. This agrees well with Sodemann and Zubler (2010) who showed that because of the orographic barrier presented by the Alpine crest the North Atlantic is the main moisture source for the Northern Alps, and the Mediterranean is the main moisture source for the Southern Alps. Also notable in Fig. 3.4 is the observation that all basins follow a similar trend for the convective patterns. Among the convective patterns, the CL pattern produces the most precipitation, followed by CF, and then CH. The CL pattern is associated with low pressure centered over Switzerland, CF has mid-tropospheric zonal flow, and CH is associated with high pressure (Fig. 3.3).

In addition to each synoptic classification resulting in different mean precipitation totals, the synoptic classifications also have varying probabilities of producing heavy precipitation (Fig. 3.5). The probability of exceeding $Q95_{obs}$ for each synoptic classification shows a similar pattern as mean daily precipitation. The basins in the northern and western Alps generally have a higher $P(Q95_{obs}|class)$ for AN and AW patterns, while the basins that are primarily south-facing have higher $P(Q95_{obs}|class)$ for the AS pattern. Exceptions to this are the Rhone, Aare, and Rhein basins that lie to the north and west of the main Alpine crest, yet have elevated $P(Q95_{obs}|class)$ for the AS pattern. In the Aare basin, the AS pattern results in the largest $P(Q95_{obs}|class)$. Therefore, although moisture advected from the west (AW pattern) results in the highest values of mean daily precipitation for the north- and west-facing Rhone, Aare, and Rhein basins, the relatively high values of $P(Q95_{obs}|class)$ for the AS pattern provide evidence of the importance of the Mediterranean as a moisture source for heavy precipitation events in these basins.

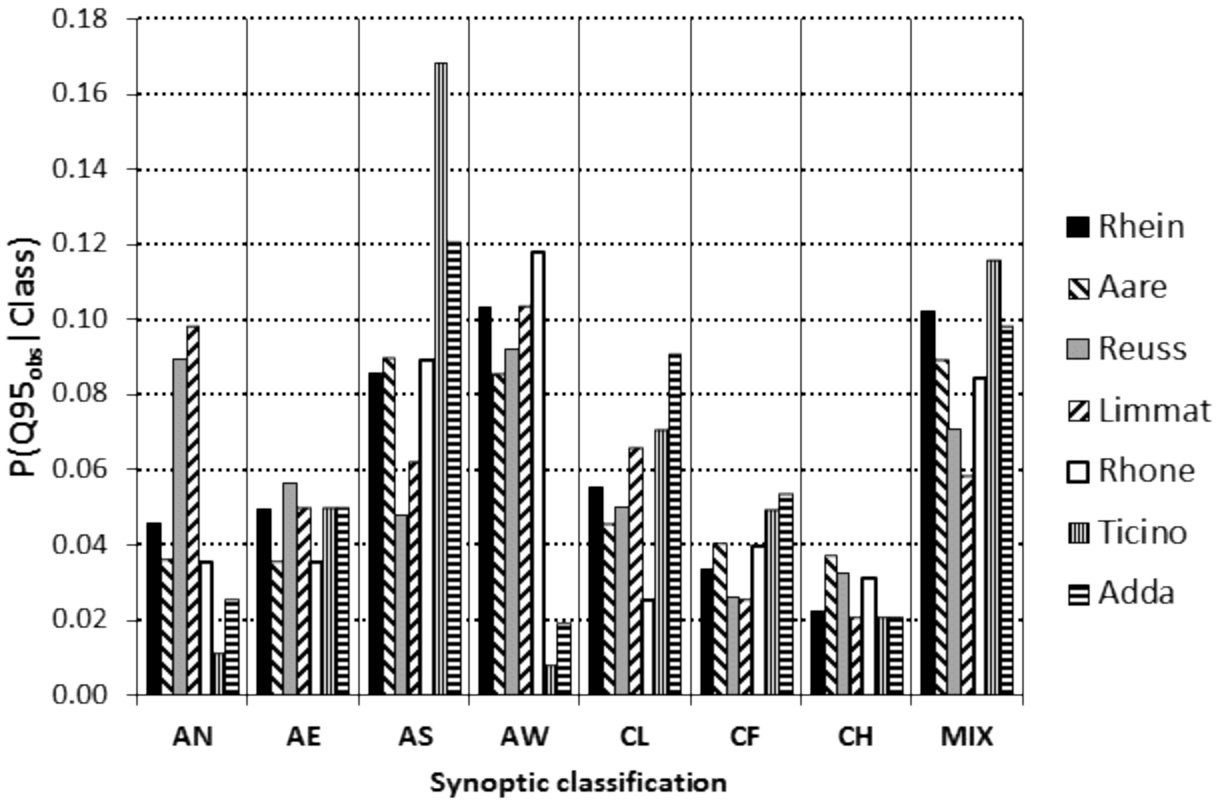


FIG. 3.5: Conditional probability of exceeding 95th quantile of daily radar-estimated precipitation in seven Swiss river basins for the years 2000-2008 given Schüepp's daily synoptic classification (classification abbreviations as in Fig. 3.3).

### *3.3.c. Future synoptic pattern frequency and precipitation*

Figure 3.6 shows mean and standard deviation for decadal frequency of Schüepp's synoptic pattern classifications, $P(Class_k)$, over the 21st century as identified from CCSM3 output. The mean and standard deviation values reported in Fig. 3.6 result from 100 replications of LVQ codebook generation and pattern identification (CALC1 and CALC4 in Fig. 3.1). The time windows used to define decades were also considered as a source of variation in the decadal synoptic pattern frequencies. Plots of annual synoptic pattern frequency (not shown) qualitatively reveal that the decadal trends identified in Fig. 3.6 are persistent, even on an annual basis, throughout the 100 year period without substantial oscillation. Therefore, it was deemed

unnecessary to perform further analysis on pattern frequency with varying decadal time boundaries.

The CCSM3 scenario A1B data show increasing frequency of convective high (CH), decreasing frequency of convective flat (CF), and slightly decreasing frequency of convective low (CL) patterns over the 21st century (Fig. 3.6 and Table 3.4). The increased occurrence of the

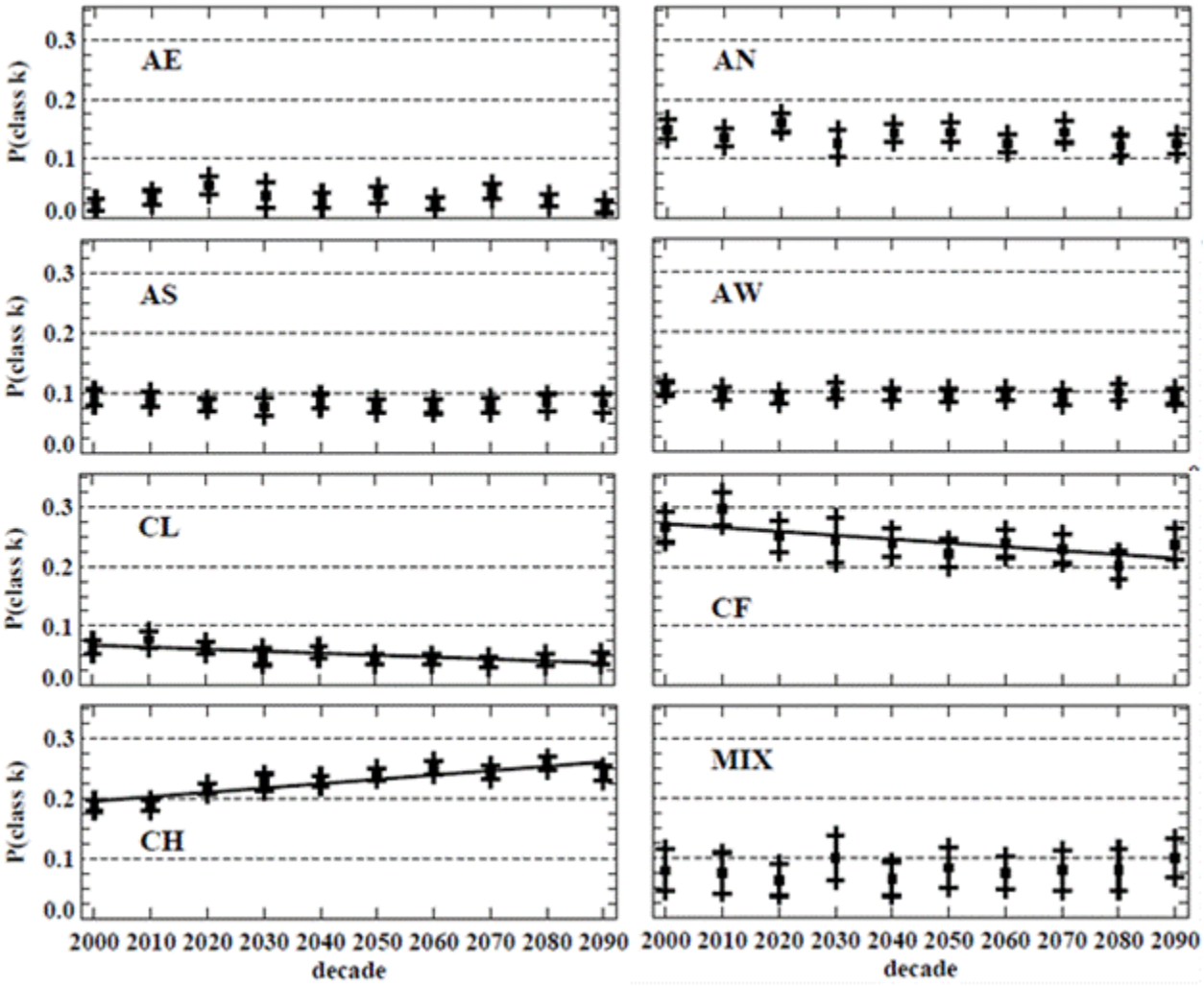


FIG. 3.6: Decadal frequency of Schüepp's synoptic pattern classifications over 21st century for A1B climate scenario as identified from CCSM3 output. Decades are labeled as 2000 for the years 2000-2009, 2010 for the years 2010-2019, etc. $P(Class_k)$ has been adjusted by the bias for each synoptic pattern that appears in Table 3.3. Mean (boxes) and 3 standard deviations (bars) result from 100 replications of LVQ codebook generation and pattern identification (CALC1 and CALC4 in Fig. 3.1). Classes where lines are present (CL, CF, and CH) have linear slopes significant at 95% confidence (as in Table 3.4).

CH pattern and decreased occurrence of the CL pattern in CCSM3 data for 2000-2099 indicate a continuation of trends in convective pattern frequencies that were identified over 1948-2008 as discussed in Section 3.3.a.. The advective pattern frequencies in CCSM3 remain relatively constant as none of the advective patterns indicate a significant trend. This differs from the observation of decreased advective pattern occurrence over 1948-2008. However, it is noted that the observed decrease in occurrence of advective patterns over 1948-2008 was relatively small (1-2%). Also, three (AN, AE, and AS) of the four advective subclassifications have negative slopes over 2000-2099 in CCSM3, although none are significant at 95% confidence (Table 3.4). Also consistent with 1948-2008 the mixed pattern shows a slight tendency towards increased frequency for 2000-2099 in CCSM3 data, but the trend is not significant at 95% confidence.

| Synoptic pattern | Slope | $R^2$ of linear fit |
|---|---|---|
| AN | - | 0.31 |
| AE | - | 0.05 |
| AS | - | 0.21 |
| AW | + | 0.25 |
| ***CL*** | **-** | ***0.70*** |
| ***CF*** | **-** | ***0.58*** |
| ***CH*** | **+** | ***0.81*** |
| MIX | + | 0.13 |

TABLE 3.4: Sign of slope and coefficient of determination ($R^2$) of linear fit to frequency vs. decade data appearing in Fig. 3.5. Bold italic font indicates patterns with slopes that are significant at 95% confidence.

The identified changes in pattern frequency combined with mean precipitation for each pattern subsequently result in a projected 10-15% decline in total precipitation for Swiss river basins by the decade 2090-2099 as compared to 2000-2009 (Fig. 3.7). In addition to basin-wide

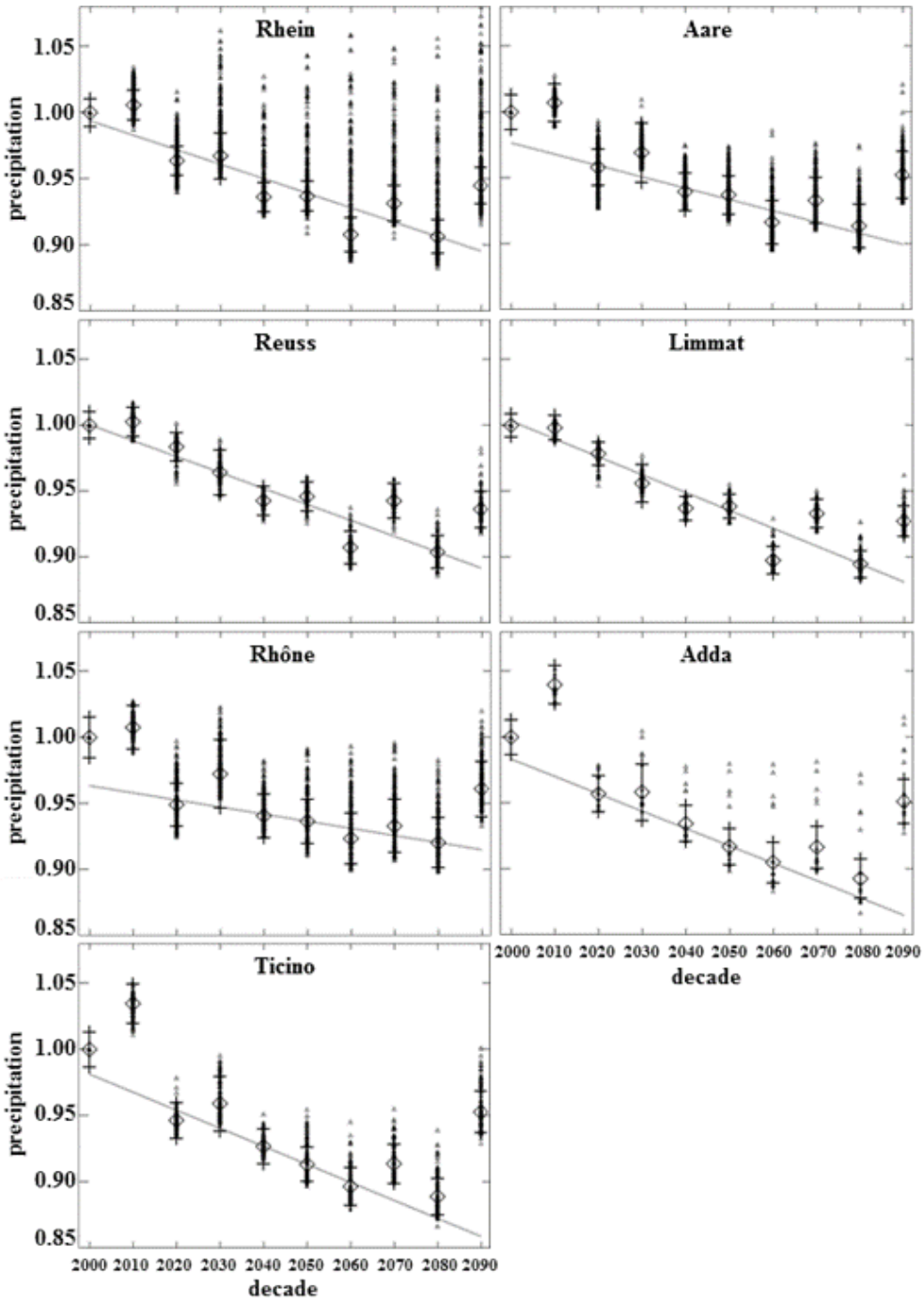


FIG. 3.7: Decadal total precipitation over the 21st century normalized to 2000-2009 for each Swiss river basin. Decades labeled as in Fig. 3.6. Individual values of normalized precipitation for each basin's sub-catchments are noted as triangles, overall basin average is noted as a diamond. Bars indicate 3 standard deviations around the basin mean. Standard deviation is calculated from the combined variance of radar estimated daily precipitation (Fig. 3.4) and synoptic pattern identification (Fig. 3.6). Kendall-Thiel linear fit is applied to the overall basin averages. In all basins the slope of the linear fit is significant with 95% confidence.

total precipitation, Fig. 3.7 also shows the range of total precipitation for each basin's sub-catchments. The high resolution nature of the radar-estimated precipitation data used as a basis for this study enables calculation of future precipitation at the sub-catchment (30-50 $km^2$) and even pixel (4 $km^2$) scale should this information be useful as an input to hydrologic models. Standard deviation of decadal precipitation for each basin (Fig. 3.7) is based on the combination of variance in radar-estimated mean daily precipitation for each synoptic pattern (Fig. 3.4) and variance due to synoptic pattern identification (Fig. 3.6). As previously stated in Section 3.2.c., the uncertainty present in CCSM3 geopotential height fields has not been quantified for this study and is, therefore, not a component of standard deviations shown in Figs. 3.7 and 3.8.

A Kendall-Thiel linear fit applied to decadal precipitation in each basin results in negative slopes for all basins that are significant with 95% confidence. A linear fit is applied only for testing significance of the trend in precipitation and is not intended to imply that precipitation is expected to decrease linearly over time. The pattern frequency changes that have the greatest impact on total precipitation are an increase in the CH pattern which produced the least precipitation in all river basins over 2000-2008 and decreases in both the CL and CF patterns. Currently (2000-2008) the CL and CF patterns both produce more precipitation than the CH pattern and some advective patterns (Fig. 3.4). The respective changes in frequency combined with mean precipitation for each classification result in a reduction in total precipitation due to dynamic changes in synoptic scale circulation. The increased frequency of the CH pattern and associated decrease in precipitation for Swiss river basins is consistent with IPCC AR4 that finds an expected decrease in precipitation in central Europe due to increased anticyclonic flow (Solomon et al. 2007). Seager et al. (2010) studied 15 GCMs used in IPCC AR4 and also found dynamic changes have a negative effect on mean zonal precipitation minus evaporation (P – E)

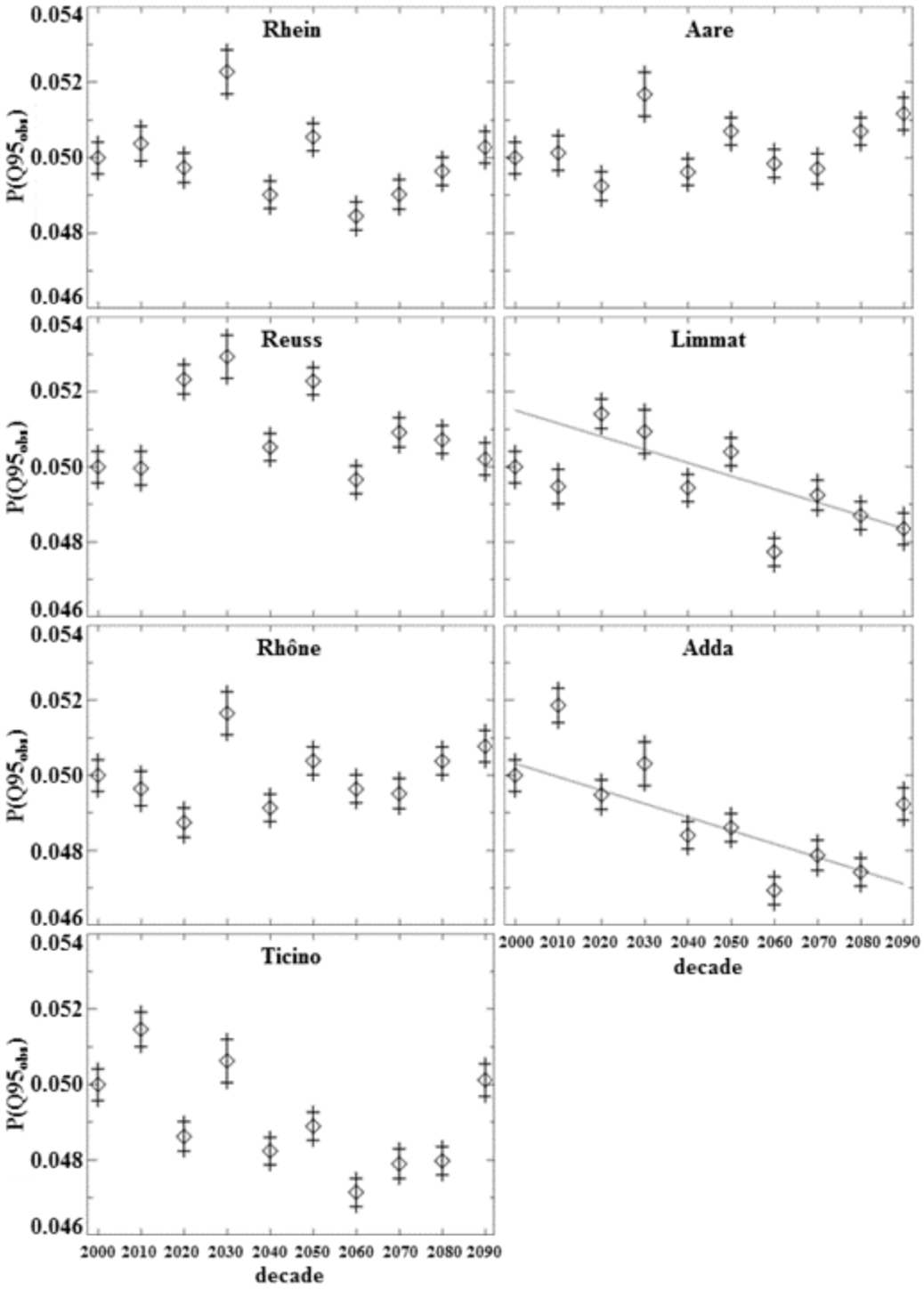


FIG. 3.8: Decadal future probability over 2000-2099 (indicated by diamonds) of exceeding the 95$^{th}$ quantile of daily precipitation established for 2000-2008 for each basin. Decades labeled as in Fig. 3.6. Connected bars indicate 3 standard deviations around $P(Q95_{obs})$ and are calculated from the variance of synoptic pattern identification (Fig. 3.6). A Kendall-Thiel linear fit is shown for basins where slope is significant at 95% confidence.

at 45°N latitude as a result of poleward movement of storm tracks due to Hadley cell expansion.

Although total precipitation decreases as a result of changes in synoptic pattern frequencies, a corresponding change in the probability of heavy precipitation is not evident (Fig. 3.8). The future probability of exceeding $Q95_{obs}$ does not appear to change significantly due to dynamic effects over the 21st century (Fig. 3.8). A Kendall-Thiel linear fit was applied to the data in Fig. 3.8, and only the Limmat and Adda basins have slopes that are significant at 95% confidence. Even for these basins, the probability of exceeding $Q95_{obs}$ only declines from 5.0% in 2000-2009 to 4.7-4.8% by the decade of 2090-2099. The absence of a dynamic effect on heavy precipitation is due to the fact that the relative differences among $P(Q95_{obs}|class)$ for the various synoptic patterns is less than the relative differences in mean precipitation resulting from each pattern. A constant probability of heavy precipitation while total precipitation is declining implies that heavy precipitation events will account for a greater overall proportion of total precipitation in the 21st century, a trend that has, in fact, already been observed in historical precipitation observations for Europe (Klein Tank and Können 2003).

The effect of changes in atmospheric moisture content on precipitation is not quantitatively addressed in this study. However, Trenberth et al. (2003) suggest that precipitation intensity may increase at the same rate as the warming-induced increase in moisture content of the atmosphere, or approximately 7% $K^{-1}$, as set by the Clausius-Clapeyron equation. Simulations from the World Climate Research Programme's (WCRP's) Coupled Model Intercomparison Project phase 3 (CMIP3) indicate that column water vapor and surface specific humidity change with global warming at rates of ~7.4% $K^{-1}$ (range 6-12% $K^{-1}$) and 5.9% $K^{-1}$ (range 5-12% $K^{-1}$), respectively (O'Gorman and Muller, 2010). Furthermore, Muller et al. (2011) find that precipitation extremes follow the rate of increase in surface water vapor concentration under

global warming. The Met Office Hadley Centre and Climatic Research Unit Global Surface Humidity dataset (HadCRUH) shows that surface specific humidity in the European Alpine area increased over 1973-2003 at a rate of 0.1-0.2 g $kg^{-1}$ $decade^{-1}$ (Willett et al., 2008). Therefore, although our analysis indicates that the probability of dynamically forced heavy precipitation events will remain constant, the precipitation rates experienced during these events may increase due to thermodynamic effects. An intensification of heavy precipitation events would effectively shift the precipitation distribution and result in increased probability of exceeding $Q95_{obs}$.

In contrast to the 10,000+ radar pixels that represent Swiss river basins in MeteoSwiss radar data, only three grid points (latitude 46.92°N and longitudes 7.03°E, 8.44°E, and 9.84°E) represent the area of Switzerland in CCSM3. CCSM3 reports large scale and convective precipitation which are summed to calculate total precipitation. Although we do not quantitatively assess uncertainty in the GCM precipitation output, Hawkins and Sutton (2011, hereafter HS11) conclude that GCM precipitation has three sources of uncertainty: 1) internal variability, or random variations in long-term climate parameters within a single model; 2) model uncertainty from variations between different models; and 3) scenario uncertainty due to uncertainty in radiative forcing. Furthermore, HS11 find the relative contributions of the three sources of variability change as the model projects further into the future. Internal variability is the largest source of uncertainty during the first 1-3 decades. Model uncertainty becomes the largest contributor to uncertainty in GCM precipitation output projections beyond 30 years. Scenario uncertainty has minimal contribution to GCM precipitation uncertainty (HS11).

No trends in total, large scale, or convective precipitation are evident in the precipitation output from CCSM3 in the general region of Swiss river basins over the 21$^{st}$ century (Fig. 3.9). Therefore, although CCSM3 shows changes in decadal frequencies of synoptic patterns,

specifically convective patterns, it does not indicate changes in total decadal precipitation. This may be attributed to thermodynamic effects counteracting dynamic effects, or it may simply be due to the fact that convective precipitation occurs at spatial scales much less than the resolution of the GCM, particularly over mountainous terrain. However, as evidenced in this study, the frequency of convective synoptic patterns influences precipitation distribution over Swiss river basins. This highlights the importance for computational models to accurately resolve convective precipitation under varying synoptic conditions in order to adequately represent future precipitation trends.

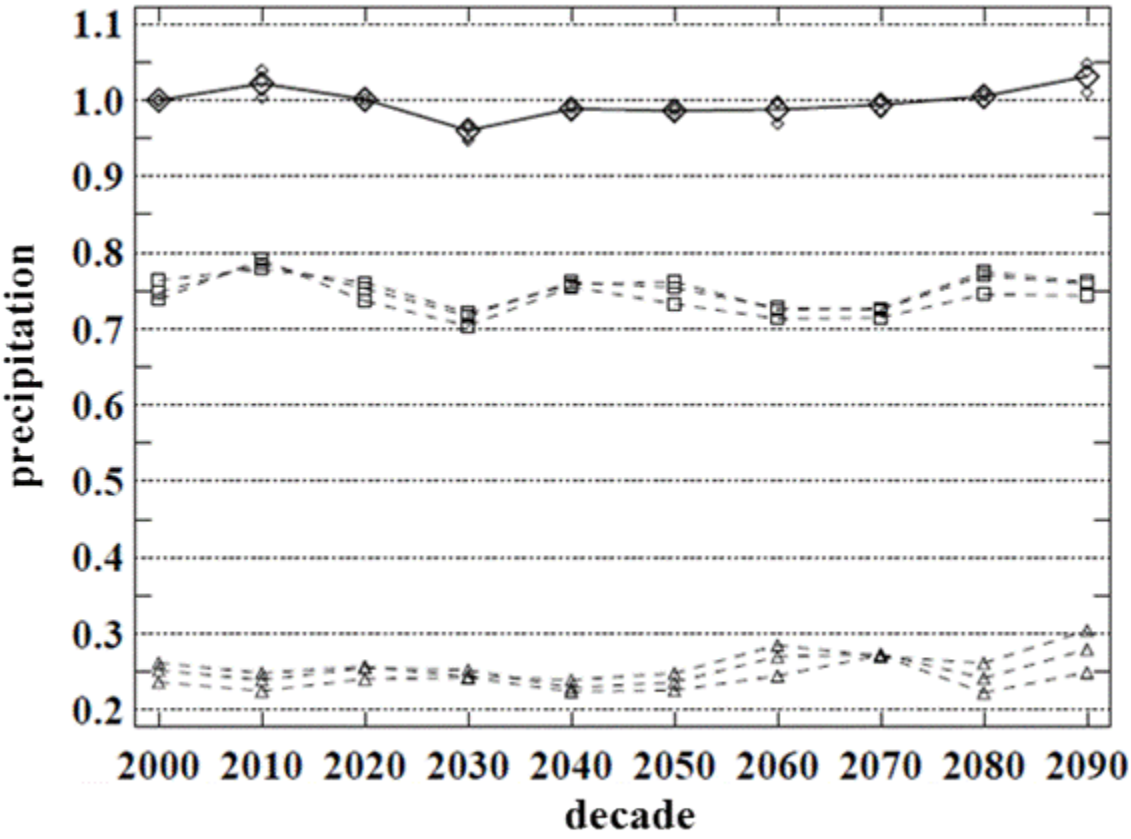


FIG. 3.9: Total decadal precipitation over Swiss Alpine area indicated by direct CCSM3 output for scenario A1B: total precipitation (large diamonds are average of three CCSM3 grid points, small diamonds are individual CCSM3 grid points), large scale precipitation (squares), convective precipitation (triangles).

### 3.4. Conclusions

This paper describes one of the first studies to combine radar-estimated precipitation observations in mountainous terrain with a GCM to describe the effects of climate change on future precipitation. Synoptic weather patterns have been used as a link between radar data and GCM output in order to determine expected trends in precipitation for Swiss river basins. This approach to understanding the impact of climate change on precipitation is unique because it provides an additional perspective to downscaled climate models for locations where sufficient radar data are available. The use of radar-estimated precipitation observations with high spatial resolution (2 x 2 $km^2$) enables development of river-basin specific analyses that account for terrain and localized climate variation, yet are not reliant on interpolation of sparse data.

Association of synoptic patterns to radar based precipitation data reveals locational-specific differences in the amount of precipitation expected for each synoptic pattern. Swiss river basins located in the northern and western Alps receive more precipitation when moisture is advected from the north or west, and moisture advected from the south increases precipitation totals for basins in southern Switzerland. Convective synoptic patterns, defined by minimal surface pressure gradient, consistently follow the same trend for expected precipitation across all basins with an anticyclonic pattern resulting in the least amount of precipitation and the cyclonic pattern producing the most precipitation. It is the difference in precipitation received from the various convective patterns that has the greatest implication for future precipitation in Swiss river basins.

Future precipitation has been quantified within this study by identifying future changes in the frequency of synoptic patterns while holding constant the amount of precipitation expected from each pattern. For IPCC climate scenario A1B the results of this study indicate that dynamic changes in atmospheric circulation over the 21st century contribute to decreases of

approximately 10-15% in total decadal precipitation for Swiss river basins. Scenarios other than A1B would likely produce varying results. The reduction in precipitation is primarily attributed to increased probability of convective high, or anticyclonic patterns, positioned over Switzerland. Since the anticyclonic pattern is observed to produce less precipitation than other synoptic patterns, an increase in its frequency results in a trend of reduced precipitation for Swiss river basins. The probability of heavy precipitation, or total daily precipitation that exceeds the 95$^{th}$ quantile established for 2000-2008, does not appear to be affected by dynamic changes over the 21$^{st}$ century. Therefore, total precipitation is expected to decrease, but heavy precipitation events account for a larger proportion of the total.

It is noted that previous work has shown thermodynamic effects on precipitation may counter-balance dynamic effects at mid-latitudes (Seager et al. 2010). Thermodynamic effects from potential changes in water content are not addressed here, so this presents an opportunity for future work. A suggested approach to quantifying thermodynamic effects is to determine the dependence of the observed precipitation distribution on specific humidity, atmospheric moisture flux, and soil moisture. These parameters, either derived from a GCM or other model, could then be used as an additional conditional variable for a long-term QPF in order to assess thermodynamic effects.

# CHAPTER 4
# SEASONALITY OF VERTICAL STRUCTURE IN RADAR-OBSERVED PRECIPITATION OVER SOUTHERN SWITZERLAND

## 4.1. Introduction

Climate aspects related to precipitation are commonly discussed in terms of spatial distribution of rainfall at the surface (i.e., amount, rate, and duration) while long-term patterns of vertical precipitation structure remain elusive. In this study we use multi-year operational radar reflectivity data from southern Switzerland to investigate the seasonal variability and annual cycle of vertical precipitation structure. Results from previous experimental campaigns are used to relate seasonal and annual reflectivity patterns to atmospheric stability and cloud microphysics observed during individual cases. Furthermore, we examine the effects of surface temperature on the vertical structure of reflectivity and implications for the impact of climate change on the hydrologic cycle.

To our knowledge, multiple-year observations of vertical precipitation structure in the European Alps have not been investigated. Most precipitation climatologies are based on surface observations from rain gauges (e.g., Schönwiese et al. 1994; Widmann and Schär 1997; Frei and Schär 1998; Schmidli et al. 2002; Klein Tank and Können 2003; Begert et al. 2005; Schmidli and Frei 2005; Moberg et al. 2006; Molnar and Burlando 2008). A few studies have used multi-year radar data as a basis for a regional precipitation climatology (Overeem et al. 2009a; Rudolph et al. 2011). However, none of these climatologies investigate long-term patterns of vertical precipitation structure. Houze et al. (2001) analyzed orographically-influenced vertical reflectivity structure in southern Switzerland over two fall seasons in 1998 and 1999. Our study is unique because we include seven years of data in our investigation of vertical reflectivity structure. In addition, we explore the relationship between total amount, duration, and intensity of precipitation that result from changes in the vertical structure. It is important to establish a

link (or lack thereof) between vertical precipitation structure and surface precipitation measurements in order to understand the implications that various storm types, as identified by the vertical structure of reflectivity, have for the hydrologic cycle.

Results from the Mesoscale Alpine Programme (MAP) characterize the vertical structure of individual storms that occurred in southern Switzerland during the fall of 1999 (Houze et al. 2001; Medina and Houze 2003; Yuter and Houze 2003; Rotunno and Houze 2007). The MAP cases provide unique information about the vertical motion and microphysics responsible for orographically-enhanced precipitation, such as whether each case has a more convective or stratiform precipitation structure. But are these individual cases from the 1999 fall season relevant to the rest of the year and representative for the typical precipitation structure in fall for southern Switzerland? Here, we apply results from the MAP case studies to explain seasonal precipitation characteristics. We infer the mesoscale conditions and microphysical processes that dominate precipitation in each season from similarities in the vertical structure of reflectivity between seasonal averages and individual MAP cases.

In this study we also investigate the relationship between temperature and seasonal changes in the precipitation structure as an indicator of potential climate change impacts on the hydrologic cycle. Warming due to anthropogenic climate change is expected to affect both the space and time distribution of precipitation through changes in precipitation intensity, duration, and interval between events (Trenberth et al. 2003). Global and regional climate models predict that changes in surface precipitation characteristics will coincide with an overall intensification of the hydrologic cycle (Solomon et al. 2007; Giorgi et al. 2011). In addition, our previous work indicates that changes in synoptic patterns over the 21st century in Europe will increase the proportion of convective precipitation for Swiss river basins (Rudolph et al. 2012). This study

further examines the possibility that precipitation events in southern Switzerland may become more convective as temperature increases and how an increase in convective precipitation may contribute to an increase in precipitation intensity.

## 4.2. Data

### *4.2.a. Monte Lema radar*

The MeteoSwiss radar network provides high-quality 3-dimensionsal multi-year reflectivity and estimated rainfall data for the Swiss Alps. The radar network is comprised of three C-band Doppler weather radars that scan 20 elevations every 5 minutes and monitor radar reflectivity up to a height of 12 km above sea level (asl) and a range of 230 km. Further detailed descriptions of MeteoSwiss radar and data products are found in Joss et al. (1998), Germann and Joss (2004), Germann et al. (2006, 2009), and Panziera and Germann (2010). *OVERVIEW* is a MeteoSwiss data product that is particularly useful for the analysis of vertical reflectivity structure. The *OVERVIEW* data set provides reflectivity at 1 km intervals between a vertical range of 1-12 km asl with a vertical resolution of 0.5 km (Joss et al. 1998). The horizontal resolution is 2 x 2 $km^2$ and the time resolution is 5 minutes. The reflectivity data are stored as 16 classes with the lowest class for reflectivity < 13 dBZ and subsequent classes in 3 dBZ intervals (e.g., 13-16 dBZ, 16-19 dBZ, 19-22 dBZ, etc.) up to the highest class for reflectivity > 55 dBZ (Joss et al. 1998). OVERVIEW data from the MeteoSwiss Monte Lema radar (Fig. 4.1) for March 2004 through February 2011 are used for this study. It is noted that MeteoSwiss is in the process of upgrading their radar network with two new radars and the addition of dual-polarization capability at new and existing radar locations (Gabella et al. 2009). As part of the upgrade project the Monte Lema radar was replaced in May 2011, which limits the data analysis to February 2011.

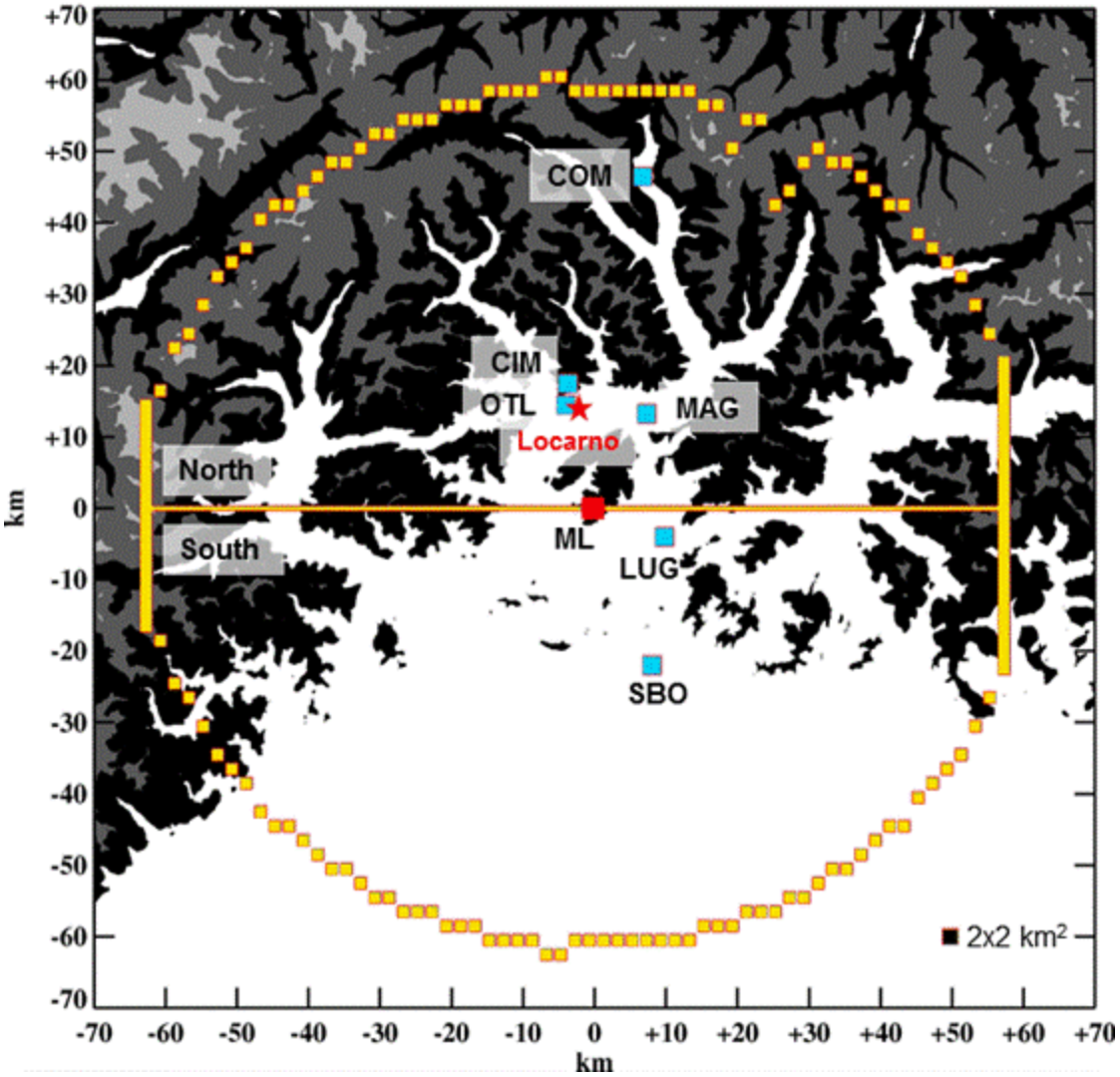


FIG. 4.1: Location of Locarno (red star), Monte Lema radar (ML, red box), and horizontal range of radar visibility used for this study (yellow boxes). The study area is divided into north and south sectors. Visibility is limited in the north sector by topography and restricted in the south sector to maintain a similar area as the north. Radar data have spatial resolution of 2x2 $km^2$ (shown for reference in lower left). Locations of rain gauge stations (blue boxes) are also indicated (abbreviations as in Table 4.1). Topography contours are in 1000 m with white denoting elevation < 1000 m asl.

The Monte Lema radar is located near Locarno, Switzerland at the southern edge of the European Alps (Fig. 4.1). Locarno provides an interesting study location since it experiences an annual climate cycle that is influenced by close proximity to the Alps and the Mediterranean Sea

(Frei and Schär 1998; Rudolph et al. 2011). An additional benefit of this location is the inclusion of data from the Monte Lema radar in Intensive Observation Periods (IOPs) and subsequent analysis resulting from the 1999 MAP experiment (Bougeault et al. 2001; Houze et al. 2001; Medina and Houze 2003; Yuter and Houze 2003; Rotunno and Houze 2007).

Because of the difference in terrain on the north and south sides of the radar, the data set used for this study was divided into north and south sectors (Fig. 4.1). The physical blockage imposed by the proximity of the Alps to the north results in a reduced range of visibility at lower elevations on the northern side of the radar. The Po River valley lies to the south of the radar, so southward visibility is largely unimpeded by the terrain (Germann et al. 2006). Since the radar's physical elevation is 1625 m, only data from ≥2 km asl are utilized. At an altitude of 2 km, the radar beam is primarily unblocked towards the north up to a range of 60 km from the radar (Fig. 4.1). Therefore, we limit the horizontal cross-sections of reflectivity at all altitudes in both the north and south sectors to a range of 60 km to maintain consistency in the volume of data analyzed at each altitude and in each sector. The radar's maximum scan elevation (40°) inhibits measurement of reflectivity directly above the radar at higher altitudes and results in a "donut hole" of missing data over the radar (Germann et al. 2006). The scan geometry causes the radius of missing data above the radar to increase with height, so it is maximized at 12 km asl. To maintain consistency in the number of pixels represented at each altitude, pixels with missing data at 12 km (representing a 6 km radius around location of radar) were omitted from lower altitudes prior to analysis.

### *4.2.b. Rain gauge network*

The selection criteria for rain gauges used in this study are: 1) the rain gauges are located at elevations below 2 km, so they are beneath the minimum altitude of analyzed radar reflectivity,

and 2) the rain gauge locations form a north-south transect across the radar range. Six rain gauge stations located within the range of selected radar data meet these criteria (Table 4.1 and Fig. 4.1). Utilizing data from multiple locations within the radar range increases the probability that localized storms captured by the radar also pass over the rain gauges. Since precipitation typically approaches the study area from the west, southwest, or south (Rudolph et al. 2011), the north-south alignment of the rain gauges also improves the likelihood of intercepting the eastward moving storms. The rain gauge data are available at 10-minute intervals with precision of 0.1 mm (https://gate.meteoswiss.ch/idaweb).

| Station | Elevation (m) |
|---|---|
| Stabio (SBO) | 353 |
| Magadino / Cadenazzo (MAG) | 203 |
| Lugano (LUG) | 273 |
| Locarno / Monti (OTL) | 366 |
| Acquarossa / Comprovasco (COM) | 575 |
| Cimetta (CIM) | 1661 |

TABLE 4.1: Rain gauge stations used in this study.

## 4.3. Method

### *4.3.a. Determining seasonal vertical structure of reflectivity*

In this study, seasonal Contoured Frequency by Altitude Diagrams (CFADs) are generated to provide a view of the average vertical reflectivity structure over the course of winter (DJF, the year associated with the winter season is the year of January/February), spring (MAM), summer (JJA), and fall (SON). CFADs provide visualization of the number of occurrences of specific radar reflectivity values at predefined altitudes over a defined time period (Yuter and Houze 1995). CFADs have previously been used to determine whether a specific storm has a more

stratiform or convective vertical structure (Yuter and Houze 1995). For the seasonal CFADs, the count of observed reflectivity for each reflectivity class *r* at each altitude *z* ($c_{r,z}$) is calculated as:

$$c_{r,z} = \sum_{1}^{N} obs_{N,r,z} \qquad (4.1)$$

where *N* is the number of 5 minute observation periods over the course of the season and $obs_{N, r, z}$ is the number of pixels with reflectivity class *r* at altitude *z* in the observed horizontal cross-section at time step *N*.

Normalizing $c_{r,z}$ by the number of pixels and time steps allows the comparison of CFAD contours between observation periods having various durations, whether it is seasons differing in number of days, or comparison of seasonal CFADs to a CFAD for an individual storm that may only last a few hours. The normalization also accounts for horizontal dimensions so that CFADs based on different spatial extents may be compared; therefore, we may directly compare CFADs for the north and south regions (Fig. 4.1) even though total surface area representing the north region is somewhat smaller than the south due to radar visibility. The normalization is carried out by dividing $c_{r,z}$ by the number of 5 minute observation periods (*N*) and also the total number of pixels (*p*) observed at each time step:

$$c_{r,z,norm} = \frac{c_{r,z}}{N\ p} \qquad (4.2)$$

CFADs plotted with normalized counts as described above allow qualitative comparison of vertical structure between seasons and/or individual storms. However, statistical comparison of CFADs requires a more quantitative method, so the centroid is calculated for each CFAD. The CFAD centroid is essentially the center of mass of the CFAD plot and provides a quantitative measure suitable for statistical analysis. The centroid of the CFAD has x- and y-coordinates (x-centroid and y-centroid) with *x* corresponding to reflectivity and *y* corresponding to height or altitude.

*4.3.b. Individual storm identification and classification of vertical structure*

In addition to exploring vertical reflectivity structure on a seasonal basis, CFADs and CFAD centroids are also generated for individual storms (following Eqns. 4.1 and 4.2; Sec. 4.3.a.). Individual precipitation events are identified using rain gauge data from the six stations listed in Table 1. Several previous analyses have identified precipitation events using a threshold of 1 mm rainfall ($R$) received over a 24 h period (Groisman and Knight 2008; Zolina et al. 2010; Giorgi et al. 2011). A similar approach is taken for this study. The start time of each event is the first 10-minute period when $R \geq 0.1$ mm is recorded at any single station and at least 1 mm precipitation is received in 24 h or less. The end time for an individual precipitation event is the last 10-minute period when $R \geq 0.1$ mm is recorded and no precipitation is measured over the next three consecutive hours at any of the six stations. The 3-hour interval without precipitation used to indicate the separation between storms is consistent with the spectral analysis of continental European storm frequency reported in Fraedrich and Larnder (1993) and the threshold used in Molnar and Burlando (2008; Peter Molnar, personal communication). Using the precipitation gauge-based storm criteria we identified 559 precipitation events between March 2004 and February 2011. Rain gauge data from all six stations are used to derive storm duration and interval between storms. Total precipitation amount and maximum 10 minute precipitation rate are from the Locarno station. The average precipitation rate for each storm is calculated using the total amount of precipitation received at Locarno and the storm duration.

After identifying individual storms, a CFAD and associated CFAD centroid coordinates are generated for each precipitation event. As with the seasonal CFADs and CFAD centroids described above (Sec. 4.3.a.), the storm-specific CFADs are also normalized following Eq. 4.2, so that the storm- and seasonal-based CFADs and centroids may be directly compared. In

addition, we use the centroids from the individual storm CFADs to classify the vertical structure of reflectivity for each precipitation event as winter-type (DJF), summer-type (JJA), or spring/fall type (MAM/SON) by finding its nearest neighbor among the seasonal CFAD centroids. Seasonal CFAD centroids from the northern sector were used for classification of individual storms since most of the rain gauge stations are located north of the radar.

## 4.4. Results

### *4.4.a. Seasonal variation of vertical structure*

CFADs for each season from March 2004 through February 2011 show distinct seasonal differences that are consistent from year-to-year in both the north and south sectors (Fig. 4.2). For this study, we define vertical extent of reflectivity as the maximum altitude where the 0.004 count contour (equivalent to a spatial frequency of 0.3 $km^{-2}$ $day^{-1}$) appears in the seasonal CFAD (Fig. 4.2). Vertical extent of reflectivity is maximized in summer (JJA) when reflectivity extends to 9-10 km asl and minimized in winter (DJF) when reflectivity extends only to 5-6 km asl both in the north and south sectors. Therefore, reflectivity of 15 dBZ is observed with the same frequency at nearly twice the altitude in summer as in winter and indicates that precipitating systems in summer extend higher into the atmosphere. Seasonal CFADs for spring (MAM) and fall (SON) have intermediate values of vertical extent of 6-7 km which is 3-4 km lower than JJA and slightly higher (~1 km) than DJF.

The seasonal CFADs also show differences in magnitude of reflectivity (Fig. 4.2). Larger magnitude of reflectivity is more frequent near the ground in JJA than in DJF. In the north sector at 3 km asl, reflectivity of 35 dBZ occurs in JJA with similar frequency as 27 dBZ in DJF. Maximum reflectivity in MAM and SON (33-34 dBZ at 2 km in north region) approaches the magnitude of maximum reflectivity seen in JJA (35 dBZ at 3 km in north region, Fig. 4.2). A

distinct difference between MAM and SON versus JJA for both the north and south is that larger reflectivity values appear at 3 km asl in JJA and at a lower altitude of 2 km in MAM and SON.

Although the seasonal CFADs from the north and south sectors are similar in vertical extent and magnitude of reflectivity, the frequency of observed reflectivity is larger on the north side of the radar (Fig. 4.2). For example, comparison of the north and south JJA seasonal CFADs shows that 20 dBZ reflectivity is approximately 50% more frequent at 3 km asl in the north sector than in the south (0.012 count contour for north versus 0.008 count contour for south; JJA in Fig. 4.2). Higher frequency of observed reflectivity at each altitude on the north side of the radar is consistent throughout the seasonal CFADs.

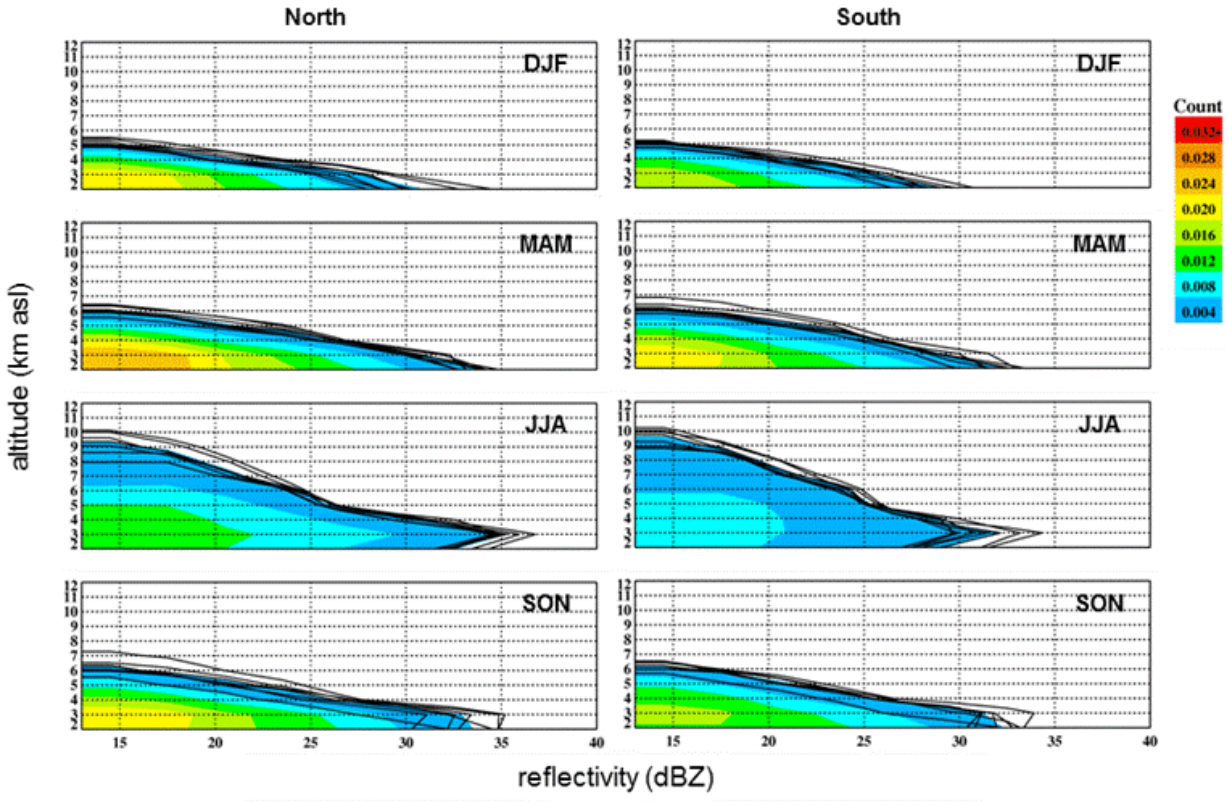


FIG. 4.2: Seasonal CFADs for the north (left column) and south (right column) sectors for March 2004 through February 2011 (DJF – winter; MAM – spring; JJA – summer; SON – fall). Color contours represent average seasonal CFAD over all years. Black lines are the 0.004-count contour for each individual year.

Seasonal CFAD centroid locations for the north sector (as described in Section 4.3.a. and based on Fig. 4.2) for each year of 2004 through 2010 (2005 through 2011 for DJF) are shown in Fig. 4.3 (bold diamond symbols). From this point on, our results and discussion of seasonal CFAD centroids are solely focused on the north sector because the seasonal CFAD centroids for the north and south sectors are similar (not shown), and the majority of rain gauges that we use for storm identification are located north of the radar (Fig. 4.1). Enhanced reflectivity values observed at higher elevations in JJA are reflected in the greatest magnitude y-centroid (range of 4.1 to 4.7 km asl) as determined from the CFAD (y-axis corresponds to altitude, Fig. 4.3). The

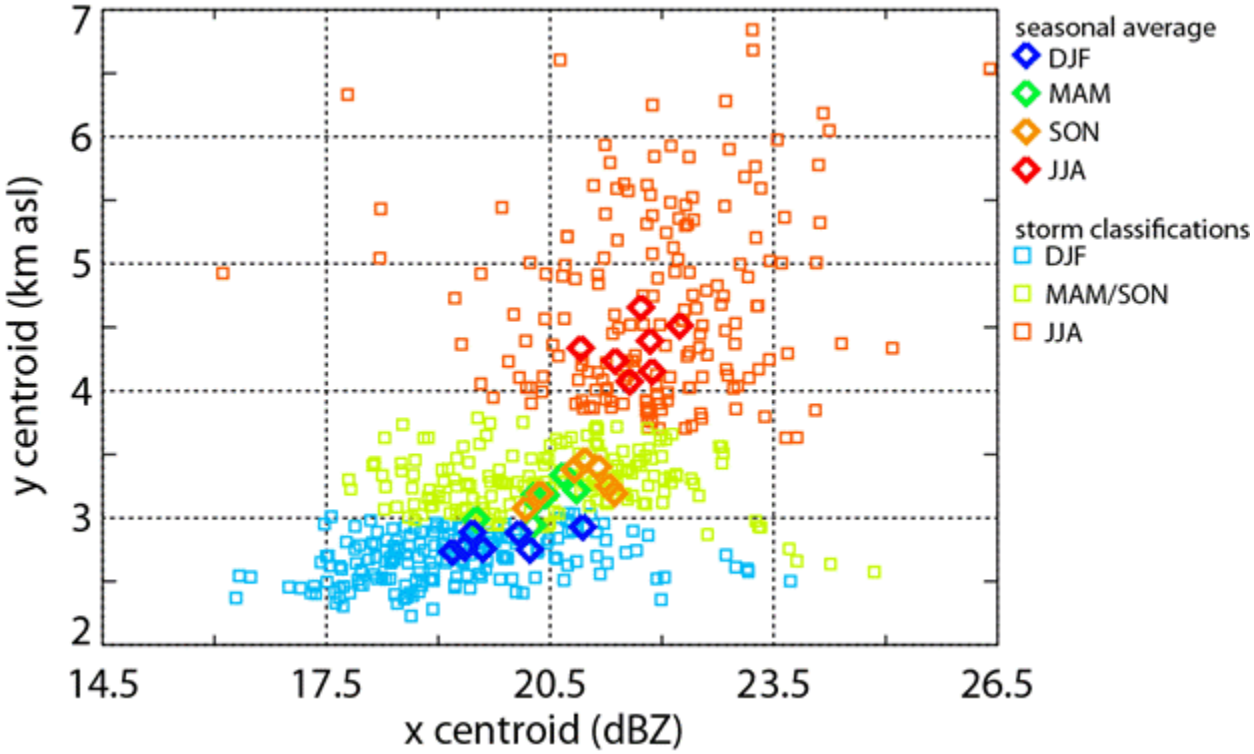


FIG. 4.3: Centroids as determined from the north sector seasonal CFADs shown in Fig. 2 (bold diamond symbols) and individual storm CFAD centroids (square symbols) with x-centroids representing reflectivity and y-centroids representing altitude. Colors represent different seasons with winter (DJF) in blue, spring (MAM) in green, summer (JJA) in red, and fall (SON) in orange. Individual storms are classified by nearest neighbor among the seasonal CFAD centroids. Fall- and spring-type storms (MAM/SON: indicated in light green) are combined into a single class for the individual storm analysis because no significant difference is observed between the seasonal spring and fall x- (reflectivity) and y- (altitude) centroids.

JJA seasons' CFAD y-centroids are significantly greater (with 95% confidence) than winter, spring, or fall. DJF has the lowest CFAD y-centroids (95% confidence) ranging from 2.7 to 2.9 km. CFAD y-centroids for MAM and SON are not found to significantly differ (ranging from 2.9 – 3.4 km). JJA also experiences larger reflectivity values than the other seasons (with 95% confidence, CFAD x-axis corresponds to reflectivity in Fig. 4.3). This results in JJA having the largest CFAD x-centroids (ranging from 21 to 23 dBZ). The x-centroids (x-axis corresponds to reflectivity) for DJF and MAM/SON vary between 18-21 dBZ and 19 to 22 dBZ, respectively. The intermediate values of the CFAD x- and y-centroids for MAM and SON as compared to JJA and DJF imply that radar-observed reflectivity structure undergoes a transition from DJF to JJA, and vice versa.

### *4.4.b. Classification of individual storms reveals annual pattern of vertical structure*

The significant differences in the seasonal CFAD centroid locations (Fig. 4.3, bold diamond symbols) enables us to classify individual storms as winter- (DJF), summer- (JJA), or spring/fall- (MAM/SON) type systems based on the comparison of individual storm CFAD centroids to seasonal CFAD centroids. Individual storms are classified by identifying the nearest neighbor among the seasonal CFAD centroids (Fig. 4.3), so the individual storm classifications (Fig. 4.3, square symbols; Sec. 4.3.b.) are independent of the season in which the storm occurred. MAM- and SON-type storms are grouped together as classification MAM/SON because their respective seasonal CFAD centroids are indistinguishable (not significantly different at 95% confidence). The seasonal and individual storm CFAD centroids in Fig. 4.3 also indicate that mean reflectivity increases (x-centroid) with vertical extent (y-centroid).

Figure 4.4 shows the time series of all individual precipitation events occurring between March 2004 – February 2011 and their corresponding storm classifications based on the storms' vertical structure of reflectivity (square symbols in Fig. 4.3). An annual pattern is apparent with individual storm classifications following a progression from DJF- to MAM/SON- to JJA- to MAM/SON- to DJF-type storms as time moves forward through each year. The vertical structure of DJF-type storms (i.e., storms with vertical extent < 5-6 km and reflectivity mainly < 20-30 dBZ) is most common during winter, but also occurs in spring and fall and only occasionally in summer (Fig. 4.4). Vertical structure of reflectivity typical for MAM/SON-type storms is mainly observed during spring and fall. Although MAM/SON-type storms appear in all seasons, they are less common in winter. JJA-type storms (i.e., storms with vertical extent < 9-10 km and high reflectivities of < 30-35 dBZ) exist mainly during summer, but also appear in late spring and early fall.

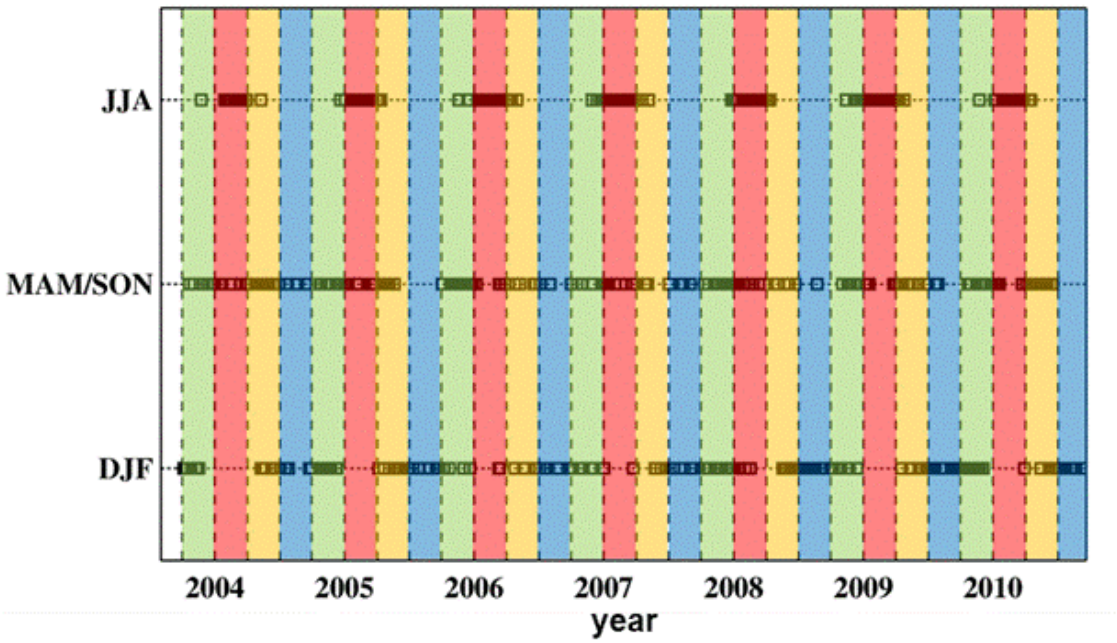


FIG. 4.4: Individual precipitation events (squares) occurring between March 2004 and February 2011 are plotted in time series by their classification based on the storms' vertical structure of reflectivity (Fig. 4.3). Colored bands indicate seasonal time windows for spring - MAM (green), summer - JJA (red), fall - SON (yellow), and winter - DJF (blue) with dashed vertical lines separating seasons.

### *4.4.c. Relationship between vertical structure of reflectivity and surface temperature*

Throughout spring a steady increase in average daily temperature is experienced with decreasing average daily temperature as fall progresses (solid lines in Fig. 4.5). The vertical structure of JJA-type storms becomes more common in late spring when average daily temperature is higher (Fig. 4.5a); likewise, the vertical structure associated with JJA-type storms becomes less frequent as average daily temperature decreases during fall (Fig. 4.5b). Therefore, as daily average temperature increases in spring, the frequency reflectivity observed at higher altitudes also increases. Similarly, individual storms that occur in early spring and late fall commonly have a vertical structure of DJF-type storms. MAM/SON-type vertical structure is more frequently observed during the middle of spring and fall as the reflectivity structure transitions from DJF- to JJA-type storms in spring and JJA- to DJF-type storms in fall. Based on the 2004-2010 data, there is no indication that the occurrence of JJA- or DJF-type storms has consistently shifted to an earlier or later onset or decline in spring or fall.

To further explore potential effects of temperature on the vertical reflectivity structure, CFADs for individual storms and surface temperature from Locarno are combined to determine the conditional probability of experiencing a particular storm-type classification given the three-day average daily temperature (Fig. 4.6). Average three-day temperature is used as the basis for conditional probability in order to align average surface temperature with the observed frequency of continental European frontal systems which occur, on average, approximately every three days (Fraedrich and Larnder 1993). In Fig. 4.6, the relationship between storm type and surface temperature, as evidenced by conditional probability, is based on all storms occurring between March 2004 and February 2011. The smooth curves (black lines) in Fig. 4.6 are the result of

a) spring

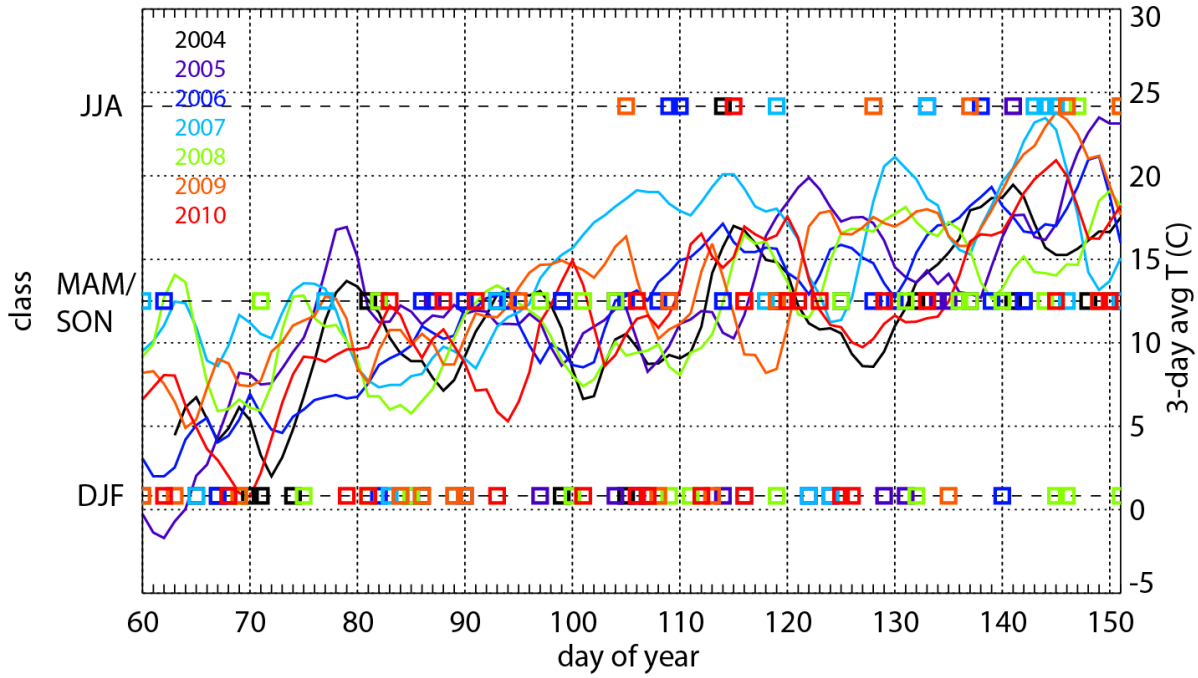


b) fall

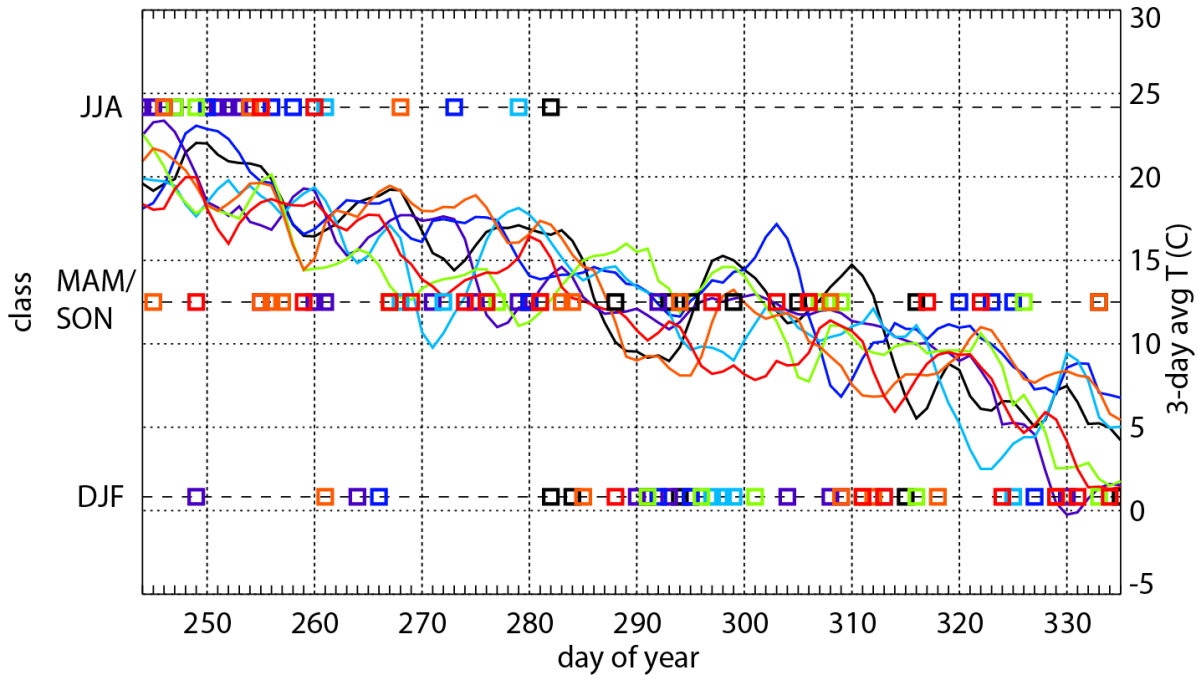


FIG. 4.5: Occurrence of individual precipitation events (square symbols) for a) spring and b) fall of the years 2004-2010 as a function of storm type based on Fig. 4.2. Solid lines indicate three-day average temperature at Locarno for each year. Colors indicate individual years.

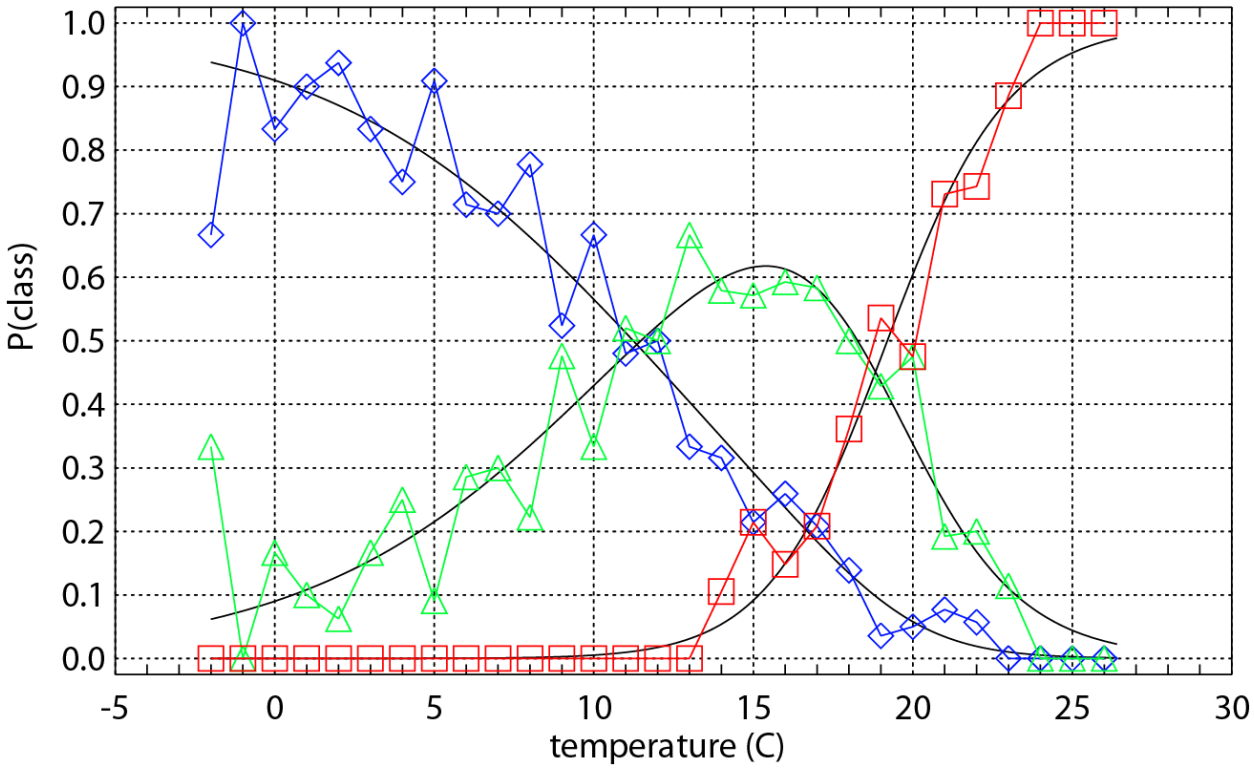


FIG. 4.6: Probability of each storm-type class as a function of the three-day average daily temperature for all observed precipitation systems occurring between March 2004 and February 2011: blue diamonds – DJF; green triangles – MAM/SON; red squares – JJA. Black lines are the vglm fit of conditional probabilities as described in Section 4.4.c.

fitting a vector general linearized model (referred to as vglm hereafter) to the observed data following Yee and Hastie (2003) and Yee (2008). The vglm fit results in coefficients $a_n$ and $b_n$ for the log-linear relationships:

$$\log\left(\frac{P_{MAM/SON}}{P_{DJF}}\right) = a_1 + b_1 T \qquad (4.3)$$

$$\log\left(\frac{P_{JJA}}{P_{DJF}}\right) = a_2 + b_2 T \qquad (4.4)$$

where $P_{DJF} + P_{MAM/SON} + P_{JJA} = 1$. $P_{DJF}$, $P_{MAM/SON}$, and $P_{JJA}$ are the respective probabilities for classes DJF, MAM/SON, and JJA when the 3-day average temperature is $T$. Applying the vglm fit to the 2004-2011 data, the log-linear relationship results in the following coefficients: $a_1 = -2.31$; $b_1 = 0.20$; $a_2 = -11.68$; $b_2 = 0.70$.

DJF-type vertical structure is the most probable storm classification when average daily temperature is less than 11°C (Fig. 4.6). MAM/SON becomes the most common storm type when the surface temperature ranges between 11-18°C. Above 18°C JJA-type vertical structure is the most likely classification, and only JJA-type vertical structure is observed when temperature exceeds 24°C. DJF-type vertical structure is not observed when daily average surface temperature rises above 23°C, and JJA-type storms are not observed below 14°C.

### *4.4.d. Surface precipitation characteristics associated with vertical structure of reflectivity*

Beyond changes in vertical structure of radar reflectivity, the transition in storm type has additional implications for surface precipitation characteristics. Table 4.2 lists the mean values of total precipitation, storm duration, interval between storms, average precipitation rate over the entire storm, and maximum precipitation rate within 10 minutes for each storm-type classification regardless of the season in which the individual storms occurred. The entire range of data is shown in Fig. 4.7. JJA-type storms have the shortest duration (mean duration 16.7 h) as compared to MAM/SON- and DJF-types, each having a mean duration of 24.2 h (Table 4.2 and Fig. 4.7a). The precipitation characteristics of each storm type shown in Fig. 4.2 are compared by using a Wilcoxon non-parametric test at 95% confidence. No significant difference is found in the mean length of the dry intervals following JJA- and MAM/SON-type storms (~60 h, Table 4.2 and Fig 4.7b). The dry interval of 95 h following DJF-type storms is the longest. Despite the difference in duration, the Wilcoxon non-parametric comparison finds no significant difference in total precipitation for JJA- and DJF-type precipitation events (Table 4.2 and Fig 4.7c). The only type that produces significantly different total precipitation is MAM/SON (mean total of 27.2 mm) which is greater than both DJF and JJA (14.9 and 21.8 mm, respectively; Table

4.2 and Fig 4.7c). Since no statistical difference is found in total amount of precipitation received from JJA- or DJF-type storms, but JJA-type storms have shorter duration, it follows that the average precipitation rate recorded during JJA-type storms (1.4 mm $h^{-1}$) is more than three times greater than for DJF (0.4 mm $h^{-1}$, Table 2). In addition, JJA-type storms produce the largest maximum 10-minute precipitation rate (3.5 mm/10 min), nearly double the maximum 10-minute precipitation rate of MAM/SON-type storms (1.4 mm/10 min) and seven times greater than DJF-type vertical structure (0.5 mm/10 min; Table 4.2 and Fig. 4.7d).

| Mean precipitation characteristics | *Classification* DJF | MAM/SON | JJA |
|---|---|---|---|
| Total (mm) | 14.9 [A] | 27.2 [B] | 21.8 [A] |
| Duration (h) | 24.2 [A] | 24.2 [A] | 16.7 [B] |
| Interval (h) | 95.3 [A] | 60.1 [B] | 56.4 [B] |
| Average rate (mm/h) | 0.4 [A] | 0.8 [B] | 1.4 [C] |
| Maximum rate (mm/10 min) | 0.5 [A] | 1.4 [B] | 3.5 [B] |

TABLE 4.2: Mean precipitation characteristics for each storm-type classification. Letters [in brackets] indicate statistically significant groupings by Wilcoxon non-parametric comparison at 95% confidence. For instance, the total precipitation for DJF and JJA is not statistically different (both DJF and JJA denoted by [A]), but both DJF and JJA differ from MAM/SON (MAM/SON denoted by [B]). Average rate is statistically different for each classification (as denoted by [A] for DJF, [B] for MAM/SON, and [C] for JJA). The full range of data for each classification is shown in Fig. 4.7.

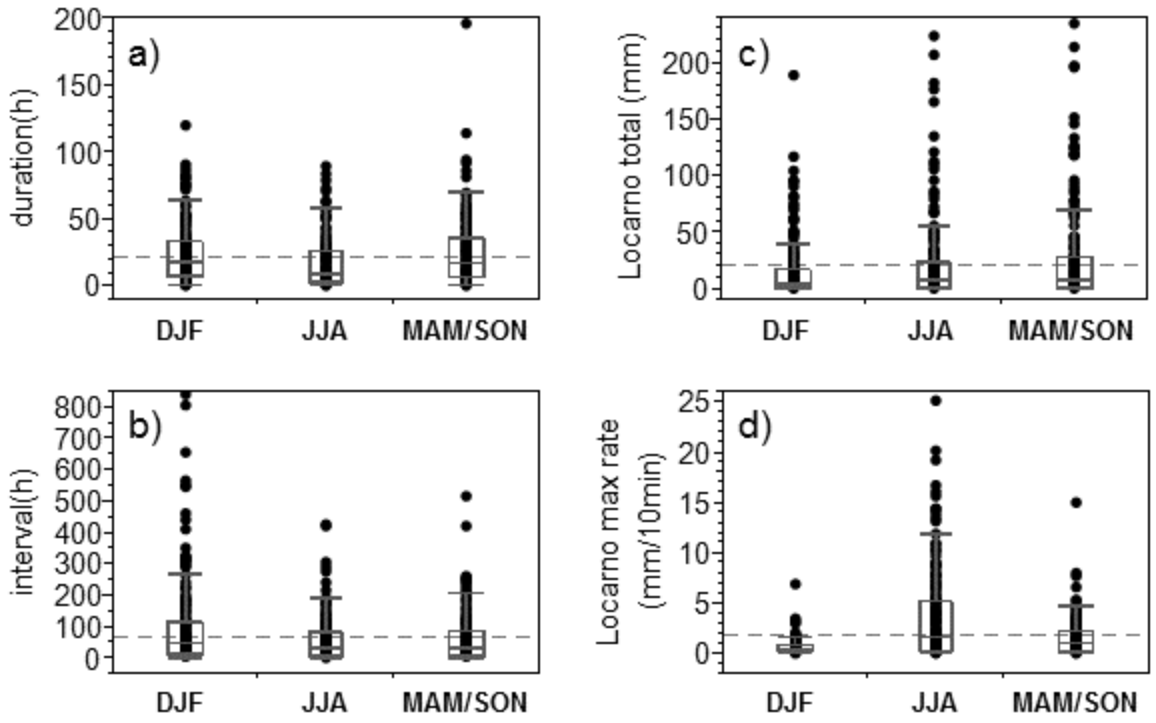


FIG. 4.7: Precipitation characteristics of each storm-type based on rain gauge data: a) storm duration, b) interval between storms, c) total precipitation amount, and d) maximum 10-minute precipitation rate. Boxes indicate median and interquartile range ($25^{th}$ to $75^{th}$ quantile) with extended hash marks at the 10% and 90% quantiles.

### *4.4.e. Potential effect of increased surface temperature on surface precipitation characteristics*

The vglm for the probability of each storm type as a function of temperature (Eqns. 4.3 and 4.4; Fig. 4.6) is used to further quantify the potential effect of an increase in surface temperature due to climate change on precipitation characteristics by using Monte Carlo simulations (see Appendix 2). It is a simplified model of precipitation as it is only based on surface temperature without accounting for potential changes in moisture, atmospheric stability, or large-scale circulation which might alter in a changing climate. Nonetheless, the intent of the Monte Carlo simulations is to show the impact of increased convective precipitation type on seasonal precipitation characteristics. Figure 4.8 shows average storm duration, interval between storms,

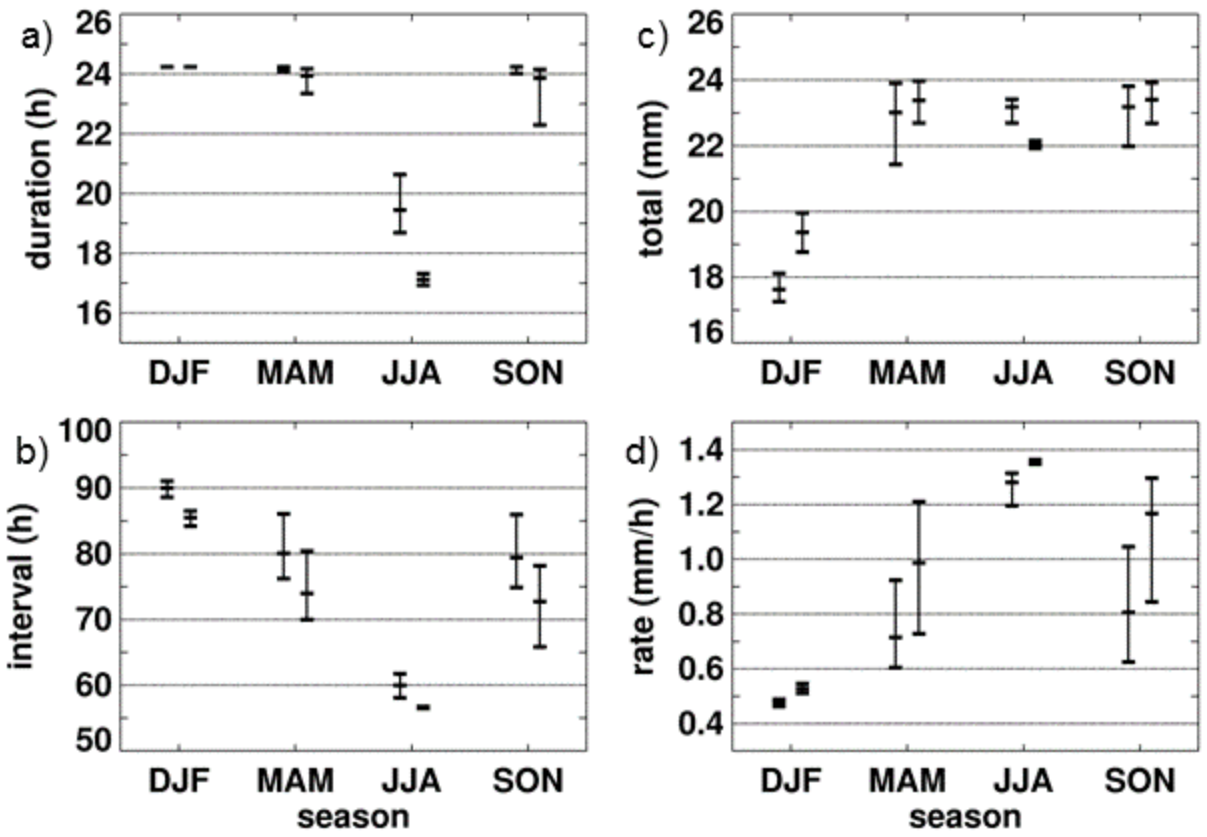


FIG. 4.8: Results from the Monte Carlo simulation of precipitation characteristics by season for current and future climate: a) storm duration, b) interval between storms, c) total precipitation amount, and d) average precipitation rate. For each season, left side data are for current climate and right side data represent the future climate simulations. Hash marks indicate median and interquartile range ($25^{th}$ to $75^{th}$ quantile).

total amount of precipitation received during each storm, and average precipitation rate for each season from the simulations of current and future climate. Storm duration in winter is the same in both the current and future simulations with a tight range in the data (Fig. 4.8a). This is due to winter season storms remaining a mixture of DJF- and MAM/SON-type storms with both having the same mean duration (Table 2). Therefore, although the vertical structure of the MAM/SON-type storms becomes more probable in winter with increased temperature, it has no effect on the storm duration. For the storm duration in spring and fall, the interquartile range ($25^{th}$ to $75^{th}$ quantile, referred to as IQR hereafter) increases, and the median shifts towards shorter duration

events as JJA-type storms become more common in the future. In summer, storm duration for the future simulation approaches the observed mean value of duration (Table 2) for JJA-type storms. Also, the IQR for summer duration is reduced in the future as MAM/SON-type storms are less probable with increased temperature, and vertical structure of JJA-type storms dominates.

The Monte Carlo simulation results show that the interval between storms is reduced in all seasons for the future climate simulations (Fig 4.8b). The reduction of interval between storms is mainly due to reduced probability of DJF-type vertical structure when surface temperature is increased. Storms with DJF-type vertical structure have the longest interval between subsequent precipitation events (95.3 h in Table 2), so a reduction in their frequency as shown in the future simulation decreases the average interval between storms.

The largest effect and only significant increase in total precipitation is seen in winter (increase of 2 mm per storm, or approximately 12%; Fig. 4.8c). For our simulation this is due to increased frequency of MAM/SON-type vertical structure which produces greater total precipitation than the DJF-type storms. Total precipitation in spring and fall does not change significantly, but does indicate a future reduction in IQR because decreased occurrence of DJF-type vertical structure, having the lowest mean total precipitation, drives a reduction in variation. Mean total precipitation received from each storm is slightly reduced in the future for summer (reduction of 1 mm per storm, or approximately -4%). Similar to the storm duration, summer season total precipitation moves toward the mean value for JJA-type storms as MAM/SON-type storms that produce greater total precipitation occur less often.

Average precipitation rate increases in all seasons for the future climate Monte Carlo simulations (Fig. 4.8d). Average precipitation rate is a function of storm duration and total

precipitation received. Therefore, the winter precipitation rate increase is primarily due to increased total precipitation since duration undergoes little change. In spring and fall, decreased duration and increased precipitation combine to increase precipitation rate under climate change. For summer, average precipitation rate is increased because mean storm duration decreases while there is less change in total precipitation.

## 4.5. Discussion

### *4.5.a. Comparison of seasonal vertical structure to MAP case studies*

The greater vertical extent, higher reflectivity values near ground level, and slightly elevated maximum reflectivity in the summer season provide evidence that summer precipitation is more buoyantly-driven than precipitation occurring in winter (Fig. 4.2). The observation of enhanced reflectivity at higher altitudes that coincides with increased probability of JJA-type vertical structure as surface temperature increases is indicative of more unstable stratification of the boundary layer during the summer season. The increased convective nature of summertime precipitation implies stronger vertical air motion (Houze 1993; Houze 1997). Weaker vertical air motion in winter, as evidenced by lower altitude reflectivity, suggests that wintertime precipitation has a more stratiform character. However, convective and stratiform precipitation are not mutually exclusive (Houze 1997). Instead, a single precipitation system may consist of both convective and stratiform areas depending on the range of vertical velocities within the storm. The presence of embedded convective cells can be associated with intense orographic precipitation, such as the historic Alpine flood in central Switzerland during August 2005 (Hohenegger et al. 2008; Langhans et al. 2011).

Several papers describe radar-observed vertical precipitation structure that occurred during the MAP experiment in 1999 (Houze et al. 2001, hereafter H01; Medina and Houze 2003,

hereafter MH03; Yuter and Houze 2003, hereafter YH03; Rotunno and Houze 2007, hereafter RH07). In addition to the Monte Lema radar data used in our study, the MAP analyses utilize data from a temporarily deployed NCAR S-POL dual-polarization Doppler radar and a vertically-pointing radar to derive vertical velocity and distributions of hydrometeor types (H01, MH03, YH03). The vertical structure depicted in the fall season CFAD for years 2004-2010 (Fig. 4.2) has many similarities to the vertical cross sections of radar reflectivity from the fall seasons of 1998 and 1999 observed during MAP (H01). The current study and H01 both observed maximum reflectivity values at 2-3 km asl and increased frequency of radar returns between 2-4 km asl with greater magnitude of reflectivity and frequency towards the north of the Monte Lema radar as compared to the south side. H01 observed that the melting level occurred consistently between 2-3 km asl over the fall seasons of 1998 and 1999. Therefore, as in H01, the maximum reflectivity values observed in our study at 2-3 km asl also indicate the melting level. The larger frequency of reflectivity in the northern sector is likely due to orographic enhancement of precipitation when moisture flux encounters the main crests of the Alps (Fig. 4.1).

Analysis of individual storms that occurred during fall 1998 and 1999 revealed that seasonal average reflectivity was comprised of two types of storms: one type in which stratiform precipitation was enhanced by embedded convection and a second type which only had stratiform precipitation (H01). Individual cases from MAP provide examples of precipitation events with embedded convection (IOP 2b) and events characterized by stratiform structure (IOP 8; MH03; YH03; RH07). The seasonal JJA CFAD for the northern sector presented here (Fig. 4.2) has similarities to the vertical reflectivity cross-section from MAP IOP 2b (MH03). Both show maximum reflectivity (35 dBZ for our JJA CFAD and 35-40 dBZ for IOP 2b) at 3 km asl.

In addition, 15 dBZ reflectivity is observed in the JJA CFAD at 8-10 km asl and at 7 km asl in IOP 2b. The resemblance in vertical structure provides an indication that mesoscale conditions and microphysics described for IOP 2b are typical for summertime precipitation systems. Orographic precipitation is strongly affected by atmospheric stability and moisture flux (H01; MH03; RH07; Panziera and Germann 2010). The precipitation structure during IOP 2b resulted from unstable and unblocked flow with a high Froude number. The precipitation is orographically enhanced by the development of embedded convective cells over the first mountain peaks (MH03; YH03; RH07). The similarity in vertical structure between our JJA-type storm classification and IOP 2b implies that the majority of summer precipitation occurs during unstable/unblocked mesoscale conditions. In IOP 2b fallout of rimed ice particles and graupel from convective cells and coalescence of raindrops beneath the melting level produced locally intense precipitation (MH03; YH03; RH07). The increased intensity associated with JJA-type vertical structure suggests that precipitation is enhanced by microphysical processes similar to those observed during IOP 2b. Also, MH03 note that MAP IOP 2b occurred on a day having average temperature of ~19°C. Figure 4.6 shows the vertical structure of reflectivity associated with the JJA storm type is the most probable vertical structure type at a temperature of 19°C and further supports the relevance of comparison between IOP 2b and JJA-type vertical structure.

In addition, the DJF seasonal CFAD from the north sector resembles the vertical reflectivity profile from MAP IOP 8 (MH03). Both vertical profiles of reflectivity show maximum reflectivity of 30 dBZ at 2 km asl with 15 dBZ reflectivity limited vertically to the 5 km level in the DJF CFAD and 4 km for IOP 8. Furthermore, MAP IOP 8 occurred during a much cooler day with average temperature ~8°C (MH03). At 8°C the most probable vertical structure type is

DJF (Fig. 4.6). The similarity in vertical profiles between our DJF-type vertical structure and IOP 8 could suggest that blocked flow conditions and associated microphysics described for IOP 8 dominate winter season precipitation systems. In contrast to IOP 2b, IOP 8 was found to be more stratiform as its structure is characterized as a layer of dry snow over wet snow with light rain below 2 km (MH03). Some overturning is present due to shear at the top of the blocked airflow, but the resulting vertical motion is not enough to trigger graupel formation or significant riming. Instead, vapor diffusion onto ice is hypothesized as the primary particle growth mechanism (MH03, YH03; RH07). The reduced precipitation intensity associated with DJF-type vertical structure hints that DJF-type storms may be primarily characterized by stratiform microphysical processes as described for IOP 8.

### *4.5.b. Effect of relationship between surface temperature and vertical reflectivity structure on observed seasonal climate*

The relationships between temperature, vertical reflectivity structure and surface characteristics provide insights concerning observed seasonal precipitation. Vertical structure of reflectivity appears to be related to surface temperature (Fig. 4.6), and different precipitation characteristics result from different vertical structures of reflectivity (Table 4.2 and Fig. 4.7). Rudolph et al. (2011) show that precipitation follows an annual pattern in southern Switzerland with daily precipitation at a minimum in winter, increasing in spring, maximized in summer, and decreasing, although highly variable, in fall. We have shown that JJA-type storms increase in probability with increasing surface temperature, and JJA-type storms have the highest precipitation rates, the shortest duration, and the shortest interval between precipitation events. Therefore, the current study indicates that the summertime maximum in precipitation is the result of more frequent and higher intensity precipitation. This aligns with Molnar and Burlando

(2008) who show for southern Switzerland that summer has the shortest and most intermittent storms. Likewise, the annual minimum in daily precipitation experienced during winter stems from less frequent and lower intensity storms. Individual storms having MAM/SON-type vertical structure produce greater total amounts of precipitation than storms with DJF- or JJA-type vertical structure. The large amount of total precipitation produced by MAM/SON-type vertical structure which becomes most common in mid-spring and fall likely contributes to October having the maximum monthly precipitation for the area around the Monte Lema radar (Frei and Schär 1998). Rudolph et al. (2011) observed that 10-day average precipitation amounts in the fall season are occasionally similar to 10-day average precipitation amounts experienced during the summer season. This coincides with our current study's finding that precipitation systems occurring in the warmer days of early fall often have JJA-type vertical structure (Fig. 4.5b). Then, in mid-fall as daily temperatures cool and MAM/SON-type storms become more likely, individual precipitation systems become less intense, but the average precipitation received from each storm increases (Table 4.2 and Fig. 4.5).

### *4.5.c. Future climate implications of relationship between surface temperature and vertical reflectivity structure*

The conditional probability of storm type given the surface temperature combined with observed precipitation characteristics associated with each storm type may have implications concerning global warming's effect on precipitation. Figure 4.6 implies that changes in average daily temperature affect the probability of precipitation having JJA- vs. MAM/SOM- vs. DJF-type vertical structure. This may become especially relevant during the spring and fall seasons if climate change impacts average daily temperature by earlier onset of warmer temperatures in spring or later occurrence of cooler temperatures in fall. If the conditional probability of storm

type given a certain surface temperature remains constant as spring and fall become warmer, longer portions of each season could experience more intense, summer-type storms. The transition to more frequent summer-type storms is similar to results from Beniston (2009) that indicate an increasing portion of European precipitation observed in the 20th century and modeled for the 21st century occurs during "warm modes" (temperature above 75th quantile). In addition, the warm mode precipitation is more likely to have convective precipitation characteristics of short duration and high intensity (Beniston 2009), similar to the precipitation characteristics that accompany JJA-type vertical structure (Table 2).

Previous studies also provide evidence that winter precipitation may be more sensitive to temperature than summer season precipitation. Over the years 1864-2000 the winter season had both the largest increase in seasonal temperatures (0.9-1.1 °C/100y north of the Alps and ~0.6 °C/100y south of the Alps) and the largest positive trend in precipitation at several locations across Switzerland, although notably the precipitation trend is 16-37%/100 y in northern Switzerland with no precipitation trend identified in southern Switzerland (Begert et al. 2005). Regional climate models (RCMs) for the 21st century also predict an increase in precipitation extremes for Europe during the winter season (Frei et al. 2006). In the context of our study, climate change related to an increase in surface temperature leads to an increase of average total precipitation in winter because warmer daily temperatures increase the probability of MAM/SON-type vertical structure which produce higher total amounts of precipitation than DJF-type storms (Fig. 4.8c).

The Monte Carlo simulation results for future climate show average precipitation rate increases in all seasons while the interval between storms is reduced in all seasons (Figs. 4.8b and 8d). Giorgi et al. (2011) describe hydroclimatic intensity (HY-INT) as a combination of the

frequency of heavy precipitation events and the length of the interval between storms. With this perspective, our simulations of increased surface temperature have a mixed effect on HY-INT. On one hand, HY-INT is increased due to higher probability of JJA-type systems that result in higher average precipitation rates. However, the reduction in interval without precipitation following JJA-type storms reduces HY-INT.

The increase in precipitation rate that results from our Monte Carlo simulations is in agreement with many observational and model-based studies. However, the decrease in storm interval is contrary to previous works that find precipitation rate increases under climate change are accompanied by increases in the time interval between storms (Hennessy et al.1997; Dai et al. 1998; Trenberth 1999; Giorgi et al. 2011). Likely, this contradiction arises from our model's inherent assumption of constant precipitation characteristics for each class of vertical structure. However, climate change may affect the availability of atmospheric moisture from evaporation and advection due to changes in soil moisture and large scale circulation. Subsequently, changes in moisture availability may change the distribution of precipitation characteristics for each type of storm (Trenberth et al. 2003). For example, Berg et al. (2009) find observed and modeled precipitation intensity is more dependent on temperature in winter than in summer with the wintertime increase in intensity attributed to increased atmospheric moisture content at higher temperatures due to the Clausius–Clapeyron relationship. However, temperature effects on precipitation intensity are limited in summer by moisture availability, potentially due to drier soil (Berg et al. 2009).

Lastly, phenological evidence based on plant development and freeze dates indicates that spring is occurring earlier in the Northern Hemisphere (Schwartz et al. 2006). Is there any evidence from the Monte Lema radar that convective storms are occurring earlier in spring or

later in fall? To answer this, we examine the day of year for the first occurrence of a JJA-type storm in spring and the last occurrence in fall (Figs. 4.5a and 4.5b). Over the years 2004 -2010, no trend was found concerning earlier onset of JJA-type storms in spring or later occurrence in fall. However, seven years is rather short for a conclusion concerning a climate change signal, especially regarding precipitation, so lack of an identified trend it is not particularly surprising. However, over a longer period of time the date of onset of convective storms in spring and decline in fall may be a worthwhile climate signal to monitor.

### 4.6. Conclusions

Analysis of operational radar data over March 2004 - February 2011 from the Monte Lema radar located close to Locarno, Switzerland indicates that the vertical structure of reflectivity follows a seasonal pattern. Frequency distributions of reflectivity versus altitude (CFADs) reveal that summer precipitation events have the highest vertical extent and greatest reflectivity near the surface as compared to any other season and indicate the increased convective nature of summer-time precipitation. Winter CFADs portray a more stratiform character as reflectivity remains closer to ground level and at lower magnitude than the other seasons. CFADs for spring and fall show a vertical extent and magnitude of reflectivity in between the values observed for summer and winter. The consistency in seasonal CFADs allows classification of individual storms by similarity to vertical structure of reflectivity typically observed in summer, winter, or spring/fall.

Rain gauge data for individual precipitation events reveal unique precipitation characteristics for JJA-, MAM/SON-, and DJF-type storms. JJA-type precipitation events are more severe than DJF-type: shorter duration, higher maximum precipitation rate; but result in similar total precipitation per event. Therefore, a change in the probability distribution of storm-type classification, such as for a specific day or over an entire season, has implications for

precipitation characteristics at the surface. An increase in the probability of JJA-type precipitation events results in a shift towards shorter, more severe storms.

The differences in precipitation characteristics based on different vertical structure of reflectivity have relevance for predicting future precipitation for a changing climate because of the relationship between storm-type classification and surface temperature. A simulation comparing precipitation characteristics between current climate and future climate (perturbed with a temperature increase) shows decreased frequency of DJF-type storms results in an increase in total precipitation for the winter season. In addition, the duration of precipitation events and the interval between events decrease in all seasons while average precipitation rate increases.

These effects demonstrate the role that an increase in the occurrence of convective precipitation may have on hydrologic intensity as climate changes. In addition, the possibility that convective precipitation will play an increasing role in annual precipitation highlights the importance of accurately portraying convection in climate models, either through improved parameterization or spatial resolution appropriate for convective precipitation. Lastly, we point out that our simplified model of vertical reflectivity structure as a function of surface temperature assumes that seasonal relationships between temperature and Froude number remain constant. This raises questions about the localized impacts of climate change on atmospheric stability, moisture flux, and wind speed and direction as these parameters are especially relevant to blocked or unblocked flow in areas of complex terrain where orography influences precipitation distribution.

# CHAPTER 5
# OVERALL CONCLUSION

## 5.1 Main Findings

The research described in this dissertation has resulted in the first published studies of 1) a radar-based precipitation climatology over complex terrain (chapter 2, Rudolph et al. 2011), 2) a quantitative precipitation forecast for specific river basins based on combining high resolution radar-based precipitation estimates with large scale circulation patterns from a GCM (chapter 3, Rudolph et al. 2012), and 3) a multi-year analysis of vertical reflectivity structure in mountainous terrain (chapter 4, Rudolph and Friedrich 2012).

The main findings from this research are:

1. Radar-estimated precipitation data show that precipitation is maximized across the Alps during the summer season, both in terms of average daily precipitation and occurrence of intense precipitation rate. Nine years (2000-2008) of observational radar data were used to analyze total precipitation and the frequency of heavy precipitation events (precipitation rate $\geq$ 20 mm/h) in six regions representing different topographical aspects in the Alps. Total daily precipitation was found to follow an annual cycle across all regions with minimum values in the winter, steadily increasing during the spring, consistently at the highest values in the summer, and then decreasing in late summer and more variable throughout the fall. All regions experienced the most high precipitation rate events during summer and the least number during winter over the years 2000-2008.
2. Precipitation distribution in the Alps is related to synoptic scale weather patterns. The highest amounts of total daily precipitation occur on days with advective weather patterns, a synoptic situation that carries moist air from the Mediterranean toward the Alps. A convective synoptic weather classification having minimal surface pressure

gradient is associated with the occurrence of high precipitation rate. Under synoptic conditions favorable to convection, large total amounts of precipitation are more likely to result from high precipitation rates. Conversely, under an advective synoptic pattern large amounts of total daily precipitation are more likely to result from longer duration, lower intensity precipitation rates.

3. Changes in the frequency distribution of synoptic scale weather patterns are expected to decrease total decadal precipitation by ~10-15% for Swiss river basins by the end of the 21$^{st}$ century. The relationship between synoptic weather patterns and precipitation distribution enables the coupling of radar-estimated precipitation observations and GCM output in order to generate a 21$^{st}$ century precipitation outlook for Swiss river basins. The high spatial resolution (2x2 km$^2$) of the radar-estimated precipitation observations are leveraged to generate the probability and amount of precipitation received within the specific boundaries of each river basin for each synoptic weather pattern. GCM data from CCSM3 for scenario A1B indicate an increased probability of convective high, or anticyclonic patterns, positioned over Switzerland. Since the anticyclonic pattern is observed to produce less precipitation than other synoptic patterns, an increase in its frequency results in a trend of reduced precipitation for Swiss river basins. The probability of heavy precipitation, or total daily precipitation that exceeds the 95th quantile established for 2000-2008, does not appear to be affected by dynamic changes over the 21st century. Therefore, total precipitation is expected to decrease, but heavy precipitation events account for a larger proportion of the total.
4. The vertical structure of radar reflectivity over southern Switzerland follows an annual pattern. The vertical extent of reflectivity, or maximum altitude at which reflectivity is

observed, is maximized during summer and minimized during winter. In addition, the summer season experiences the highest values of reflectivity near the surface and the winter season has the lowest values of reflectivity near the surface. Vertical extent and magnitude of reflectivity for the spring and fall seasons are at intermediate values as compared to summer and winter. The increased vertical extent and magnitude of reflectivity observed during the summer imply that summer season storms are, on average, more likely to contain convective cells while winter season storms have a more stratiform structure.

5. In addition, the vertical structure of radar reflectivity over southern Switzerland is related to surface precipitation characteristics. After classifying individual storms based on the similarity of their vertical reflectivity structure to seasonal averages, it was found that storms having summer-type vertical structure have the highest precipitation rates and the shortest duration. Winter-type storms have the longest duration, lowest total amount of precipitation, and lowest precipitation rates.
6. The vertical structure of radar reflectivity over southern Switzerland is also related to surface temperature. The relationship between vertical reflectivity structure and surface temperature is most evident during the spring and fall seasons. For example, in late spring and early fall when surface temperatures are warm, summer-type vertical reflectivity structure is the most common. However, during early spring and late fall, the cooler portions of each season, winter-type structure is the most common. The relationships between vertical structure, surface precipitation characteristics, and surface temperature suggest that increased temperature due to climate change will increase the probability of more intense summer-type storms, especially in the spring and fall.

## 5.2 Outlook

The work described herein presents several opportunities for further research. One avenue of future work involves taking additional advantage of the high spatial resolution offered by the radar-based precipitation distribution which has an underlying resolution of 2x2 $km^2$. For example, radar-based precipitation observations may be useful for comparison to precipitation data generated from regional climate models. Radar-based precipitation estimates are also relevant for long-term analysis of precipitation over specific terrain features, such as individual catchments or glaciers.

The 21$^{st}$ century precipitation forecast for Swiss river basins also provides opportunities for further work. The study presented here utilizes CCSM3 data from IPCC scenario A1B. The methods developed for this study could be used to compare synoptic weather pattern frequency in multiple GCMs and RCMs for a variety of climate change scenarios. In addition, thermodynamic effects on precipitation have not been addressed. As suggested in chapter 3, a possible approach to quantifying thermodynamic effects is to investigate the dependence of the observed precipitation distribution on specific humidity, atmospheric moisture flux, and soil moisture. These parameters, derived from satellite observations or models, could then be used as an additional conditional variable for a long-term precipitation forecast in order to assess thermodynamic effects.

Additional research questions are also raised by the relationship between vertical structure of reflectivity and surface temperature. The model of vertical reflectivity structure as a function of surface temperature (chapter 4) inherently assumes that the relationship between temperature and vertical structure remains constant. This invites further investigation into the localized impacts of climate change on atmospheric stability, moisture flux, and wind speed and direction as these

parameters are especially relevant to blocked or unblocked flow in areas of complex terrain where orography influences precipitation distribution. Vertical reflectivity data also lends itself to identification of the melting level and could be used for the development of a melting level climatology.

Lastly, this work has been based on the high spatial and temporal resolution of precipitation observations offered by operational radar data. This is especially relevant in areas where complex topography affects precipitation distribution. My research has utilized data from the Swiss radar network – a truly unique dataset that encompasses multiple years of high quality radar data over the complex terrain of the European Alps. Although this work has focused on the Swiss Alps, the methods presented in this dissertation are potentially applicable to any region with the important caveat that radar data are available. Currently, the availability of long-term high quality radar data from mountainous regions outside of the Alps is limited. However, it is my hope that the results from this work have demonstrated the value of radar for monitoring precipitation in complex terrain and will motivate the expanded usage of radar for long term precipitation observations that are relevant to climate.

# REFERENCES

Ahijevych, D. A., C. A. Davis, R. E. Carbone, and J. D. Tuttle, 2004: Initiation of precipitation episodes relative to elevated terrain. *J. Atmos. Sci.*, **61**, 2763–2769.

Allamano, P., P. Claps, and F. Laio, 2009: Global warming increases flood risk in mountainous areas. *Geophys. Res. Lett.*, **36**, L24404.

Bates, B. C., Z. W. Kundzewicz, S. Wu, and J. P. Palutikof, Eds., 2008: *Climate Change and Water*. Tech. Paper VI, IPCC Secretariat, 200 pp. [Available online at http://www.ipcc.ch/pdf/technical-papers/climate-change-water-en.pdf.]

Begert, M., T. Schlegel, and W. Kirchhofer, 2005: Homogeneous temperature and precipitation series of Switzerland from 1864 to 2000. *Int. J. Climatol.*, **25,** 65–80.

Beniston, M., 2005: The risks associated with climatic change in mountain regions. In Uli M. Huber, Harald K. M. Bugmann, and Mel A. Reasoner (Eds.), *Global Change and Mountain Regions:* Springer, pp. 511-520.

Beniston, M., 2009: Trends in joint quantiles of temperature and precipitation in Europe since 1901 and projected for 2100. *Geophys. Res. Lett.*, **36**, L07707.

Berg, P., J. O. Haerter, P. Thejll, C. Piani, S. Hagemann, and J. H. Christensen, 2009: Seasonal characteristics of the relationship between daily precipitation intensity and surface temperature. *J. Geophys. Res.*, **114**, D18102.

Bougeault, P., and Coauthors, 2001: The MAP Special Observing Period. *Bull. Amer. Meteor. Soc.*, **82**, 433–462.

Brodzik, M. J. and K. W. Knowles, 2002: EASE-grid: a versatile set of equal-area projections and grids. In M. Goodchild (Ed.), *Discrete Global Grids*. Santa Barbara: National Center for Geographic Information & Analysis.

Carbone, R. E., J. D. Tuttle, D. A. Ahijevych, and S. B. Trier, 2002: Inferences of predictability associated with warm-season precipitation episodes. *J. Atmos. Sci.*, **59**, 2033–2056.

Christensen, J. H., and O. B. Christensen, 2007: A summary of the PRUDENCE model projections of changes in European climate by the end of this century. *Clim. Change*, **81**, 7–30.

Collins, W.D., and Coauthors, 2006: The Community Climate System Model version 3 (CCSM3). *J. Climate*, **19,** 2122–2143.

Dai, A., K. E. Trenberth, and T. R. Karl, 1998: Global variations in droughts and wet spells: 1900–1995. *Geophys. Res. Lett.*, **25**, 3367–3370.

Doswell, C.A., C. Ramis, R. Romero, and S. Alonso, 1998: A diagnostic study of three heavy precipitation episodes in the Western Mediterranean region. *Wea. Forecasting*, **13**, 102–124.

Fraedrich, K., and C. Larnder, 1993: Scaling regimes of composite rainfall time series. *Tellus, Ser. A*, **45**, 289– 298.

Frei, C. and C. Schär, 1998: A precipitation climatology of the Alps from high-resolution rain-gauge observations. *Int. J. Climatol.*, **18**, 873-900.

Frei, C., R. Schöll, S. Fukutome, J. Schmidli, and P. L. Vidale, 2006: Future change of precipitation extremes in Europe: Intercomparison of scenarios from regional climate models. *J. Geophys. Res.*, **111**, D06105.

Gabella M., U. Germann, M. Boscacci, M. Sartori, and O. Progin, 2009: Planning acceptance tests of the next generation Swiss weather radar network. *34th Conf. on Radar Meteorology*, Amer. Meteor. Soc., P11.3, (accessed from http://ams.confex.com/ams/34Radar/techprogram/paper_154452.htm).

Germann, U., M. Berenguer, D. Sempere-Torres, and M. Zappa, 2009: REAL—Ensemble radar precipitation estimation for hydrology in a mountainous region. *Quart. J. Roy. Meteor. Soc.*, **135**, 445–456.

Germann, U., G. Galli, M. Boscacci, and M. Bolliger, 2006: Radar precipitation measurement in a mountainous region. *Quart. J. Roy. Meteor. Soc*., **132**, 1669-1692.

Germann, U., and J. Joss, 2004: Operational measurement of precipitation in mountainous terrain. In P. Meischner (Ed.), *Weather Radar: Principles and Advanced Applications: (*pp. 52–77). In series *Physics of Earth and Space Environment*, Springer-Verlag, Berlin, Germany.

Gilleland, E. and Katz R.W., 2011: New software to analyze how extremes change over time. *Eos*, **92**, 13-14.

Giorgi, F., E. S. Im, E. Coppola, N. S. Diffenbaugh, X. J. Gao, L. Mariotti, and Y. Shi, 2011: Higher hydroclimatic intensity with global warming. *J. Climate*, **24**, 5309–5324.

Grazzini F., 2007: Predictability of large-scale flow conducive to extreme precipitation over the Western Alps. *Meteor. Atmos. Phys.* **95**, 123-138.

Groisman, P.Y., and R.W. Knight, 2008: Prolonged dry episodes over the conterminous United States: New tendencies emerging during the last 40 years. *J. Climate*, **21**, 1850–1862.

Groisman, P.Y., R.W. Knight, D.R. Easterling, T.R. Karl, G.C. Hegerl, and V.N. Razuvaev, 2005: Trends in intense precipitation in the climate record. *J. Climate*, **18,** 1326–1350.

Hawkins, E., R. Sutton, 2011: The potential to narrow uncertainty in projections of regional precipitation change. *Clim. Dyn.*, **37**, 407-418.

Hennessy, K. J., J. M. Gregory, and J. F. B. Mitchell, 1997: Changes in daily precipitation under enhanced greenhouse conditions. *Climate Dyn.,* **13**, 667–680.

Hirsch, R. M., 2011: A Perspective on Nonstationarity and Water Management. *J. Am. Water Resour. Assoc.*, **47**, 436–446.

Hohenegger, C., A. Walser, W. Langhans, and C. Schär, 2008: Cloud resolving ensemble simulations of the August 2005 Alpine flood. *Quart. J. Roy. Meteor. Soc*., **134**, 889-904.

Houze, R.A., Jr., 1993: *Cloud Dynamics*. Academic Press, 573 pp.

Houze, R. A., Jr., 1997: Stratiform precipitation in regions of convection: A meteorological paradox? *Bull. Amer. Meteor. Soc.*, **78,** 2179–2196.

Houze Jr., R. A., C. N. James, and S. Medina, 2001: Radar observations of precipitation and airflow on the Mediterranean side of the Alps: Autumn 1998 and 1999. *Quart. J. Roy. Meteor. Soc.*, **127,** 2537–2558.

Joss, J. S., and Coauthors, 1998: *Operational Use of Radar for Precipitation Measurements in Switzerland.* Zurich: Hochschulverlag AG, 108pp.

Klein Tank, A.M.G., and G.P. Können, 2003: Trends in indices of daily temperature and precipitation extremes in Europe, 1946–99. *J. Climate*, **16**, 3665–3680.

Kohonen, T., 1997: *Self-Organizing Maps.* 2nd ed., Springer, New York, 426 pp.

Kundzewicz, Z. W., and Coauthors, 2007: Freshwater resources and their management. *Climate Change 2007: Impacts, Adaptation and Vulnerability*, M. L. Parry et al., Eds., Cambridge University Press, 173–210. [Available online at http://www.ipcc.ch/pdf/assessment-report/ar4/wg2/ar4-wg2-chapter3.pdf.]

Laing A.G., and J.M. Fritsch, 1997: The global population of mesoscale convective complexes. *Quart. J. Roy. Meteor. Soc*., **123**, 389-405.

Langhans, W., A. Gohm, and G. Zängl, 2011: The orographic impact on patterns of embedded convection during the August 2005 Alpine flood. *Q. J. R. Meteorol. Soc.* **137**: 2092–2105.

Lin, Y.L., S. Chiao, T.A. Wang, M.L. Kaplan, and R.P. Weglarz, 2001: Some common ingredients for heavy orographic rainfall. *Wea. Forecasting*, **16**, 633–660.

Machguth, H., F. Paul, S. Kotlarski, and M. Hoelzle, 2009: Calculating distributed glacier mass balance for the Swiss Alps from regional climate model output: A methodical description and interpretation of the results. *J. Geophys. Res.*, **114**, D19106.

Martius, O., E. Zenklusen, C. Schwierz, and H. Davies, 2006: Episodes of Alpine heavy precipitation with an overlying elongated stratospheric intrusion: a climatology. *Int. J. Climatol.*, **26**: 1149-1164.

Massacand, A.C., H. Wernli, and H.C. Davies, 1998: Heavy precipitation on the Alpine southside: An upper-level precursor. *Geophys. Res. Lett.*, **25**, 1435-1438.

Medina, S., and R. A. Houze Jr., 2003: Air motions and precipitation growth in Alpine storms. *Quart. J. Roy. Meteor. Soc.*, **129,** 345–371.

Milly, C., and Coauthors, 2008: Stationary is dead: Whither water management. *Science*, **318**, 573–574.

Moberg, A., and Coauthors, 2006: Indices for daily temperature and precipitation extremes in Europe analyzed for the period 1901–2000. *J. Geophys. Res.*, **111**, D22106.

Molnar, P., and P. Burlando, 2008: Variability in the scale properties of high-resolution precipitation data in the Alpine climate of Switzerland. *Water Resour. Res.*, **44**, W10404.

Muller, C. J., P. A. O'Gorman, and L. E. Back, 2011: Intensification of precipitation extremes with warming in a cloud-resolving model. *J. Climate*, **24**, 2784-2800.

O'Gorman, P. A., and C. J. Muller, 2010: How closely do changes in surface and column water vapor follow Clausius-Clapeyron scaling in climate change simulations? *Environ. Res. Lett.*, **5**, 025207.

Overeem, A., I. Holleman, and A. Buishand, 2009a: Derivation of a 10-year radar-based climatology of rainfall. *J. Appl. Meteor. Climatol.*, **48**, 1448–1463.

Overeem, A., T.A. Buishand, and I. Holleman, 2009b: Extreme rainfall analysis and estimation of depth-duration-frequency curves using weather radar. *Water Resour. Res.*, **45**, W10424.

Panziera, L., and U. Germann, 2010: The relation between airflow and orographic precipitation on the southern side of the Alps as revealed by weather radar. *Quart. J. Roy. Meteor. Soc.*, **136**, 222–238.

Plaut, G., and E. Simonnet, 2001: Large-scale circulation classification, weather regimes, and local climate over France, the Alps and western Europe. *Clim. Res.*, **17**, 303–324.

Ranzi, R., Zappa, M. and Bacchi, B.,2007: Hydrological aspects of the Mesoscale Alpine Programme: findings from field experiments and simulations. *Quart. J. Roy. Meteor. Soc.*, **133**, 867–880.

Rotunno, R., and R. A. Houze, 2007: Lessons on orographic precipitation from Mesoscale Alpine Programme. *Quart. J. Roy. Meteor. Soc.*, **133,** 811–830.

Rudari, R., D. Entekhabi, and G. Roth, 2004: Terrain and multiple-scale interactions as factor in generating extreme precipitation events. *J. Hydrometeor.*, **5**, 390– 404.

Rudolph, J.V. and K. Friedrich, 2012: Seasonality of vertical structure in radar-observed precipitation over southern Switzerland. *J. Hydrometeor*., in review.

Rudolph, J.V., K. Friedrich, and U. Germann, 2011: Relationship between radar-estimated precipitation and synoptic weather patterns in the European Alps. *J. Appl. Meteor. Climatol.*, **50**, 944–957.

Rudolph, J.V., K. Friedrich, and U. Germann, 2012: Model-based estimation of dynamic effect on 21st century precipitation for Swiss river basins. *J. Climate*, **25**, 2897-2913.

Schiemann, R., and C. Frei, 2010: How to quantify the resolution of surface climate by circulation types: An example for Alpine precipitation. *Phys. Chem. Earth*, **35**, 403-410.

Schiesser, H., R. Houze, and H. Huntrieser, 1995: The mesoscale structure of severe precipitation systems in Switzerland. *Mon. Wea. Rev.*, **123**, 2070–2097.

Schmidli J, and C. Frei, 2005: Trends of heavy precipitation and wet and dry spells in Switzerland during the 20$^{th}$ century. *Int. J. Climatol.*, **25**, 753-771.

Schmidli, J., C. M. Goodess, C. Frei, M. R. Haylock, Y. Hundecha, J. Ribalaygua, and T. Schmith, 2007: Statistical and dynamical downscaling of precipitation: An evaluation and comparison of scenarios for the European Alps. *J. Geophys. Res.*, **112**, D04105.

Schmidli, J., C. Schmutz, C. Frei, H. Wanner, and C. Schär, 2002: Mesoscale precipitation variability in the region of the European Alps during the 20$^{th}$ century. *Int. J. Climatol.*, **22**, 1049–1074.

Schönwiese, C.-D., J. Rapp, T. Fuchs, and M. Denhard, 1994: Observed climate trends in Europe 1891 – 1990. *Meteor. Z.*, **3**, 22– 28.

Schüepp, M., 1979: *Klimatologie der Schweiz, Band III: Witterungsklimatologie*. Zürich: Schweizerische Meteorologische Anstalt, 93 pp.

Schwartz, M. D., R. Ahas, and A. Aasa, 2006: Onset of spring starting earlier across the Northern Hemisphere. *Global Change Biology*, **12**, 343–351.

Seager, R., N. Naik, G.A. Vecchi, 2010: Thermodynamic and Dynamic Mechanisms for Large-Scale Changes in the Hydrological Cycle in Response to Global Warming. *J. Climate*, **23**, 4651–4668.

Smiatek, G., H. Kunstmann, R. Knoche, and A. Marx, 2009: Precipitation and temperature statistics in high-resolution regional climate models: Evaluation for the European Alps. *J. Geophys. Res.*, **114**, D19107.

Smith, R.B., Q.F. Jiang, M.G. Fearon, P. Tabary, M. Dorninger, J.D. Doyle, and R. Benoit, 2003: Orographic precipitation and air mass transformation: an Alpine example. *Quart. J. Roy. Meteor. Soc*., **129**, 433-454.

Sodemann, H., and E. Zubler, 2010: Seasonal and inter-annual variability of the moisture sources for Alpine precipitation during 1995-2002. *Int. J. Climatol.*, **30**, 947-961.

Solomon, S., D. Qin, M. Manning, M. Marquis, K. Averyt, M. M. B. Tignor, H. L. Miller Jr., and Z. Chen, Eds., 2007: *Climate Change 2007: The Physical Science Basis*. Cambridge University Press, 996 pp.

Stefanicki, G., P. Talkner, and R.O. Weber, 1998: Frequency changes of weather types in the Alpine region since 1945. *Theor. Appl. Climatol.*, **60**, 47-61.

Trenberth, K. E., 1999: Conceptual framework for changes of extremes of the hydrological cycle with climate change. *Climatic Change*, **42**, 327–339.

Trenberth, K. E., A. Dai, R. M. Rasmussen, and D. B. Parsons, 2003: The changing character of precipitation. *Bull. Amer. Meteor. Soc*., **84**, 1205–1217.

Wanner, H., E. Salvisberg, R. Rickli, and M. Schüepp, 1998: 50 years of Alpine weather statistics (AWS). *Meteor. Z.*, **7**, 99-111.

Webster, P. J., and Coauthors, 2010: Extended-range probabilistic forecasts of Ganges and Brahmaputra floods in Bangladesh. *Bull. Amer. Meteor. Soc.*, **91**, 1493–1514.

Weisman, M.L., and J.B. Klemp, 1984: The structure and classification of numerically simulated convective storms in directionally varying wind shears. *Mon. Wea. Rev.*, **112**, 2479–2498.

Widmann, M. and C. Schär, 1997: A principle component and long-term trend analysis of daily precipitation in Switzerland. *Int. J. Climatol.*, **17**, 1333–1356.

Willett, K. M., P. D. Jones, N. P. Gillett, and P. W. Thorne, 2008: Recent changes in surface humidity: development of the HadCRUH dataset. *J. Climate*, **21**, 5364–5383.

Wüest, M., C. Frei, A. Altenhoff, M. Hagen, M. Litschi, and C. Schär, 2009: A gridded hourly precipitation dataset for Switzerland using rain-gauge analysis and radar-based disaggregation. *Int. J. Climatol.*, (published online: 1 Oct 2009).

Yee, T. W., 2008: The VGAM Package. *R News*, **8**, 28–39.

Yee, T. W., and T. J. Hastie, 2003: Reduced-rank vector generalized linear models. *Statistical Modelling*, **3**, 15–41.

Yuter, S. E., and R. A. Houze, 1995: Three-dimensional kinematic and microphysical evolution of Florida cumulonimbus, Part II: Frequency distributions of vertical velocity, reflectivity, and differential reflectivity. *Mon. Weather Rev.*, **123**, 1941–1963.

Yuter, S. E., and R. A. Houze Jr., 2003: Microphysical modes of precipitation growth determined by S-band vertically pointing radar in orographic precipitation during MAP. *Quart. J. Roy. Meteor. Soc.*, **129,** 455–476.

Zappa, M., and Coauthors, 2008: MAP D-PHASE: real-time demonstration of hydrological ensemble prediction systems. *Atm. Sci. Lett*., **9**, 80–87.

Zolina, O., C. Simmer, A. Kapala, S. Bachner, S.K. Gulev, H. Maechel, 2008: Seasonality of precipitation extremes over Central Europe during the last 50 years. *J. Geophys Res.*, **113**, D06110.

Zolina, O., C. Simmer, S.K. Gulev, and S. Kollet, 2010: Changing structure of European precipitation: longer wet periods leading to more abundant rainfalls. *Geophys. Res. Lett*., **37**, L06704.

# APPENDIX 1

## Synoptic patterns as precipitation predictor: rain gauge basis

A modified version of the method used to project 21st century precipitation for Swiss river basins based on radar-estimated precipitation data (Fig. 3.1) was also applied to rain gauge data to evaluate the use of synoptic patterns as a precipitation predictor with the assumption that mean precipitation received during each synoptic pattern remains constant. First, precipitation recorded at 63 Swiss rain gauges for the eight main Schüepp synoptic classifications: AN, AE, AS, AW, CH, CF, CL, MIX (as described in Section 3.2.a.) was evaluated for the 10-year period of 1989-1998. $P(Precip|Class_k)$ was determined following Eq. 3.1 where precipitation days are defined as days when the rain gauge recorded at least 1 mm of total precipitation. For this case, $\overline{Precip}_{d,class\ k}$, as appears in Eq. 3.3, is the mean daily precipitation received at each rain gauge during days when precipitation occurred for each synoptic classification. The observed frequency of each synoptic pattern over 1999-2008, $P(Class_k)$, was used in Eq. 3.6 to predict total precipitation for 1999-2008. This allows comparison of observed precipitation received at each rain gauge to precipitation predicted by synoptic pattern frequency and the mean precipitation distribution for each synoptic pattern (Fig. A1). Figure A1 shows observed vs. predicted total precipitation for the 10 year period of 1999-2008. The data are distributed around the $y = x$ line and have a mean value of predicted-observed (pred-obs) equal to -441 mm with a 95% confidence interval of -1655 to 773 mm. Therefore, the hypothesis that predicted precipitation equals observed precipitation (pred-obs = 0) cannot be rejected, so no bias is found between predicted and observed precipitation. However, performing the analysis on the basis of persistence shows similar results. For the persistence prediction, observed total precipitation

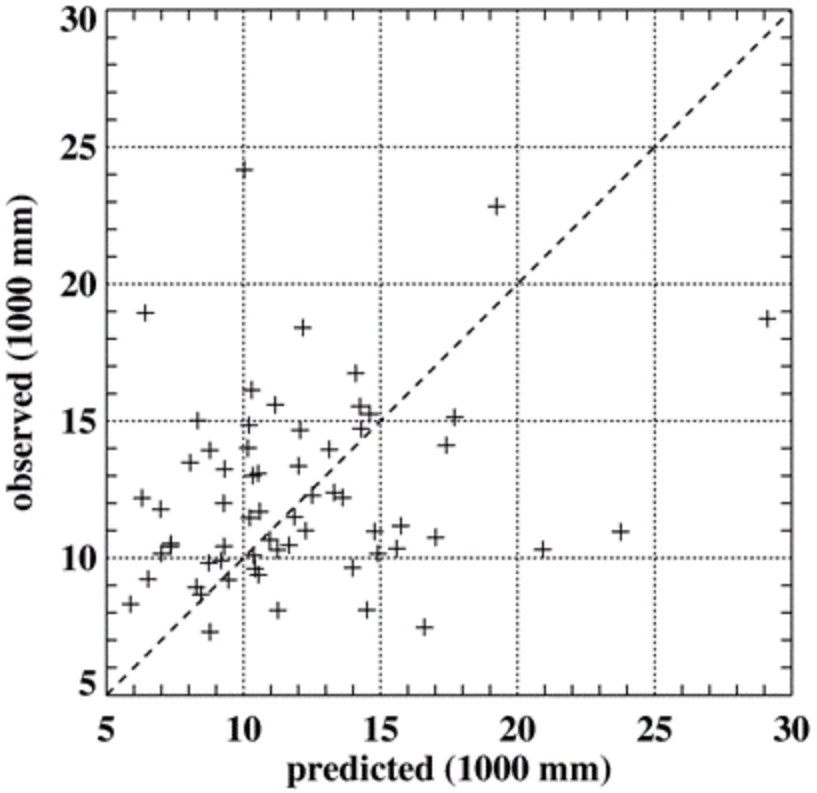


FIG. A1: Observed vs. predicted total precipitation for total precipitation over the 10-year period of 1999-2008 based on rain gauge data from 63 Swiss rain gauges. The dashed line is $y = x$.

over 1989-1998 is used as a predictor for precipitation during 1999-2008. For persistence, the mean value of pred-obs is equal to -588 mm with a 95% confidence interval of -1763 to 587 mm. Therefore, for this case, persistence from the previous decade is also an unbiased precipitation predictor. The similarity in results for the synoptic pattern-based prediction and persistence prediction may be attributed to lack of significant changes in synoptic pattern frequency between the decades used for prediction and observation (Table A1). If the prediction and observation periods contained more substantial differences in synoptic pattern frequencies, it is possible that the outcomes would differ, both for the synoptic pattern-based prediction, as well as the

persistence prediction. However, the main point of performing the rain gauge based analysis is to provide an indication of the extent that mean precipitation associated with synoptic patterns varies over decadal time scales. Although, we can't claim it remains constant in this case, we do not find evidence that it changes enough over the twenty year period of 1989-2008 to induce bias in the synoptic pattern-based decadal precipitation prediction. One notable difference between the rain gauge analysis and the radar-based analysis described in the main text is that rain gauges provide point measurements of precipitation whereas the radar data are spatially integrated over river basins. Since precipitation in complex terrain typically exhibits high spatial variation, it is likely that the spatial integration incorporated in the radar-based approach reduces variability in the difference between observed and predicted precipitation.

| Synoptic Classification | 1989-1998 $P(Class_k)$ | 1999-2008 $P(Class_k)$ | $\Delta$ |
|---|---|---|---|
| AN | 0.13 | 0.15 | 0.01 |
| AE | 0.04 | 0.04 | 0.00 |
| AS | 0.08 | 0.09 | 0.01 |
| AW | 0.08 | 0.08 | 0.00 |
| All Advective | 0.34 | 0.36 | 0.02 |
| CL | 0.07 | 0.06 | -0.01 |
| CF | 0.31 | 0.30 | -0.01 |
| CH | 0.23 | 0.21 | -0.02 |
| All Convective | 0.61 | 0.57 | -0.04 |
| MIX | 0.05 | 0.07 | 0.02 |
| Total | 1.00 | 1.00 | - |

TABLE A1: Frequency of Schüepp's synoptic weather classifications, $P(Class_k)$, for the 10-year periods 1989-1999 and 1999-2008, and the frequency difference between the two periods ($\Delta$).

# APPENDIX 2

## Monte Carlo simulations of current and future precipitation distribution

Monte Carlo simulations of current and future climate were used to quantify the effect of changing surface temperature on precipitation characteristics (Fig. A2). Each simulation has the three-day average temperature as the input variable and outputs daily precipitation characteristics: storm duration, interval between storms, total precipitation amount, and average precipitation rate. For the current climate scenario, we use temperature as observed at Locarno between March 2004 and February 2011 to calculate the mean three-day temperature for each day of the year. For the future climate scenario, the three-day average temperature is increased based on the PRUDENCE (Prediction of Regional scenarios and Uncertainties for Defining EuropeaN Climate change risks and Effects) ensemble modeling results for the seasonal average temperature increase in the Alps over years 2071-2100 as compared to 1961-1990 (Christensen and Christensen 2007). As such, the observed three-day average temperature is increased by 3.53°C for each day in winter, 3.32°C for spring; 5.04°C for summer; and 4.15°C for the days during the fall season. In both the current and future climate simulations, a storm type (DJF-type, MAM/SON-type, or JJA-type) is randomly selected for each day of the year from the probability distribution that results from the vglm of storm types as a function of average three-day temperature (Fig. 4.6 and Eqns. 4.3 and 4.4). The simulation of each day of the year is repeated 100 times. The storm type is then used to select mean precipitation characteristics for each simulated day (Table 4.2). Daily variations in temperature throughout each season and the probability distribution of storm types for each repetition result in the distributions of seasonal precipitation characteristics (Fig. 4.8). In reality, the precipitation characteristics associated with each storm type are continuously distributed (Fig. 4.7) rather than single mean values (Table

4.2). The use of mean values of precipitation characteristics as opposed to a distribution of precipitation characteristics associated with each storm type has the effect of reducing the variances of the resulting seasonal precipitation characteristics (Fig. 4.8).

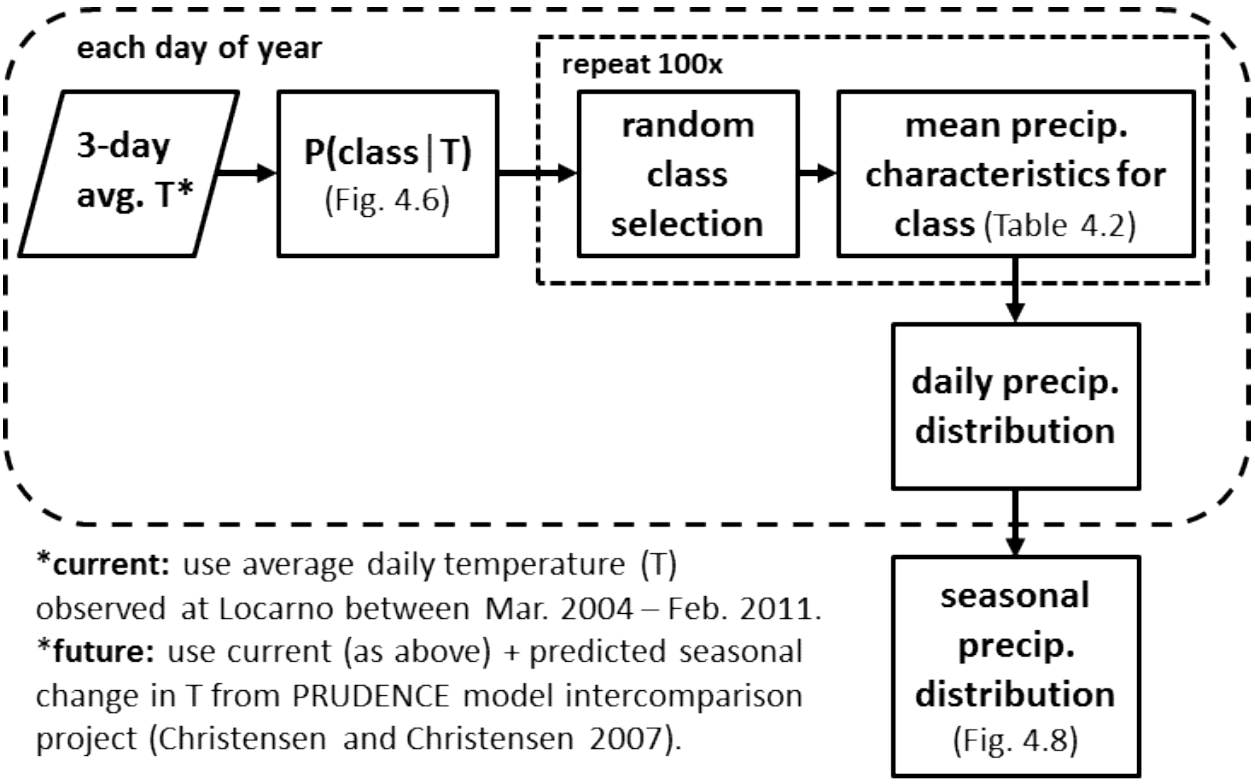


FIG. A2: Process used for Monte Carlo simulations of current and future precipitation characteristics.